




FACULTY OF SCIENCE AND TECHNOLOGY
MASTER THESIS

| | |
|---|---|
| Study programme / specialization: Marine & Offshore Technology/Offshore Wind | The spring semester, 2022 Open |
| Author: Hammad Munir |  (signature of author) |
| Course coordinator: Prof. Yihan Xing Supervisor(s): Prof. Muk Chen Ong Co-Supervisor: Chern Fong Lee | |
| Thesis title: Global analysis of floating offshore wind turbines with shared mooring system. | |
| Credits (ECTS): 30 | |
| Keywords: Offshore wind; single CSC model; dual CSC model; shared mooring line; dynamic response; mooring restoring stiffness. | Pages: 79 + appendix: 2 Stavanger, June 15/2022 date/year |

ABSTRACT

Wind energy harvesting has increased considerably in recent decades across the world. Over the years, wind farms have gradually extended further into the sea to make use of the greater potential of wind resources in deeper water. Floating wind turbines (FWTs) might be a viable option for deep-water applications. The three most researched floating structures so far are spar, semi-submersible, and tension leg platform (TLP). Cost-effective solutions are desired for further viability and commercialization of these concepts. FWTs with a shared mooring system have the potential to be one of the most cost-efficient ways to minimize the cost of mooring. The 5-MW Conceptual Semi-Submersible Concept (CSC) floating structure with a shared mooring line is considered in the present study due to scarce research on this topic.

This study is inspired by the successful research experience of FWTs' feasibility with a shared mooring system presented in Munir et al. (2021) which the first author is the author of this thesis. The present thesis is the continuation work which aims to further investigate the feasibility of FWTs with a shared mooring line. To achieve this, two different methodologies are adopted in Munir et al. (2021) and in the present study. In Munir et al. (2021), two single CSC FWTs are connected with a shared line by removing one anchor fixed mooring line from each. Two different configurations of FWTs are studied with 6 and 8 rotors diameter distance between the FWTs, placed horizontally. Along with the length of the shared line, static equilibrium position of FWTs is also varied. The floaters of a dual CSC model are rotated to accommodate the shared mooring line and wind turbines are rotated to experience the maximum thrust. Global analysis revealed higher maximum surge and sway offsets because of the reduced mooring restoring stiffness as compared to a single CSC model. The reduced restoring stiffness can be attributed to the reduction of one anchor fixed mooring line from each FWTs.

In the present study, three different configurations of the dual CSC model are studied with different shared line and single mooring configurations. This includes Model 1 with a medium-long shared line, Model 2 with a longer shared line, and Model 3 with a relatively shorter shared line. As an alternation of the methodology presented in Munir et al. (2021), the static equilibrium position of FWTs is kept constant at 9 rotors diameter distance and only the length of the shared line varies. The anchor positions are changed to keep the FWTs at their mean static equilibrium position in all the configurations. The orientation of the floaters and wind

turbines is same as in Munir et al. (2021). Dynamic responses of all the configurations are analyzed and compared, including the natural periods, restoring stiffness of the structures, mooring restoring force, and platform motions. The analysis revealed that the surge and sway DOFs are more influenced by the shared mooring configuration with higher offsets and natural periods as compared to a single CSC model. This happens because of the reduced mooring restoring stiffness of the structure in surge and sway directions and no shared mooring restoring force in horizontal DOFs. To avoid the snap loads and increased tension on the fairleads in extreme environmental conditions, Model 1 is recommended for further study in future as compared to Model 2 and Model 3 with a longer and shorter shared line. The results indicate that the dual CSC model with a shared line is a feasible concept and could become an alternative concept in deep water.

KEYWORDS: Offshore wind; single CSC model; dual CSC model; shared mooring line; dynamic response; mooring restoring stiffness.

ACKNOWLEDGEMENTS

First of all, I want to pay high gratitude to my main supervisor, Professor Muk Chen Ong, who ensured that I finish my thesis on time because of his organizational arrangements. His unique understanding continually inspires me to strive toward greater heights of accomplishment. Within a short period of time, I have achieved a personal academic milestone as a result of his support and greetings.

Moreover, I would like to express my sincere appreciation to my co-supervisor, Chern Fong Lee, who has been a mentor and a friend to me during the course of this master's degree and research work. His practical experience in the industry assists me in securing a professional job. His valuable advice and patient guidance contributed a lot to my writing and the completion of my studies. He is always quick to respond to my queries and help me find the answers I am looking for. His approach to academics has been an inspiration to me. His ability to think logically and clearly has been a huge help to me as I conduct my research.

As a member of Professor Ong's research team, I have the distinct privilege of working with so many amazing individuals. Assoc. Prof. Lin Li's practical advice means a lot to me. I would also like to show my special thanks to the fellow classmates: Christodoulos Tryfonidis, and Agata Patrycja Jurga, who are always there for me. Memories of our time together in Norway will live on in my heart.

Finally, I would like to thank my entire family for their support. Their unwavering spiritual support enables me to pursue my ambitions in a faraway land. I intend to share my joy with my family by dedicating this accomplishment to them.

ABBREVIATIONS

| | |
|---------|---|
| FWTs | Floating Wind Turbines |
| TLP | Tension Leg Platform |
| SWL | Sea Water Level |
| MWL | Mean Water Level |
| FOWTs | Floating Offshore Wind Turbines |
| DOFs | Degree of Freedoms |
| WADAM | Wave Analysis by Diffraction and Morison Theory |
| FOWTs | Floating Offshore Wind Turbines |
| FOWF | Floating Offshore Wind Farm |
| BEM | Blade Element Momentum |
| IEC | International Electrotechnical Commission |
| COB | Center of Buoyancy |
| COG | Center of Gravity |
| COM | Center of Mass |
| JONSWAP | Joint North Sea Wave Project |
| Deg | Degrees |
| FEs | Finite Elements |

RESEARCH PAPER

In this thesis, part of introduction, modeling and methodology is included from the paper listed below and is attached in Appendix A.

Paper:

Global analysis of floating offshore wind turbines with shared mooring system.

Hammad Munir, Chern Fong Lee and Muk Chen Ong

Published in *IOP Conference Series: Materials Science and Engineering* (Vol. 1201, No. 1, p. 012024). IOP Publishing.

DECLARATION OF AUTHORSHIP

Regarding the authorship in the above-mentioned paper, I am the first author and responsible for numerical modeling, data analysis, dynamic simulations, and writing the paper under the supervision of Professor Muk Chen Ong and Chern Fong Lee. Chern Fong Lee gave me huge support for the numerical model and provided valuable comments for writing the paper.

TABLE OF CONTENTS

- ABSTRACT i
- ACKNOWLEDGEMENTS iii
- ABBREVIATIONS iv
- RESEARCH PAPER..... v
- TABLE OF CONTENTS vi
- LIST OF TABLES viii
- LIST OF FIGURES ix
- 1 INTRODUCTION..... 1
 - 1.1 Background and motivation..... 1
 - 1.2 Early work on shared mooring 6
 - 1.3 Floating Wind Turbines 7
 - 1.4 Scope and outline of this thesis 11
- 2 THEORY..... 14
 - 2.1 Wind and wave modeling 14
 - 2.1.1 Wind 14
 - 2.1.2 Waves 16
 - 2.2 Aerodynamic load..... 17
 - 2.2.1 Blade Element Momentum (BEM) method 20
 - 2.3 Hydrodynamic loads..... 21
 - 2.3.1 Wave loads on structures & Morison’s equation 24
 - 2.3.2 Response of floating structures 24
 - 2.4 Stability of floating structure 25
 - 2.4.1 Initial Stability 25
 - 2.5 Mooring system 26
- 3 METHODOLOGY 29

| | | |
|---------|---|----|
| 3.1 | Numerical modeling for FWTs..... | 29 |
| 3.1.1 | HydroD model..... | 29 |
| 3.1.1.1 | Hull model of a CSC FWT | 29 |
| 3.1.2 | SIMO Model | 32 |
| 3.1.3 | RIFLEX model..... | 36 |
| 3.2 | Floating wind turbine models | 36 |
| 3.2.1 | Single CSC model | 36 |
| 3.2.1.1 | Single mooring line modeling..... | 40 |
| 3.2.2 | Dual CSC model with varying static equilibrium position | 43 |
| 3.2.3 | Dual CSC model with constant static equilibrium position | 43 |
| 3.2.3.1 | Shared mooring line modeling..... | 44 |
| 3.3 | Coordinate system | 47 |
| 4 | RESULTS AND DISCUSSIONS | 48 |
| 4.1 | Global analysis of FWTs with varying static equilibrium position..... | 48 |
| 4.2 | Free decay test | 49 |
| 4.3 | Constant wind simulations..... | 54 |
| 4.4 | Constant wind with varying wind speeds | 58 |
| 4.4.1 | Environmental conditions | 61 |
| 4.4.2 | Mooring lines tension..... | 62 |
| 4.4.3 | Platform motions | 65 |
| 5 | CONCLUSION | 71 |
| 6 | RECOMMENDATIONS FOR FUTURE WORK..... | 74 |
| 7 | REFERENCES..... | 76 |

APPENDIX A: Research paper

APPENDIX B: Calculation sheet for a single CSC model

LIST OF TABLES

| | |
|--|----|
| Table 1.1 Mooring elements cost. | 5 |
| Table 3.1 Critical parameters of the mass model for a CSC. | 31 |
| Table 3.2 Input properties for CSC body in SIMO. | 33 |
| Table 3.3 Mass moment of inertia with different geometry. | 33 |
| Table 3.4 Quadratic drag force coefficients in SIMO for slender elements. | 34 |
| Table 3.5 Linear stiffness coefficients for the CSC. | 35 |
| Table 3.6 Dimensions of the hull of the 5-MW-CSC by Luan et al. (2016). | 38 |
| Table 3.7 Specifications of the NREL 5-MW wind turbine. Jonkman et al. (2009). | 38 |
| Table 3.8 Design parameters of a single mooring system by Luan et al. (2016). | 41 |
| Table 3.9 Arrangement of fairleads and dual CSC mooring line anchors in global coordinate system. | 42 |
| Table 3.10 Dual CSC FWTs properties. | 44 |
| Table 3.11 Properties of shared mooring line with varying configurations. | 46 |
| Table 4.1 Environmental simulation parameters for the decay tests. | 50 |
| Table 4.2 Natural periods [s] in six degrees of freedom of 5-MW single CSC model from Luan et al. (2016). | 52 |
| Table 4.3 Simulation parameters for incident wind simulation. | 55 |
| Table 4.4 Incident wind speeds simulated. | 58 |
| Table 4.5 Environmental loading for extreme operating condition from Li et al. (2015). | 62 |
| Table 4.6 Statistical properties of a single CSC model presented by Luan et al. (2016). | 66 |

LIST OF FIGURES

| | |
|--|----|
| Figure 1.1 Development of global wind energy between 2001 to 2017 by Council, (2021): (a) Annual installed global capacity; (b) Global cumulative installed capacity. | 1 |
| Figure 1.2 Commonly used FWTs from shallow to deep waters. Robert Speht, (2021). | 2 |
| Figure 1.3 FWTs development. | 3 |
| Figure 1.4 Relation between cost of offshore wind turbine structures and water depth. Musial et al. (2006). | 4 |
| Figure 1.5 Cost breakdown for typical bottom fixed and floating wind projects. Katsouris & Marina, (2016). | 6 |
| Figure 1.6 Offshore wind turbine foundations for shallow and intermediate water. Byrne & Houlsby (2003). | 8 |
| Figure 1.7 FOWTs concept. Illustration by Scheu et al. (2018). | 9 |
| Figure 1.8 CSC semi-submersible FWT. Luan et al. (2016). | 10 |
| Figure 2.1 JONSWAP wave spectrum. | 17 |
| Figure 2.2 Streamlines past rotor with up and downstream of velocity and pressure distribution. Hansen, (2015). | 18 |
| Figure 2.3 Velocities at the rotor plane. Hansen, (2015). | 18 |
| Figure 2.4 Loads at the rotor plane. Hansen, (2015). | 20 |
| Figure 2.5 Boundary conditions of wave-structure interaction problem. Pettersen, (2007). | 22 |
| Figure 2.6 The buoyancy and gravity force in a submerged body. Wen, (2018). | 25 |
| Figure 2.7 An illustration for the inclined barge position. Wen, (2018). | 26 |
| Figure 2.8 Standard layout of the catenary mooring. Gudmestad, (2015). | 27 |
| Figure 2.9 Static equilibrium of mooring line's segment. Kvamen, (2020) | 28 |
| Figure 3.1 Mesh illustration of the hull of the 5-MW-CSC FWT in GeniE. | 30 |
| Figure 3.2 Panel model of a single CSC in HydroD. | 31 |
| Figure 3.3 Surge RAO of the 5-MW-CSC. Munir et al. (2021). | 32 |
| Figure 3.4 Heave RAO of the 5-MW-CSC. Munir et al. (2021). | 32 |
| Figure 3.5 Pitch RAO of the 5-MW-CSC. Munir et al. (2021). | 32 |
| Figure 3.6 Dual CSC FWTs model in SIMA. | 35 |
| Figure 3.7 A 5-MW-CSC single FWT model. Luan et al. (2016) | 37 |
| Figure 3.8 Side view of the hull of 5-MW-CSC. Luan et al. (2016). | 37 |
| Figure 3.9 Top view of the hull of 5-MW-CSC. Luan et al. (2016) | 38 |

| | |
|--|----|
| Figure 3.10 Ballast arrangement. Luan et al. (2016)..... | 39 |
| Figure 3.11 Mooring configuration for single CSC FWT..... | 40 |
| Figure 3.12 Single mooring system diagram for the single CSC and dual CSC FWTs..... | 41 |
| Figure 3.13 Single mooring line shape for three different configurations of dual CSC FWTs..... | 42 |
| Figure 3.14 Illustration of dual CSC FWTs configuration from Munir et al. (2021). | 44 |
| Figure 3.15 Illustration of catenary plane of the shared line. Liang et al. (2021)..... | 45 |
| Figure 3.16 Arrangement of shared mooring line with clump weights in the present study. ... | 46 |
| Figure 3.17 Shared mooring lines shape for three different configurations of dual CSC FWTs. | 47 |
| Figure 4.1 Decay force illustration with ramp duration 50 s, and constant force duration 100 s. Kvamen, (2020) | 49 |
| Figure 4.2 Illustration of eigenmodes in the surge direction (dashed line: initial position, solid line: mode shape)..... | 51 |
| Figure 4.3 Illustration of eigenmodes in the roll direction (dashed line: initial position, solid line: mode shape)..... | 51 |
| Figure 4.4 Free decay test for Model 1: (a) Surge; (b) Sway; (c) Roll; (d) Yaw | 52 |
| Figure 4.5 Free decay natural periods for the dual 5-MW CSC Model 1. | 53 |
| Figure 4.6 Free decay natural periods for the dual 5-MW CSC Model 2. | 53 |
| Figure 4.7 Free decay natural periods for the dual 5-MW CSC Model 3. | 54 |
| Figure 4.8 Stiffness comparison of FWT 1 from constant wind simulation. | 55 |
| Figure 4.9 Stiffness comparison of FWT 2 from constant wind simulation. | 56 |
| Figure 4.10 Illustration of horizontal offset of Model 1 from constant wind simulation..... | 57 |
| Figure 4.11 Illustration of pitch rotation of Model 1 from constant wind simulation. | 58 |
| Figure 4.12 Thrust curve for the 5MW NREL FWTs from constant wind simulation. | 59 |
| Figure 4.13 Platforms surge from incident wind simulation for 0 deg wind direction. | 59 |
| Figure 4.14 Platforms surge from incident wind simulation for 90 deg wind direction. | 60 |
| Figure 4.15 Platforms surge from incident wind simulation for 180 deg wind direction. | 60 |
| Figure 4.16 Relationship between line tension and offset x_g | 63 |
| Figure 4.17 Relationship between line tension and offset y_g | 63 |
| Figure 4.18 System restoring force. | 64 |
| Figure 4.19 Tower-base side-to-side bending moment of FWT 1's tower. | 66 |
| Figure 4.20 Platform surge..... | 67 |
| Figure 4.21 Platform sway | 67 |

| | |
|---|----|
| Figure 4.22 Platform pitch..... | 68 |
| Figure 4.23 Power spectra for platform surge in EC2..... | 70 |
| Figure 4.24 Power spectra for platform sway in EC2. | 70 |
| Figure 4.25 Power spectra for platform pitch in EC2. | 70 |

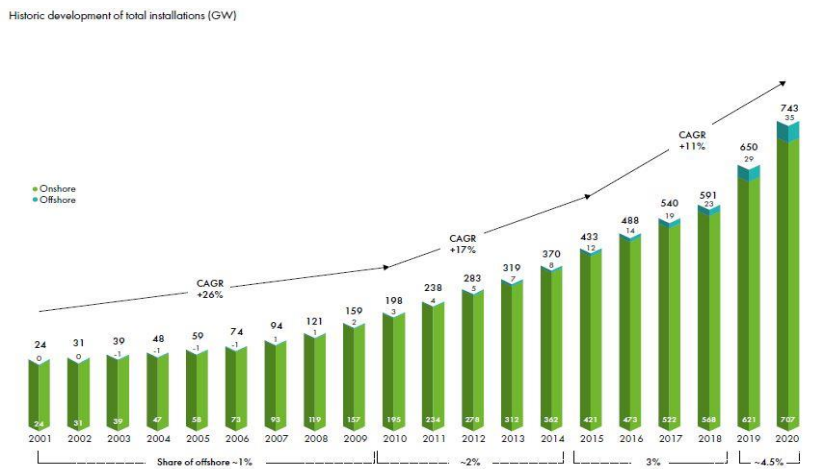
1 INTRODUCTION

1.1 Background and motivation

In past decades, the development and demand of global wind power generation have expanded dramatically. From Figure 1.1 (a), we can see that the annual installed wind capacity in 2020 is above 90 GW, bringing the cumulative wind capacity up to 743 GW proposed by Council, (2021) as shown in Figure 1.1 (b). Wind turbines can be used to capture and convert wind energy into electricity. In terms of the direction of the rotating axis, FWTs are divided into horizontal-axis wind turbines (HAWTs) and vertical-axis wind turbines (VAWTs). Because HAWTs have higher aerodynamic efficiency and tip-speed ratio (TSR) than VAWTs, HAWTs with higher commercial values are increasingly more common in the global wind energy business.



(a)



(b)

Figure 1.1 Development of global wind energy between 2001 to 2017 by Council, (2021): (a) Annual installed global capacity; (b) Global cumulative installed capacity.

Given the scarcity of fossil fuels and our growing understanding of global climate change, it is a common objective of humanity to reduce greenhouse gas emissions into the atmosphere. One of the most critical stages in achieving this aim is to replace fossil fuels with renewable energy sources. Wind energy is expected to play a significant role in the future energy infrastructure. Floating Wind Turbines (FWTs) have been increasingly considered in the wind energy sector during the last decade due to ample wind resources in deeper water. The main reasons for this are the reduced offshore surface friction, better wind production due to reduced average turbulence, and the avoidance of noise and sight pollution owing to the significant distance from inhabited areas. This concept has become even more viable because of improved maritime transport infrastructure such as huge towing vessels and massive lift cranes. Therefore, a lot of research has been conducted e.g., by Musial et al. (2004), Fontana et al. (2016), and Katsouris & Marina, (2016) around the design of FWTs to make them more cost-effective and sustainable. Widely used floating offshore wind turbines and advancements in their design by Robert Speht, (2021) from shallow to deep waters are shown in Figure 1.2.

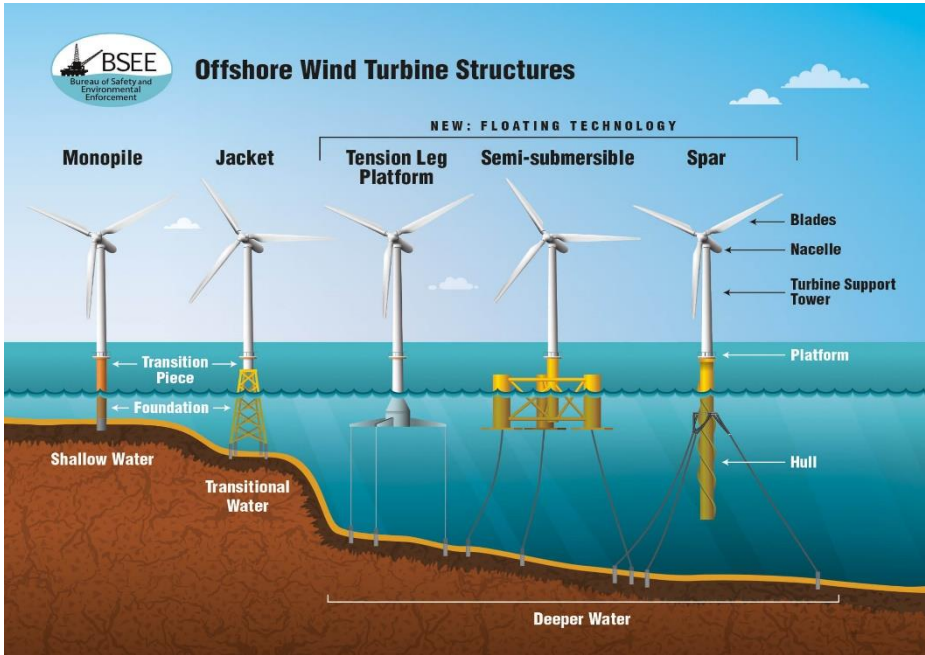


Figure 1.2 Commonly used FWTs from shallow to deep waters. Robert Speht, (2021).

The offshore wind sector will continue to expand nationally. Fixed offshore wind turbines, with water depth ranging from 0 to 50 meters, will continue to dominate the industry. Mainly used substructures for fixed offshore wind turbines from shallow to intermediate water depth are monopile, tripod, and jacket, as shown in Figure 1.2. Among the above-mentioned reasons for

FWTs development in deeper water, one reason is their better standardization due to less site dependency on foundations.

Equinor has been operating the world's first floating wind turbine park, the Hywind park, with five 6 MWs turbines, since 2017. The distance to the shore is between 25 and 30 kilometers, with a water depth of above 100 meters published by Rummelhoff, (2017). Floatgen has been in operation since 2018 and produced 6 GWh of power in 2019, with a 14% increased production in 2020 according to new research Floatgen breaks new records in 2020, (2021). WindFloat was launched in 2011 with a 2 MW Vestas turbine by The WindFloat® advantage, (2020). Hitachi Zosen, with NEDO funding, began construction of two 3-5 MW turbines with concrete and steel Ideol platforms, and were installed in 2018 Richard, (2018).



Hywind park. Rummelhoff, (2017)



Floatgen. Floatgen breaks new records in 2020, (2021)



WindFloat®. WindFloat® advantage, (2020)



Hitachi Zosen. Richard, (2018)

Figure 1.3 FWTs development.

On the other hand, offshore wind turbines provide practical challenges, such as a more significant initial investment, complex structural design, limited accessibility, and higher expenses associated with maintenance and electric power supply to shore. The cost of the floating structure remains one of the largest hurdles in fully deploying commercialized floating

wind farms due to the demand for a more compliant supporting structure to manage the dynamic motions of the wind turbine within reasonable limits. The most important aspect of offshore wind turbine development is the substructure, which must be chosen primarily based on the water depth. As water depth increases, the cost of offshore substructures will rise due to the increased complexity and equipment required below the sea surface. Musial et al. (2006) shows the relation between water depth and the cost of offshore wind turbine substructure in Figure 1.4.

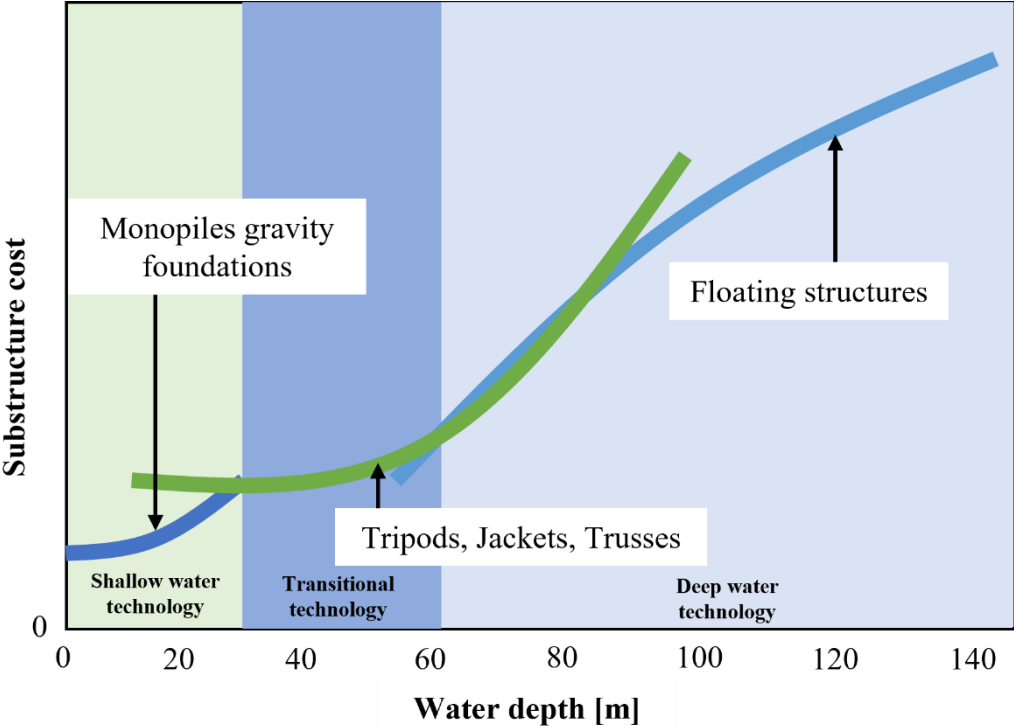


Figure 1.4 Relation between cost of offshore wind turbine structures and water depth. Musial et al. (2006).

Reducing the structural weight by lowering the number of components is one of the most promising strategies to reduce the Levelized cost of energy (LCoE). When it comes to floating offshore wind farms (FOWFs), sharing mooring lines between nearby FWTs is an appealing idea for lowering the LCoE and reducing the number of installation operations. By sharing mooring lines between two nearby FWTs, the overall number of mooring lines is reduced. The number of anchors required also lower, resulting in considerable cost savings for anchor installation as proposed by Liang et. al (2020) for the dual spar case. Ikhennecheu et al. (2021) describes that the cost of a mooring line depends on the material and the type. Furthermore,

following the guidelines of Benveniste et al. (2016), the cost of a single mooring line is determined by its weight and may be calculated as follows:

$$CML = Cm * lML * mML \tag{1}$$

where *CML* is the cost of a mooring line (€), *lML* is the length of a mooring line (m), *mML* is the mass (kg/m), and *Cm* is the mooring line's cost in €/kg.

As with the mooring line, the cost of an anchor varies depending on the type of anchor. Beiter et al. (2016) introduced two generic functions as well as cost values for anchor and mooring expenses based on the technology where:

$$Drag - embedded\ anchor\ cost = 10.198 * MBL \tag{2}$$

$$Chain\ cost = (0.0591 * MBL - 87.69) * L \tag{3}$$

where *MBL* is minimum breaking load and *L* is the length of chain. Costs are calculated using these functions dependent on chain tension (not the holding capacity). Table 1.1 shows some values derived from Bjerkseter & Ågotnes, (2013) and Hurley & Nordstrom, (2014).

Table 1.1 Mooring elements cost.

| Type | Bjerkseter & Ågotnes, (2013) | Hurley & Nordstrom, (2014) | Average cost (£) |
|----------------------------|---------------------------------|-------------------------------|------------------|
| | Drag-embedded | Driven pile | - |
| Anchor cost (£/anchor) | 97,000 | 160,000 | - |
| Mooring cost (£/anchor) | 34,000 | 41,000 | 36,000 |

Note: All costs are converted to pound sterling at the actual year.

A breakdown of the typical capital expenditure (CAPEX) for a bottom-fixed and floating wind farm by Katsouris & Marina, (2016) is shown in Figure 1.5.

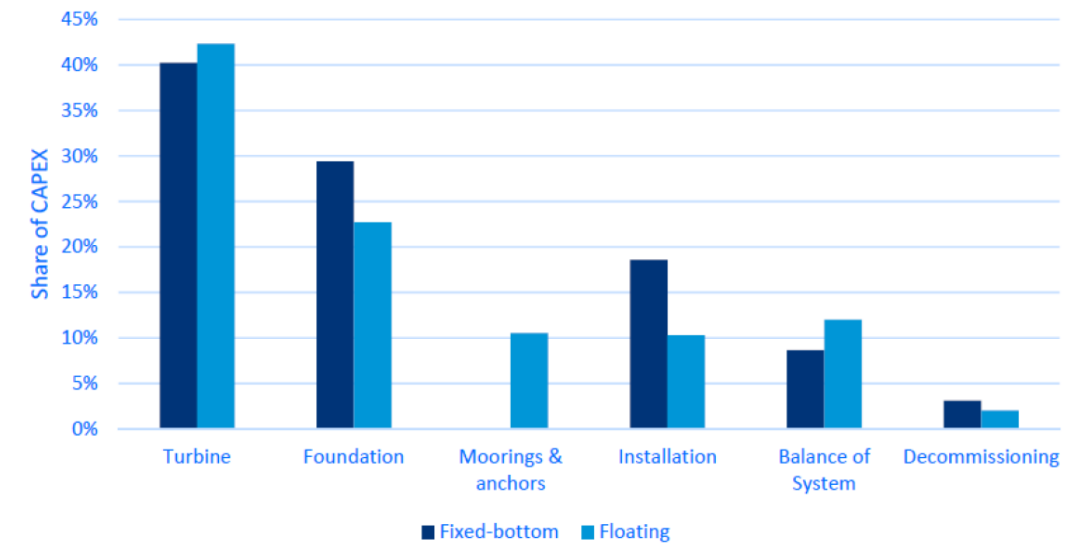


Figure 1.5 Cost breakdown for typical bottom fixed and floating wind projects. Katsouris & Marina, (2016).

Mooring cost for the FWTs will be reduced by connecting the adjacent FWTs with a shared line which is the basis for the present study. This could reduce the amount of mooring lines and anchors needed for the project, thus lowering the overall cost.

1.2 Early work on shared mooring

Musial et al. (2004) gave a thorough description of common support structures of FWT, including anchors, platform geometry, and mooring systems. In the paper, it was claimed that the cost of anchoring single FWT is the biggest disadvantage. Moreover, in an FOWF, specific anchors type, and mooring arrangement could assist in minimizing mooring expenses.

Fontana et al. (2016) suggested and simulated shared anchor systems for FWTs. They showed a variety of geometric arrangements that could be used for layouts of FWTs. These arrangements are built on square and hexagonal unit cells and are used in substantial wind farms with 100 or more turbines. According to time-domain simulations of multidirectional anchors and mooring line forces, the total number of anchors required for a FOWF could be considerably decreased by anchoring numerous FWTs to the same anchor.

Goldschmidt & Muskulus, (2015) used numerical modeling in the time and frequency domains to evaluate FOWFs with shared mooring systems. They modeled only translational motions in linear, triangular, and rectangular array layouts at a depth of 200 meters. The linear array is

simulated in the time domain, while the others in the frequency domain. Their studies demonstrated that using shared moorings can save money, but only up to a certain farm size, after which the additional cost of mooring line become too expensive to make shared moorings viable.

Shared mooring systems are also investigated in the framework of wave energy converters. Using a time-domain simulation, Gao & Moan, (2009) studied a system of nine wave energy converters connected to each other and the seafloor. The lines connecting from converter to converter are frequently subjected to severe stresses, indicating that the possibility of snap loads in FOWF with shared mooring should be considered.

Liang et al. (2021) also studied the effect of a shared mooring system on the natural periods of FWTs with dual spar configuration. Irvine's methodology and response surface method was adopted to design the shared line, and a sensitivity analysis was carried out to assess the contributions of various mooring parameters. It was concluded that the sensitivity study was helpful to design the mooring system away from the excitation loads frequencies and influence of different mooring properties on natural periods of the system.

1.3 Floating Wind Turbines

Wind turbines can be installed both onshore and offshore. Based on the water depth criteria, FWTs are divided into three categories by Roddier & Weinstein, (2010):

- Shallow water, if the water depth is below 30 meters.
- Intermediate water, if the water depth is between 30 to 60 meters.
- Deepwater, if the water depth is above 60 meters.

Byrne & Houlsby, (2003) proposed that most economical bottom fixed foundations wind turbines in shallow to intermediate water depth are gravity-based, monopile, and suction bucket which are schematically presented in Figure 1.6.

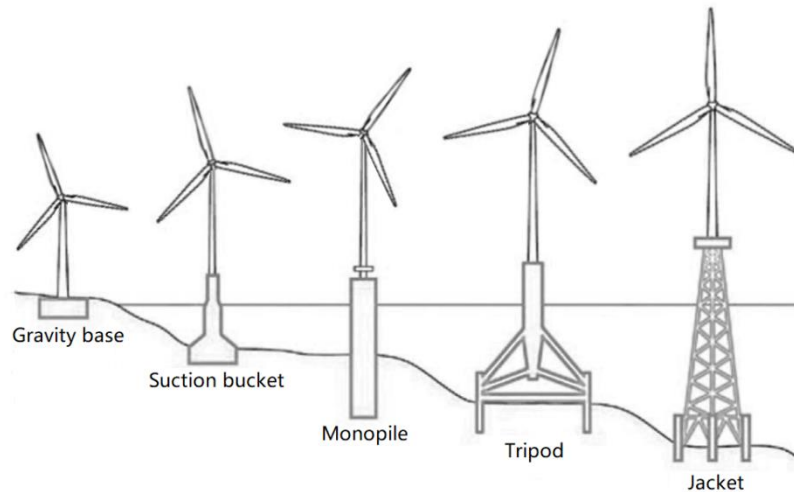


Figure 1.6 Offshore wind turbine foundations for shallow and intermediate water. Byrne & Houlsby (2003).

Monopile are the most deployed foundations in shallow water due to their simplicity, minimum design developments of existing onshore monopiles, and footprints on the seabed as described by Siavashi, (2018). Monopiles, on the other hand, are limited in their use in deeper waters due to their flexibility, that is, the structure's natural frequency to be dropped into a range of the excitation sources' frequencies. Furthermore, accommodating monopiles in deeper water necessitates more bulk and specialized installation equipment, as well as a higher cost.

Moreover, gravity-based foundations are free from flexibility issues of monopiles but require detailed soil analysis and significant seabed preparation. Suction bucket foundations also have some advantages, like avoiding the use of large pile drivers as in monopile foundations. But the cost of gravity base and suction bucket foundations will grow dramatically with water depth. Tripod and submerged jacket foundations as shown in Figure 1.6 are economically feasible solutions for the intermediate water depth. A submerged jacket with a transition tube tower, for example, was chosen as the foundation for the 588 MW Beatrice offshore wind farm, which is located 13.5 km off the coast of Caithness in the United Kingdom. The Beatrice offshore wind farm has been entirely operational since June 2019, but the foundations used in transitional waters need to have a wider base with multiple anchor points by Beatrice Offshore Windfarm Ltd homepage, (2022).

In deep water depth, a floating substructure is the most cost-effective alternative. A floating substructure must have enough buoyancy to sustain the weight of the wind turbine and the ability to bear environmental loads such as wind, waves, and current loads. Deep-sea substructures can be configured in a variety of ways. Illustration of commonly deployed Floating Offshore Wind Turbines (FOWTs) foundations is shown in Figure 1.7.

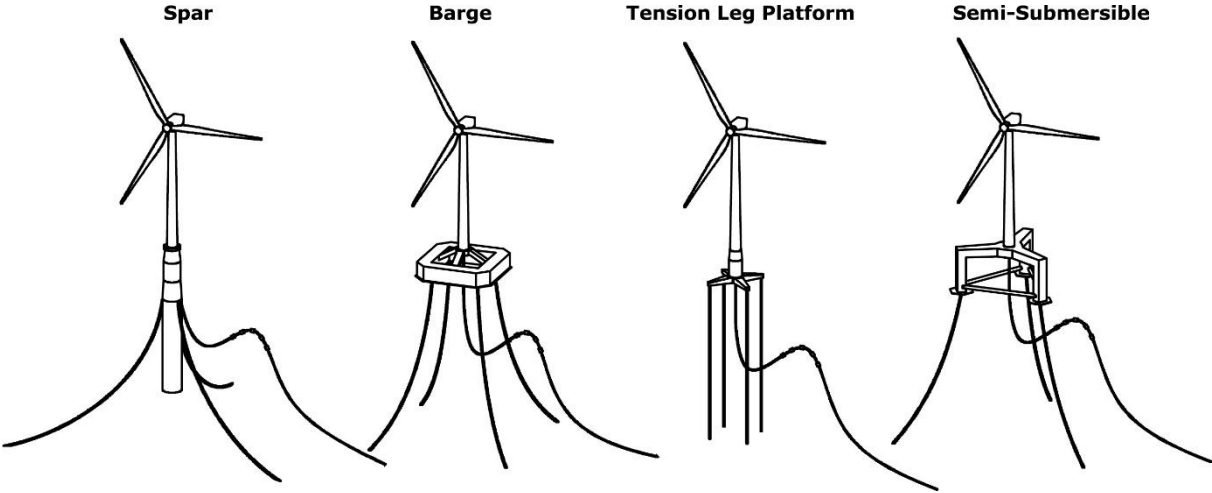


Figure 1.7 FOWTs concept. Illustration by Scheu et al. (2018).

Spar-buoy can be moored either by catenary or taut lines. Stability can be achieved by using ballast to lower the center of mass (COM) below the center of buoyancy (COB). For the TLP, stability achieves by using tension in the mooring lines which is provided by enough buoyancy in the tank. For the barge, stability is usually achieved by its waterplane area and catenary lines are used as a mooring system Siavashi, (2018).

Similarly, the 5-MW-CSC is a new braceless semi-submersible platform proposed by Luan et al. (2016) to support the NREL 5-MW horizontal axes wind turbine. Research on this concept is relatively scarce than the other similar concepts as described above. This concept is used in the present study with a shared mooring configuration. The detailed design and layout of this platform is discussed in Chapter 3. Typical 5-MW-CSC semi-submersible FWT is shown in Figure 1.8.

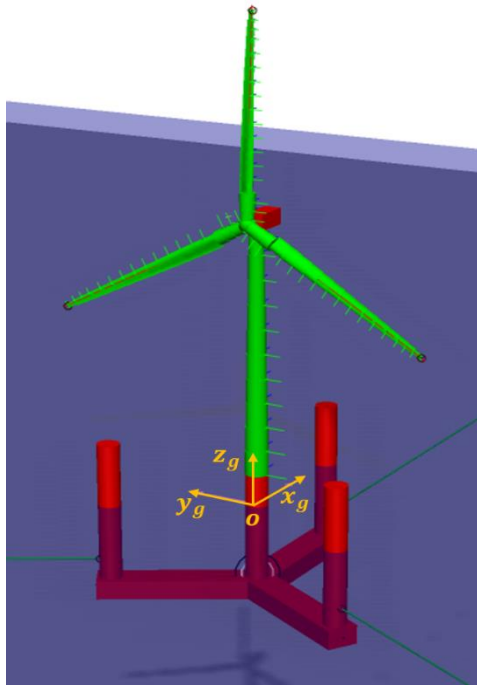


Figure 1.8 CSC semi-submersible FWT. Luan et al. (2016).

1.4 Scope and outline of this thesis

The main scope of this thesis is to investigate the feasibility of two CSC semi-submersible FWTs connected with a shared mooring line utilizing two different methodologies. Several sub-scopes of the study have been defined and achieved, which are listed below.

Scope 1: Dual CSC FWTs with varying static equilibrium position in Munir et al. (2021):

- To establish the numerical models to be tested:
 - Single CSC model, moored with chain-clump configuration at 200m water depth.
 - Dual FWT model with two CSCs placed at 6 rotors diameter distance, connected with a 671 m long shared mooring line in 200m water depth.
 - Dual FWT model with two CSCs placed at 8 rotors diameter distance, connected with a 911 m long shared mooring line in 200m water depth.
- To establish two sets of environmental conditions which are the combination of turbulent wind and irregular waves in operational and survival condition for dynamic analysis.
- To perform one-hour duration of dynamic simulation with 6 random wave seeds for each environmental case.
- To investigate the dynamic responses of each FWT part of the dual CSC models and compare them with a single CSC model.

Scope 2: Dual CSC FWTs with constant static equilibrium position (Present thesis):

- To establish the numerical models to be tested:
 - Single CSC model, moored with chain-clump configuration at 200m water depth.
 - Three dual FWT models with two CSCs placed at 9 rotors diameter distance, connected with a 1055 m, 1085 m, and 1105 m long shared mooring line in 200m water depth.
- To carry out natural period from decay tests and compare the results among different models.

- To establish a test procedure to capture the change in mooring restoring forces with varying wind direction, constant wind speed and no waves.
 - Compare the findings with a single CSC model.
- To establish a test procedure to capture the change in mooring restoring forces with varying wind direction, varying wind speed and no waves.
 - Compare the findings with a single CSC model.
- Analyze the mooring lines' tension in static configuration and estimate the offset limit and restoring force.
 - Compare the findings with a single CSC model.
- To establish three sets of environmental conditions which are the combination of constant wind and irregular waves in operational conditions for dynamic analysis.
- To perform one-hour duration of dynamic simulation with 6 random wave seeds for each environmental case.
- To investigate the dynamic responses of each FWT part of the dual CSC model and compare them with a single CSC model.

Finally, this thesis involves following six chapters.

Chapter 1: The general motivation and background of the study are introduced, and the scope of work and outline are defined. Part of the contents from Munir et al. (2021) is included in this chapter.

Chapter 2: The main theory of this study and related literature reviews are summarized in this chapter.

Chapter 3: This chapter includes the summarized methodology 1 of modeling dual CSC models with a shared line from Munir et al. (2021). Following the motivation from Munir et al. (2021), methodology 2 of modeling two FWTs horizontally connected with a shared mooring line is presented. Single and shared mooring line modeling, GENIE modeling, WADAM analysis, SIMA analysis, and basic parameters calculations are listed.

Chapter 4: The dynamic analysis of both the FWTs is included. A comparative study of mooring lines tension, system's restoring force, restoring stiffness of the structure, system's

responses and natural periods in 6 DOFs for all the three configurations are investigated. The main findings from Munir et al. (2021) are also summarized in this chapter.

Chapter 5: A summary of the thesis is included in this chapter. The main conclusions on the feasibility of the proposed model are addressed.

Chapter 6: The last chapter involves the recommendations for the future work of the thesis.

2 THEORY

The fundamental theories of dynamic analysis of FOWTs are introduced. In the first section, wind and wave numerical models are presented. The floating structure's aerodynamic model and hydrodynamic loads are discussed. The initial stability and mooring of floating structure are presented.

2.1 Wind and wave modeling

The theory of wind field formation and the wave profile is discussed in this section. A model with constant wind and an irregular wave is used in this work to depict the stochastic variations of wind and wave. The energy distribution at various frequencies is calculated using the spectra of wind and wave. The wind and wave spectra are then used as inputs for additional aerodynamic and hydrodynamic load computations. In the first section, the above-mentioned theories are described.

2.1.1 Wind

One of the most popular approaches for describing the profile of wind speed is the power law. Wind speed varies with altitude, and the gradient of the wind speed profile is influenced by the terrain factors and the atmospheric stability. The following equation expresses the mean wind speed $U(z)$ at a given height z described by Jonkman & Kilcher, (2012):

$$U(z) = U(z_{ref}) \left(\frac{z}{z_{ref}} \right)^\gamma \quad (4)$$

where $U(z_{ref})$ is the mean wind speed at reference height z_{ref} and γ depends on the terrain conditions; the reference height z_{ref} above the mean water level is 90 m in this study. γ is defined as 0.14 in the present study due to the offshore condition according to IEC 61400-1, (2005).

The turbulent wind having a violent fluctuation in pressure and wind velocity, may depict the actual condition during operation. This phenomenon could be caused by the loss of wind kinetic energy into the thermal due to passage across the boundary layer by Wen, (2018). The turbulence intensity, defined as the ratio of the standard deviation of the wind speed to the mean speed in a time series of records, is commonly used to assess this effect.

$$I = \frac{\sigma}{\bar{U}} \quad (5)$$

The characteristics of turbulence will vary depending on the wind speed. The standard deviation of the longitudinal wind speed component is expressed in IEC 61400-1, (2005). At $u_{hub}=15$ m/s, the turbulence intensity I_{15} is determined, which may follow the IEC standard with different types of Class.

$$\sigma_u = \frac{u_{hub}}{\ln\left(\frac{z_{hub}}{z_o}\right)} + 1.28 \times 1.44 \times I_{15} \quad (6)$$

The Turbsim application can generate a turbulent wind field by numerically simulating the time series of wind fields using a statistical model as presented by Jonkman & Kilcher, (2012). This study uses the IEC Kaimal turbulence model, defined by a velocity spectrum and shown in the equation below.

$$S_k(f) = \frac{4\sigma_k^2 \cdot L_k / u_{hub}}{(1 + 6f \cdot \frac{L_k}{u_{hub}})^{5/3}} \quad (7)$$

where k denotes u, v, w in longitudinal, lateral, and vertical direction; f is the cyclic frequency; u_{hub} is the mean wind speed at hub height; σ_k is the standard deviation; L_k is an integral scale parameter which is proportional to the turbulence scale parameter, Λ_U . The turbulence scale parameter might be determined using the minima of the hub height z_{hub} and 60 meters.

$$\begin{aligned} \sigma_v &= 0.8\sigma_u \\ \sigma_w &= 0.5\sigma_u \end{aligned} \quad (8)$$

$$L_k = \begin{cases} 8.10\Lambda_U, & k = u \\ 2.70\Lambda_U, & k = v \\ 0.66\Lambda_U, & k = w \end{cases} \quad (9)$$

$$\Lambda_U = 0.7 \times \min(60m, z_{hub}) \quad (10)$$

Furthermore, neutral stability is assumed in this model, implying that the gradient Richardson number is zero. In the Turbsim program, a grid width and height must be defined to cover the entire region of FWTs. The IEC Kaimal model's velocity spectra are anticipated to be invariant throughout the whole grid., but due to spatial coherence, there is a minor amount of variance in

the standard deviation in the longitudinal direction as described by Jonkman & Kilcher, (2012). The constant standard deviations of the v and w components will span the entire grid. Finally, an inverse fast Fourier transform can be used to construct the velocity distribution in the time domain from the velocity spectrum.

2.1.2 Waves

Originally, the free surface of waves is stochastic with random probability. The real sea surface is commonly described by the summation of sinusoidal wave components for a simplified solution. The state of the sea might be long-term or short-term. The short-term sea condition, i.e., one hour duration, will be investigated in the present study. Wave spectrum is frequently used to describe the energy of a sea state in a short-term situation. Several spectra have been established to characterize the sea state for the short-term situation. In the present study, for the time-domain simulations, the JONSWAP spectrum is used.

The JONSWAP spectrum was developed as part of the "Joint North Sea Wave Project," a well-known joint research project. It was based on wave measurements taken from Sylt to 160 kilometers out into the North Sea between 1968 and 1969. The JONSWAP spectrum can be used to define the state of the sea, which can include both underdeveloped and fully developed conditions. The spectrum of JONSWAP defined in SIMO by SINTEF Ocean, (2017) is presented as follows:

$$S_{\xi}(\omega) = \frac{\alpha g^2}{\omega^5} \exp\left(-\beta\left(\frac{\omega_p}{\omega}\right)^4\right) \gamma^{\exp\left(\frac{(\omega/\omega_p-1)^2}{2\alpha^2}\right)} \quad (11)$$

where ω_p is the peak frequency which is equal to $2\pi/T_p$; γ is the peakedness parameter and a typical value of 3.3 refers to a non-fully developed sea state; β with a default value of 1.25 is form parameter; α is the spectral parameter, but to parameterize the spectrum, significant wave height H_s is often used.

$$\alpha = \left(\frac{H_s \omega_p^2}{4g}\right)^2 \frac{1}{0.065\gamma^{0.803} + 0.135} \quad (12)$$

Several critical parameters, including H_s , T_p , and γ , can influence the shape of JONSWAP. The wave energy and potential instability of a floating structure increase as the significant wave height H_s and the peak period T_p are raised. The peakedness of the spectrum is determined by

γ parameter. A three parameter JONSWAP spectrum with $H_s = 6$ m and $T_p = 10$ s is applied to the structure for the initial study of FWTs model as shown in Figure 2.1.

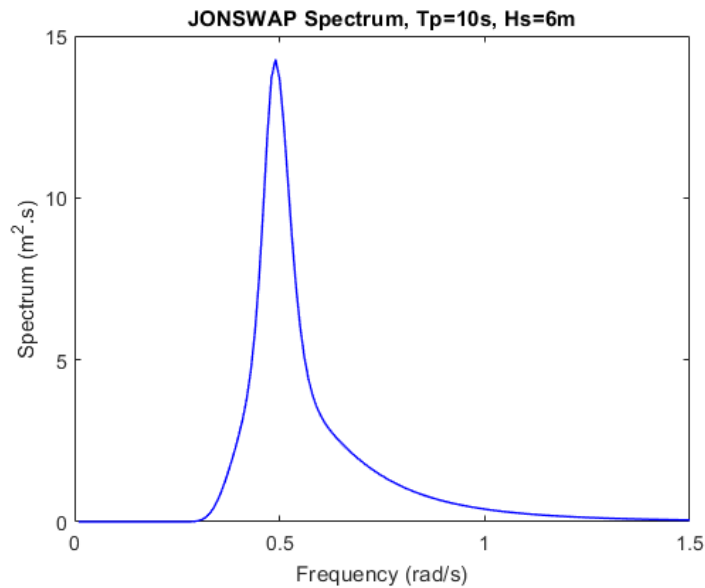


Figure 2.1 JONSWAP wave spectrum.

2.2 Aerodynamic load

The force to which wind turbines are exposed is called a thrust force from the incident wind. The following theory and derivations will follow the explanation in Hansen, (2015).

One-dimensional momentum theory and an ideal rotor were used to calculate this thrust force, with the following assumptions:

- Steady-state, incompressible, homogeneous fluid flow.
- Negligible frictional drag.
- No flow at the stream tube's end.
- Infinite blades with a consistent thrust over the disk.
- Irrotational wake.
- At a distance far from the rotor disk, the pressure is equal to the ambient pressure.

Streamlines of the wind based on these assumptions with corresponding pressure and velocity distribution are shown in Figure 2.2.

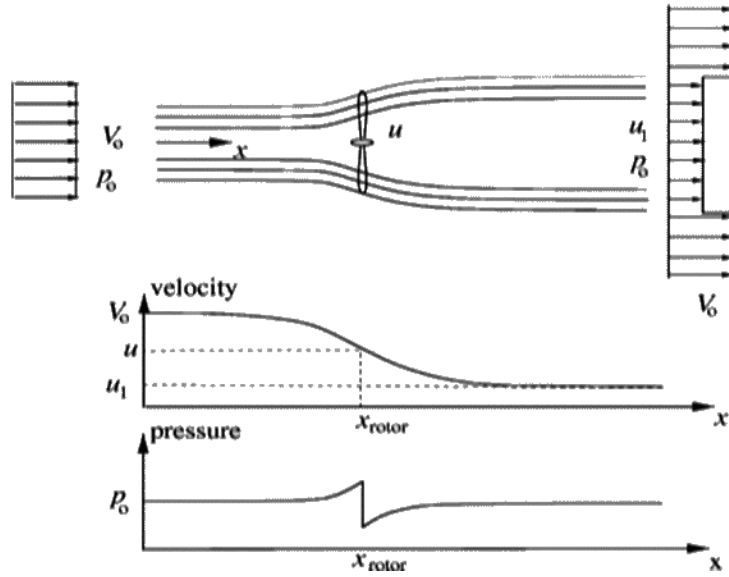


Figure 2.2 Streamlines past rotor with up and downstream of velocity and pressure distribution. Hansen, (2015).

In the above figure, V_0 is the velocity of the incoming wind, u_1 is the wind speed at far side of the rotor, u is the rotor speed, and P_0 is the flow pressure.

The lower pressure on the rotor's far side causes a thrust force, T , on the wind. This force, T , slows down the wind to extract kinetic energy. Equations 13 and 14 represent the thrust force and pressure drop determined using the Bernoulli equation.

$$T = \Delta p A_D \quad (13)$$

$$\Delta p = \frac{1}{2} \rho (V_0^2 - u_1^2) \quad (14)$$

By using 2D-aerodynamics, the velocities and the loads on an airfoil illustrated in Figure 2.3 and Figure 2.4 can be studied.

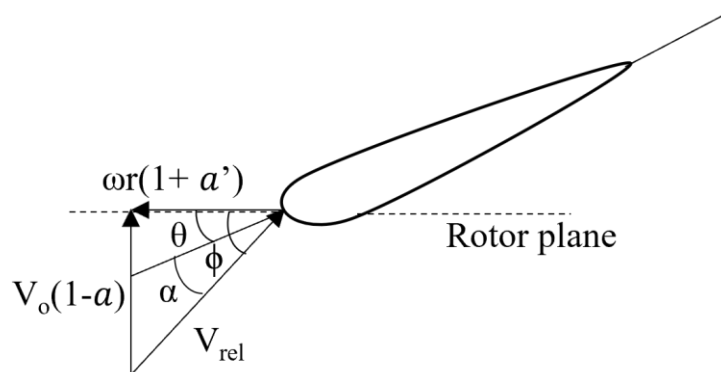


Figure 2.3 Velocities at the rotor plane. Hansen, (2015).

ω is the rotor speed and V_0 is the velocity of the incoming wind, giving a velocity ωr at the radius r . a is the axial induction factor and gives the ratio of wind velocity reduction, calculated from Equation (15).

$$a = \frac{V_0 - u_1}{V_0} \quad (15)$$

where u_1 is the wind speed at far side of the rotor as depicted in Figure 2.2.

a' is the rotational induction factor calculated from Equation 16.

$$a' = \frac{1 - 3a}{4a - 1} \quad (16)$$

The relative velocity, V_{rel} , is the speed that the blades experience. The flow angle, indicated by the letter ϕ , is the angle formed between the relative velocity and the rotor plane. This angle is comprised of two smaller angles, α and θ . The chord line is the straight line that connects the airfoil's trailing and leading edges. The angle between the chord line and the relative velocity is α , while the angle between the chord line and the rotor plane is θ .

The aerodynamic loads on a rotor are calculated using wind field data, blade geometry, drag and lift coefficients, and other inputs like the Reynolds number. Drag and lift force are the loads generated on an airfoil. The drag force, D , is caused by viscous forces and pressure differences and acts in the same direction as the relative velocity. The viscous forces in the boundary layer delay the flow. The lift force, L , is caused by the pressure difference by the uneven velocity of the airfoil and operates perpendicular to the relative velocity. The total force, R , may be divided into two components: a tangential force, P_T and a normal force, P_N . The thrust force on the rotor is contributed by P_N , while the component that moves the blade around in the rotor plane is P_T . Equations 17 and 18 may be used to compute these forces.

$$P_N = L \cos \phi + D \sin \phi \quad (17)$$

$$P_T = L \sin \phi - D \cos \phi \quad (18)$$

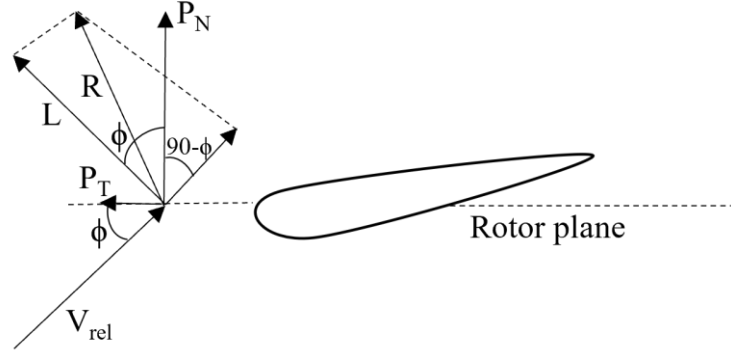


Figure 2.4 Loads at the rotor plane. Hansen, (2015).

Lift and drag coefficients, C_l and C_d are given as:

$$C_l = \frac{L}{\frac{1}{2} \rho V_\alpha^2 c} \quad \text{and} \quad C_d = \frac{D}{\frac{1}{2} \rho V_\alpha^2 c} \quad (19)$$

where V_α is the wind velocity, ρ is the air density, c is the length of the airfoil, and L and D are the lift and drag forces, respectively.

2.2.1 Blade Element Momentum (BEM) method

The blade element momentum (BEM) technique is a method for determining the steady loads and thrust force of a wind turbine with varying pitch angles and rotational speeds while subjected to variable wind speeds. The following assumptions must be made for this technique to be valid from Hansen, (2015):

- There is no radial dependence, thus what happens at one element is not sensed by the others.
- In each concentric element, the force exerted by the blades on the flow is constant; this corresponds to a rotor with an unlimited number of blades.

Generally, there are 8 steps to summarize the BEM method which are as follows from Hansen, (2015):

1. Initialize a and a' , typically $a = a' = 0$
2. Compute the flow angle, ϕ , using Equation 20.

$$\phi = \arctan\left(\frac{(1-a)V_0}{(1+a)\omega r}\right) \quad (20)$$

3. Calculate the local angle of attack, α , using Equation 21 where θ is the local pitch of the blade.

$$\alpha = \phi - \theta \quad (21)$$

4. Find $C_l(\alpha)$ and $C_d(\alpha)$ from table.
5. Compute C_n and C_t from Equation 22.

$$C_n = C_l \cos \phi + C_d \sin \phi \quad \text{and} \quad C_t = C_l \sin \phi + C_d \cos \phi \quad (22)$$

6. Calculate a and a' from Equation 23.

$$a = \frac{1}{\frac{4 \sin^2 \phi}{\sigma C_n} - 1} \quad \text{and} \quad a' = \frac{1}{\frac{4 \sin \phi \cos \phi}{\sigma C_l} - 1} \quad (23)$$

where σ is the solidity defined as the fraction of the annular area in the control volume which is covered by blades found from Equation 24.

$$\sigma(r) = \frac{c(r)B}{2\pi r} \quad (24)$$

where B is the number of blades, $c(r)$ is the local chord and r is the radial position of the control volume.

7. If a and a' have changed more than a certain tolerance, then go back to step 2, else finish.
8. Compute the local loads on the segment of blades.

2.3 Hydrodynamic loads

A floating structure's hydrodynamic loads are calculated using a combination of Morison's equation and potential theory. A potential flow model may be used to calculate the added mass, damping, and wave excitation force of the system. Morison's equation may be used to calculate the drag force along the structure's hull. It is more practical to apply linear potential flow theory when investigating a prominent volume structure exposed to waves from a hydrodynamic standpoint. This can be utilized to address an issue involving wave-structure interaction. However, there are several underlying simplifications in this theory that must be considered as proposed by Atcheson et al. (2016).

- The free surface and the body boundary conditions are linearized.
- Flow separation and shear stresses which cause viscous effects are not considered.

- The flow is irrotational, fluid is incompressible, which leads to Equation 25 known as the Laplace equation.

$$\nabla^2 \Phi = 0 \quad (25)$$

where Φ is the velocity potential.

- It is assumed that the bottom is flat and uniform.
- All variables can be expressed as a complex amplitude time $e^{i\omega t}$, under these assumptions.

Equation 26 shows the velocity potential at any wave location in the fluid domain as a result of these simplifications.

$$\Phi = Re(\phi e^{i\omega t}) \quad (26)$$

where ϕ is the complex velocity potential, Re denotes the real part, ω is the angular frequency of the incident wave, and t is the time.

Some of the other boundary conditions described in Figure 2.5 from Pettersen, (2007) can also be introduced.

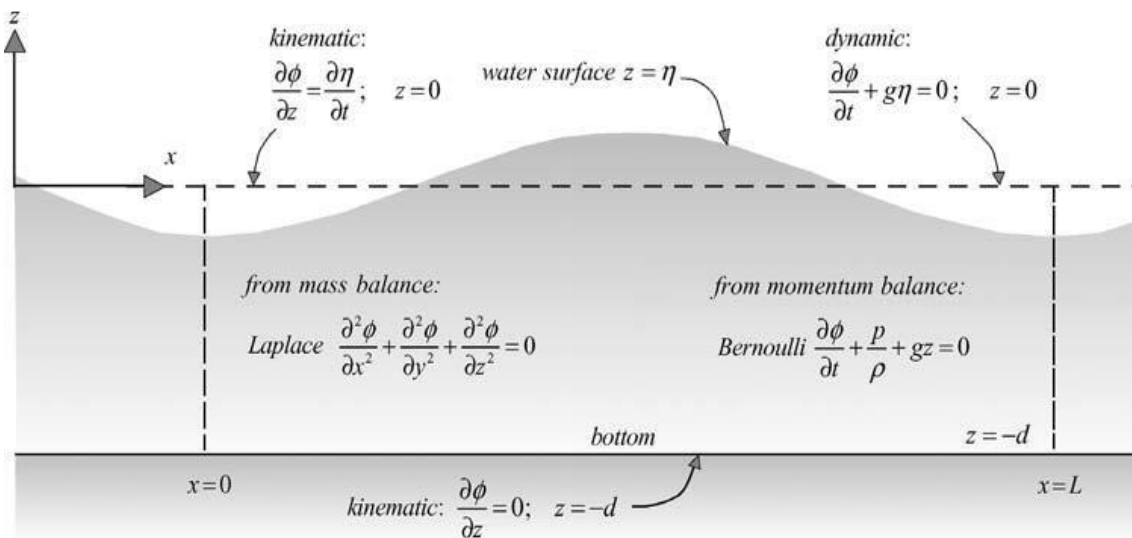


Figure 2.5 Boundary conditions of wave-structure interaction problem. Pettersen, (2007).

In regular waves, a hydrodynamic interaction issue is usually divided into two sub-problems, i.e., the diffraction problem and the radiation problem by Faltinsen, (1993).

- **Diffraction problem:** The forces and moments on the body when the structure is restrained from oscillating and there are incident regular waves. The resultant hydrodynamic loads are called wave excitation loads and are comprised of Froude-Kriloff and diffraction forces and moments.
- **Radiation problem:** In any rigid-body mode, the forces and moments on the body when the structure is forced to oscillate with the wave excitation frequency in the absence of incident waves. The resultant hydrodynamic loads are classified as damping, restoring, and added mass terms.

The steady-state hydrodynamic forces and moments caused by forced harmonic rigid body movements can be represented as added mass and damping (radiation problem). These forces and moments can be calculated by designating force components in x, y, and z direction as F_1 , F_2 , and F_3 , respectively. F_4 , F_5 , and F_6 are the moment components along the same axis. Equation 27 may be used to calculate the added mass and damping loads owing to harmonic motion's mode, η_j .

$$F_k = -A_{kj} \frac{d^2\eta_j}{dt^2} - B_{kj} \frac{d\eta_j}{dt} \quad (27)$$

Hydrostatic and mass considerations can be used to calculate the restoring forces of a freely floating structure. Equation 28 may be used to express the force and moment components.

$$F_k = -C_{kj}\eta_j \quad (28)$$

C_{kj} is the restoring coefficient of the body motion j on the specified direction of k and can be found from Equation 29.

$$\begin{aligned} C_{33} &= \rho g A_{wp} \\ C_{35} &= C_{53} = \iint_{A_{wp}} x ds \\ C_{44} &= \rho g V \overline{GM_T} \\ C_{55} &= \rho g V \overline{GM_L} \end{aligned} \quad (29)$$

where A_{wp} is the water plane area, $\overline{GM_T}$ and $\overline{GM_L}$ are the transverse and longitudinal metacentric height, and V is the displaced volume, respectively.

2.3.1 Wave loads on structures & Morison's equation

Wave loads on fixed slender offshore structures with circular cross-sections are calculated using Morison's Equation 30. As seen in Equation 30, the total force, F , is split into two components: mass force, F_M , and drag force, F_D .

$$dF = dF_M + dF_D = \rho \frac{\pi D^2}{4} C_M a_x dz + \frac{1}{2} \rho C_D Du |u| dz \quad (30)$$

where ρ is the density of water, D is the structure's diameter, C_M and C_D represents the mass and drag coefficients, and u and a_x are the velocity and the acceleration of the water particles, respectively.

The above-mentioned hydrodynamic coefficients are the function of Keulegan-Carpenter number, KC , Reynolds number, Re , and surface roughness. The Keulegan-Carpenter number and the Reynolds number can be estimated by Equation 31 and 32, respectively.

$$Re = \frac{\rho UD}{\mu} = \frac{UD}{\nu} \quad (31)$$

$$KC = \frac{UT}{D} \quad (32)$$

U represent the fluid velocity, D is the diameter of the structure, μ and ν are the dynamic and kinematic viscosity of the fluid, and T is the wave period.

2.3.2 Response of floating structures

The response of a floating structure to wave loads can be calculated using the equation of motion. Newton's second law may be used to construct the equation of motion for an uncoupled one DOF system, which yields Equation 33.

$$(M + A)\ddot{x} + C\dot{x} + Kx = F(t) \quad (33)$$

A is the added mass, M is the mass of the structure, C is the damping coefficient, K is the restoring coefficient, and $F(t)$ is the excitation force. x , \dot{x} and \ddot{x} are the displacement, velocity, and acceleration of the structure, respectively.

The diffraction problem yields the hydrodynamic excitation force. The added mass, damping and restoring coefficient, on the other hand, are determined by the radiation problem stated above.

2.4 Stability of floating structure

The hydrostatic properties of a floating structure are discussed in this section. The resistance to a slight deviation of tilting angle in a vertical direction is termed initial stability, which is an important measure to assess the stable state of the floating body. Station keeping devices are used to retain a floating structure in stable position and are typically divided into two categories: mooring and dynamic positioning. The following describes the basic theory of initial stability and mooring from Wen, (2018).

2.4.1 Initial Stability

The static equilibrium requirement for a floating structure must meet at least one of the following criteria: the magnitude of gravity and buoyancy forces must be equal, and the directions of forces must be opposite in line, as illustrated in Figure 2.6 from Wen, (2018). Archimedes' principle is used to calculate the buoyancy force. The body's center of buoyancy (COB) is the point at which the fluid pressure exerted across the submerged surface is simplified to a single resultant force. The center of mass of the displaced fluid is where the COB of a body is located.

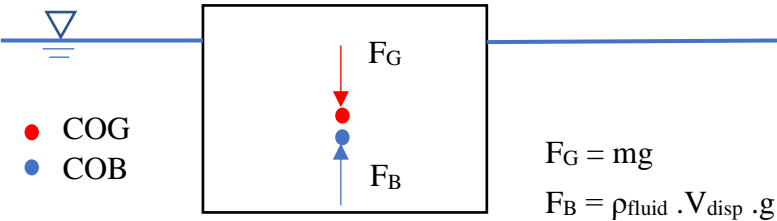


Figure 2.6 The buoyancy and gravity force in a submerged body. Wen, (2018)

The intrinsic capability of a floating body to withstand overturning loads and revert to its initial condition when the applied loads are withdrawn is referred to as initial stability. The illustration of the principal is taken from Wen, (2018) and is shown in Figure 2.7, which depicts the stability of a barge.

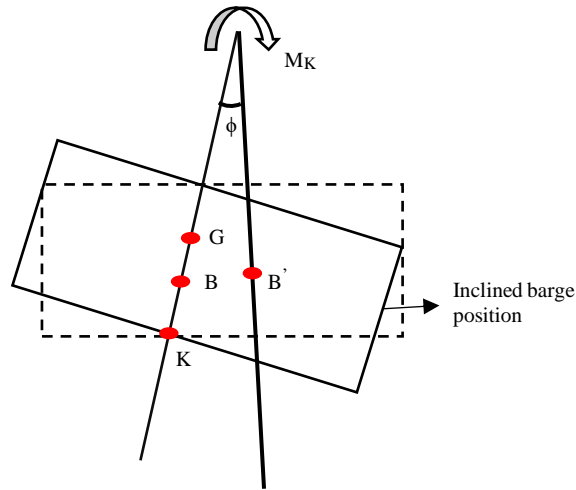


Figure 2.7 An illustration for the inclined barge position. Wen, (2018)

where G is the COG, B is the original position of the COB, B' is the inclined COB, ϕ is the inclination angle, K is the keel point and M_K is the moment that causes inclination.

The equation for the stability of the barge from geometry is given as:

$$\overline{GM} = \overline{KB} + \overline{BM} - \overline{KG} \quad (34)$$

\overline{GM} is the metacenter height which decreases as \overline{KG} increases, \overline{BM} is the metacenter radius which is the ratio of moment of inertia to the submerged volume (I/∇), \overline{KG} is the distance from COG to the keel point, and \overline{KB} is the distance between the COB and keel, which depends on the geometry of the submerge part.

The application criteria of \overline{GM} to evaluate the stability of the floating structure is: (a) $\overline{GM} > 0$: initial stability; (b) $\overline{GM} = 0$: neutral equilibrium; (c) $\overline{GM} < 0$: unstable equilibrium.

2.5 Mooring system

A mooring system utilizes mooring lines to keep a floating structure at sea in place relative to a fixed location on the seafloor. The two types of mooring systems are the catenary and taut mooring systems. This study uses the catenary mooring system for the CSC structure to offer sway, surge, and yaw motions restriction.

The shape of the mooring line is altered by the self-weight of a free-hanging chain catenary. The diagram below depicts the standard configuration of a catenary mooring line. The mooring geometry formula from Gudmestad, (2015) is written as follows:

$$y = \frac{H}{W} \left(\cosh \frac{W}{H} x - 1 \right) \quad (35)$$

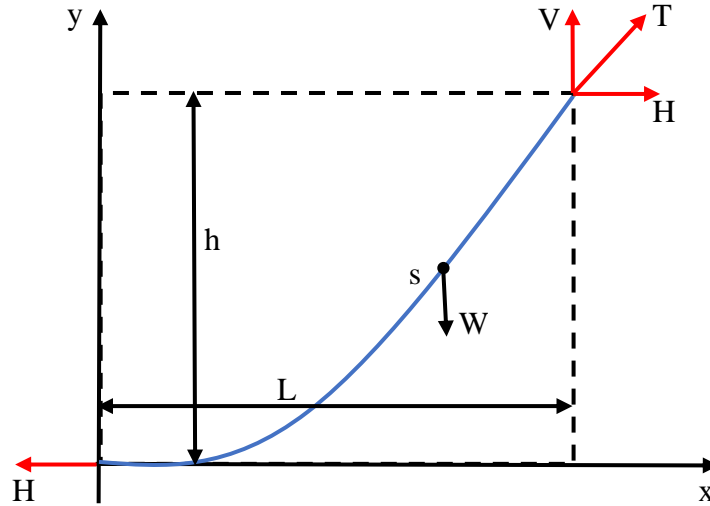


Figure 2.8 Standard layout of the catenary mooring. Gudmestad, (2015).

The following formulae from Gudmestad, (2015) can calculate the relevant forces and distance to the mooring arrangement. T is the mooring line tension; V is the tension's vertical component; H is the tension's horizontal component; S is the chain's length to the seafloor; L is the length from the point where the tension is applied to the seafloor; h is the water depth; W is the submerged weight per unit length of the hanging chain.

- Length of catenary:

$$S = \frac{H}{W} \left(\sinh \frac{W}{H} L \right) \quad (36)$$

- Water depth:

$$h = \frac{H}{W} \left(\cosh \frac{W}{H} L - 1 \right) \quad (37)$$

- Horizontal force:

$$H = \frac{W}{2h} (S^2 - h^2) \quad (38)$$

- Distance to touch down point:

$$L = \frac{H}{W} \cosh^{-1} \left(\frac{W}{H} h + 1 \right) \quad (39)$$

- Vertical force:

$$V = W \times S \quad (40)$$

- Tension:

$$T = \sqrt{H^2 + (WS)^2} \quad (41)$$

The static equilibrium of a segment in a catenary mooring line can be seen in Figure 2.9 from Kvamen, (2020).

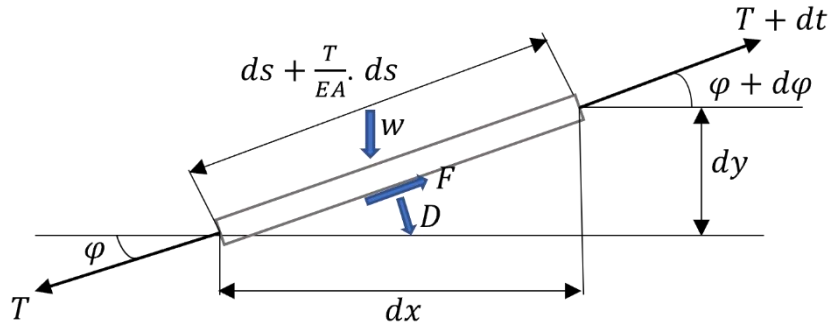


Figure 2.9 Static equilibrium of mooring line's segment. Kvamen, (2020)

The forces acting on the mooring line in the tangential and radial directions can be estimated by using the following two equations, respectively from Kvamen, (2020):

$$dT = \left[w \sin \varphi - F \left(1 + \frac{T}{EA} \right) \right] ds \quad (42)$$

$$T d\varphi = \left[w \cos \varphi + D \left(1 + \frac{T}{EA} \right) \right] ds \quad (43)$$

where the mean hydrodynamic forces per unit length operating in the tangential and normal directions are F and D , the mooring line's axial stiffness is EA , and the line tension is T , respectively.

3 METHODOLOGY

Firstly, numerical modeling of FWTs will be introduced in this section. SIMO-RIFLEX algorithm is used to perform a fully coupled aero-hydro-servo-elastic analysis in this thesis. Then, the modeling of a single CSC and dual CSC FWT will be discussed. The modeling of a shared mooring line and properties of single mooring lines is also presented. All the detailed procedures and initial settings are presented in the following sections.

3.1 Numerical modeling for FWTs

For dynamic study in the time domain of FWTs in a dual CSC configuration, a fully coupled simulation tool (SIMO-RIFLEX-BEM) is used. Floating structures' hydrodynamic loads are calculated by SIMO; BEM captures the aerodynamic loads on the blades according to the Blade Element Momentum method; RIFLEX is a nonlinear finite element solution with linkages to the BEM and an external controller for estimating dynamic structural reactions. The external controller is a Java-based proportional-integral generator torque controller used by Cheng, (2016). The controller aims to maximize power capture for the wind below the rated wind speed while maintaining a roughly constant power output for wind over the rated wind speed. In order to ensure the accuracy of the aero-hydro-servo-elastic simulator (SIMO-RIFLEX-BEM), several code-to-code checks have been performed (HAWC2, SIMO-RIFLEX-AC) and a comparison of models from Cheng et al. (2017) and Wang et al. (2013). The detailed setup of the dual CSC wind turbine configurations will be presented in the following sections, and the model of the single CSC can refer to Luan et al. (2016).

3.1.1 HydroD model

HydroD software can be used to calculate the floating structure's hydrodynamic parameters, wave loads, and motion response. The WADAM (Wave Analysis by Diffraction and Morison Theory) module from HydroD is used to extract kinetic parameters in the frequency domain, such as hydrostatic data, first-order wave force transfer function, retardation function, second-order wave drift force, etc., Imported HydroD data is used to create a SIMO model. The main procedure of dual CSC FWTs is presented as follows.

3.1.1.1 Hull model of a CSC FWT

The hydrostatic and hydrodynamic forces of a CSC's body are calculated using a panel model based on a potential theory. The wet surfaces of a body are represented by the quadrilateral or

triangular panels that make up a panel model. DNV's software, GeniE, another structure modeling software, is used to identify the wet surfaces of a panel model by placing a dummy load on the panel model. Generated using GeniE, a CSC structure with a mesh fineness of 1m long squares is shown in Figure 3.1.

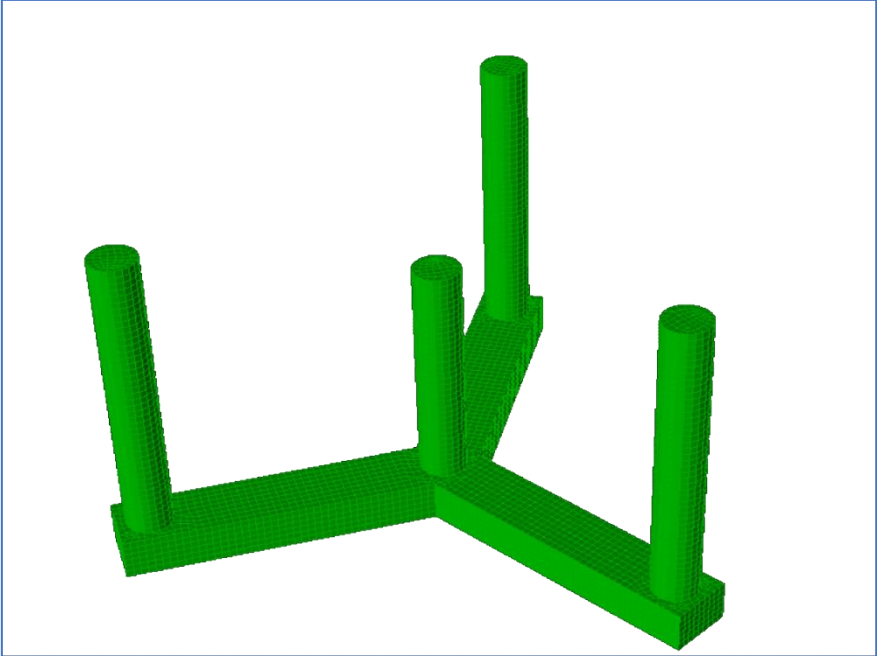


Figure 3.1 Mesh illustration of the hull of the 5-MW-CSC FWT in GeniE.

For the models in the present study, water depth of 200 m is used and twelve wave directions ranging from 0 to 360 deg with 30 deg intervals are employed to replicate the frequency domain analysis. Due to the axisymmetric nature of the CSC structure, the findings from 0 to 180 deg in wave direction will be identical to those from 180 to 360 deg. The frequency has also been chosen to undertake the frequency domain analysis. The simulation is allocated 39 wave frequencies ranging from 0.314 to 4 rad/s. The frequencies should be sufficient to guarantee that the simulation results are accurate.

The input coordinate system is specified for the "center of gravity centered system". The overall mass of the CSC hull should be assigned, which includes the weight of the CSC, ballast, and wind turbine. This mass model is initialized using the COG coordinates and gyration radius. The table below summarizes the total mass, COG, and radius of gyration values.

Table 3.1 Critical parameters of the mass model for a CSC.

| Item | | Unit | Value |
|--------------------|-----|------|----------|
| Total mass, M | | [kg] | 10558006 |
| COG coordinate | X: | | 0 |
| | Y: | [m] | 0 |
| | Z: | | -18.61 |
| Radius of gyration | RX: | | 31.53 |
| | RY: | [m] | 31.53 |
| | RZ: | | 27.93 |

Note: $RX = \sqrt{I_{xx}/M}$

In the WADAM configuration, a single body will be chosen. The loading condition is set to $z=0$, corresponding to the water surface. FEM model of the CSC (T1.FEM) is exported from GeniE and imported to the HydroD. The panel model of the CSC concept in HydroD is shown in Figure 3.2.

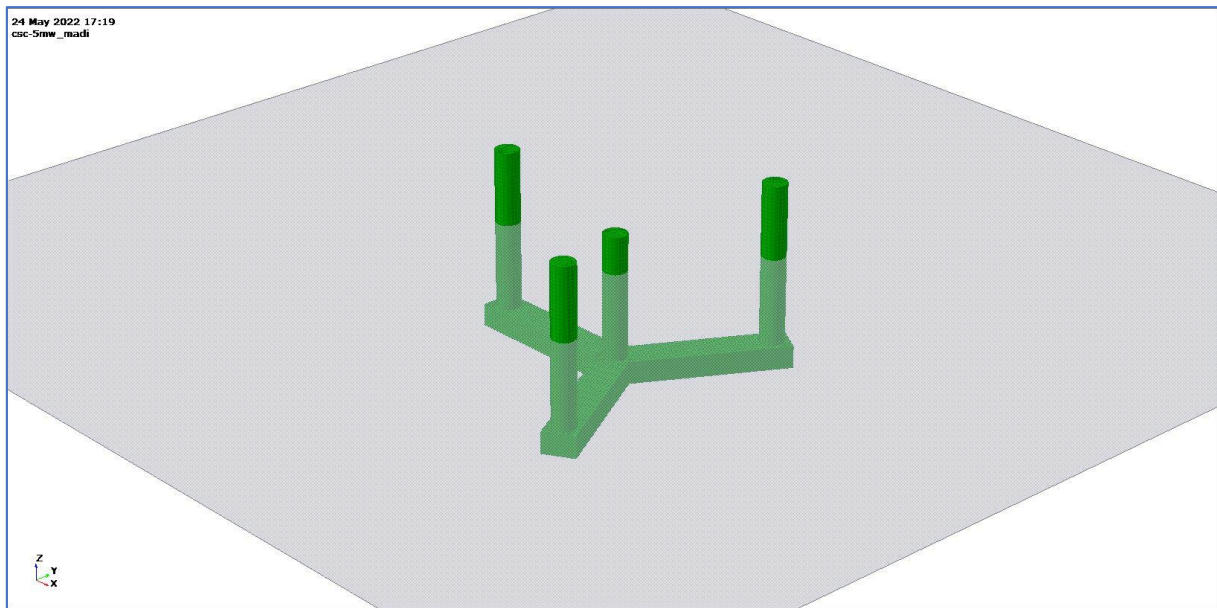


Figure 3.2 Panel model of a single CSC in HydroD.

Because of the significant distance between the two rigid bodies, the hydrodynamic coupling (added mass and damping) between the two FWTs is ignored. Figure 3.3, Figure 3.4, and Figure 3.5 show the response amplitude operators (RAOs) for surge, heave, and pitch DOFs in various wave directions from Munir et al. (2021).

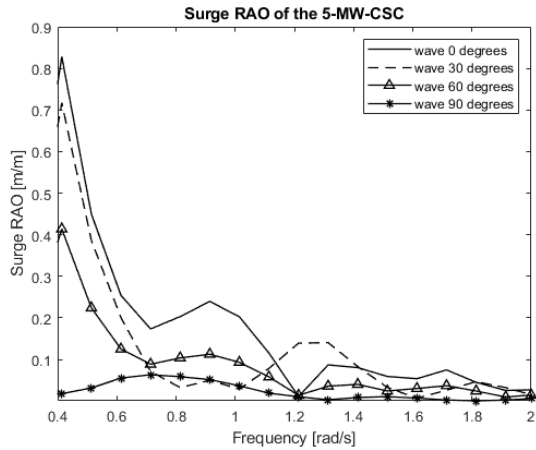


Figure 3.3 Surge RAO of the 5-MW-CSC. Munir et al. (2021)

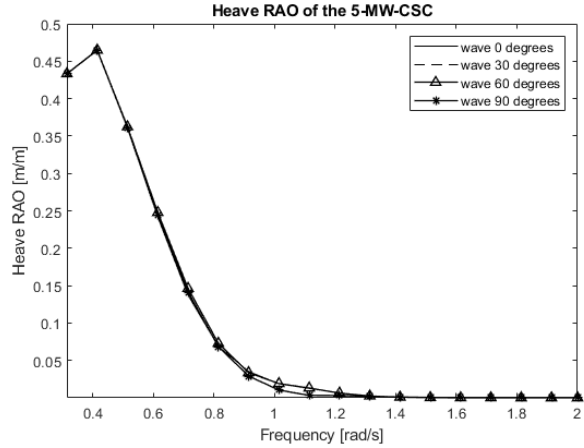


Figure 3.4 Heave RAO of the 5-MW-CSC. Munir et al. (2021)

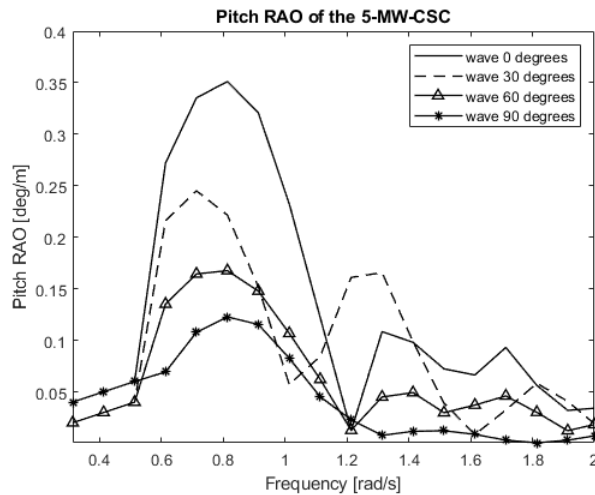


Figure 3.5 Pitch RAO of the 5-MW-CSC. Munir et al. (2021)

3.1.2 SIMO Model

For calculating hydrodynamic loads on a floating structure using time-domain analysis, SIMO is commonly employed. The floater is represented as a rigid body in SIMO, with first-order wave loads, second-order wave drift loads, and viscous drag force as the major hydrodynamic loads. The first-order wave loads are determined from the linear potential flow model. The Morison equation's viscous component and the quadratic drag force coefficient is used to compute the viscous drag forces.

Following the import of hydrodynamic characteristics from HydroD, certain parameters in SIMO require change. The primary reason for this is that the result from HydroD contains the

effects of the wind turbine, so it should be deleted in this stage to preserve the overall balance of the coupled simulation, as demonstrated in the following process.

To begin, the center of gravity, total mass, and moment of inertia for the CSC floater should be changed in the system description file by subtracting the weight of the wind turbine from the initial total mass. The table below summarizes the changed settings.

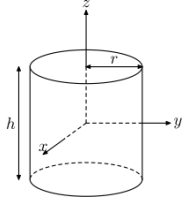
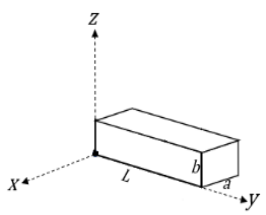
Table 3.2 Input properties for CSC body in SIMO.

| Item | | Unit | Value |
|-----------------|----------|-----------------------|----------------------|
| Total mass | | [ton] | 9,738 |
| COG coordinate | X: | | 0 |
| | Y: | [m] | 0 |
| | Z: | | -24.36 |
| Mass of inertia | I_{xx} | | 1.0851×10^7 |
| | I_{yy} | [ton*m ²] | 1.0851×10^7 |
| | I_{zz} | | 8.24×10^6 |

Note:

1. Global coordinate system is specified in body data.
2. The ballast part is simulated with a solid cylinder and rectangular section for calculating the mass of inertia, and the CSC is modeled with a thick wall structure. (Table 3.3).
3. In SIMO, the initial position (0,0,0) should be used as the reference point for computing the mass moment of inertia.

Table 3.3 Mass moment of inertia with different geometry.

| Type | Mass of inertia | Note |
|---|--|-----------------|
|  | $I_z = \frac{1}{2}mr^2$ $I_x = I_y = \frac{1}{4}mr^2 + \frac{1}{12}mh^2$ | Ballast and CSC |
|  | $I_x = \frac{1}{12}ma^2 + \frac{1}{3}mL^2$ $I_y = \frac{1}{12}mb^2 + \frac{1}{3}mL^2$ $I_z = \frac{1}{12}m(a^2 + b^2)$ | Ballast and CSC |

Seven slender elements are added to SIMO to determine the drag force of the submerged CSC using the Morison equation. Three to support the bottom pontoons, three for the side columns, and one to support the central column. The quadratic drag coefficients in the transverse direction should be placed on the sides of the CSC (parallel to the flow), and a quadratic term in the longitudinal direction should be placed on the bottom of the CSC to reflect the drag impact during heave motion.

Table 3.4 Quadratic drag force coefficients in SIMO for slender elements.

| No | z | x | L | D | a | b | C_D | C2x | C2y | C2z |
|----|-------|------------|-------|-----|-----|-----|-------|------------------------------------|------------------------------------|------------------------------------|
| | [m] | [m] | [m] | [m] | [m] | [m] | [-] | [Ns ² /m ³] | [Ns ² /m ³] | [Ns ² /m ³] |
| 1 | 0~-24 | - | 24 | 6.5 | - | - | 0.5 | - | 1666 | 1666 |
| 2 | 0~-24 | - | 24 | 6.5 | - | - | 0.5 | - | 1666 | 1666 |
| 3 | 0~-24 | - | 24 | 6.5 | - | - | 0.5 | - | 1666 | 1666 |
| 4 | 0~-24 | - | 24 | 6.5 | - | - | 0.5 | - | 1666 | 1666 |
| 5 | - | 3.25~45.5 | 42.25 | - | 9 | 6 | 1.9 | - | 5842.5 | 8763.75 |
| 6 | - | 2.8~39.4 | 42.25 | - | 9 | 6 | 1.9 | - | 5842.5 | 8763.75 |
| 7 | - | -2.8~-39.4 | 42.25 | - | 9 | 6 | 1.9 | - | 5842.5 | 8763.75 |

Note:

1. In SIMO, the load type should be set to "gravity and buoyancy not included."
2. "DNV-RP-C205 (2010) Table E-1" may be used to determine the drag coefficient (C_D).
3. The quadratic drag force per unit length, C2x, is in the cylinder's longitudinal direction; C2y/C2z is in the cylinder's transverse direction, as determined by the formula: $C2x = (1/2)\rho_{sea}DC_D$, where D denotes the diameter of the cylindrical columns and ρ_{sea} denotes 1025 kg/m³. Instead of the diameter, for rectangular pontoons, the reference length (a or b) from Table 3.3 will be utilized. The reference length used is determined by the direction of the applied drag force.

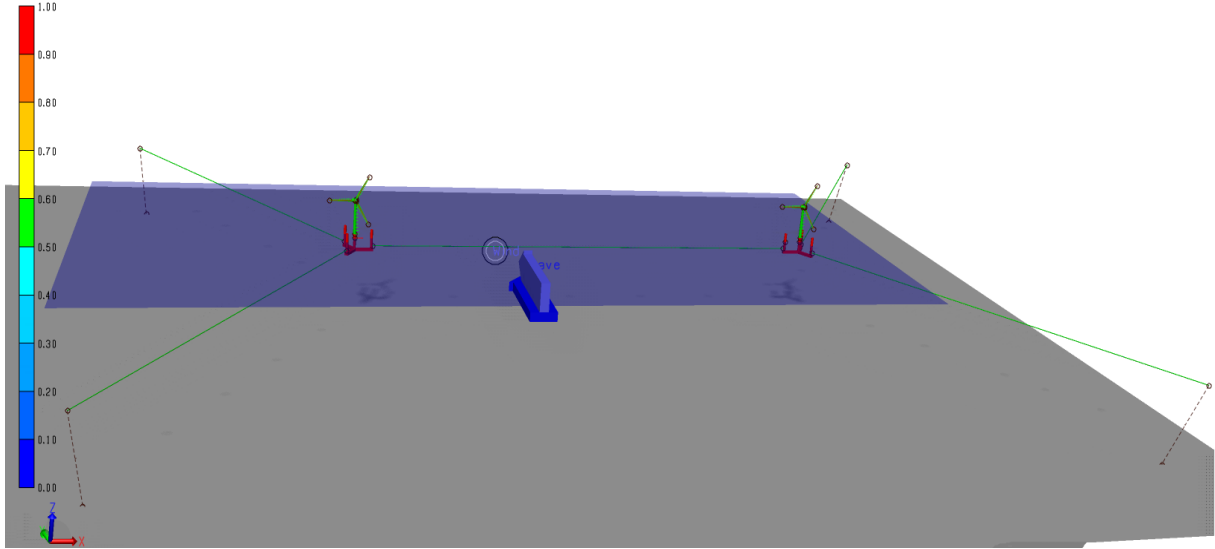


Figure 3.6 Dual CSC FWTs model in SIMA.

A SIMA model of dual CSC FWTs is illustrated in above Figure 3.6. Additionally, a defined upward force is provided at the system's bottom (0, 0, -22.425) to counteract the gravitational effect of the wind turbine and mooring lines. The specified upward force is equal to 7300 kN.

When a floater is free-floating, the restoring forces are determined by hydrostatic and mass parameters. In SIMO, the linear stiffness matrix is a 6x6 matrix that determines the stiffness in various DOFs. Similarly, the turbine's weight should be eliminated, thus, the matrix properties need to be modified. C_{33} , C_{44} , and C_{55} in heave, roll, and pitch motions are the only non-zero terms for the CSC as a symmetry plane for the submerged volume as described by Faltinsen, (1993). The table below summarizes the stiffness matrix.

Table 3.5 Linear stiffness coefficients for the CSC.

| Stiffness term | Unit | Value |
|--|-------|---------------------|
| $C_{33} = \rho_{sea}gA_{wp}$ | [N/m] | 1.319×10^6 |
| $C_{44} = \rho_{sea}g\nabla GM_T$ | [Nm] | 1.035×10^9 |
| $C_{55} = C_{44} = \rho_{sea}g\nabla GM_L$ (a symmetric plane) | [Nm] | 1.035×10^9 |

Note:

1. A_{wp} is the water plane area of the CSC.
2. ∇ is the submerge volume.
3. GM_T and GM_L is the metacenter height in transverse and longitudinal direction.

3.1.3 RIFLEX model

RIFLEX is a finite element solver designed to analyze mooring lines and other slender structures from RIFLEX by SINTEF Ocean, (2017). The RIFLEX is used to model the FWT system, including the blades, tower, shaft, and mooring system. Beam elements are used to depict the blades, tower, and shaft. The bar elements represent the mooring line. The mooring line configurations in the CSC model are based on the specifications of the spread mooring system (see Sections 3.2.1.1 and 3.2.3.1).

Mooring line configuration in CSC is mostly determined by a static analysis regulated by water depth, catenary length, and submerged hanging chain length. Chapter 2 and Appendix B include the theoretical section and the calculation results. At first, the stress-free configuration of the mooring lines should be specified, after which it will be fed into the RIFLEX model for static simulation. RIFLEX should be used to specify the final anchor positions listed in Table 3.9.

All three distinct CSC models, on the other hand, have a similar tower, shaft, and mooring line parameters due to the same CSC structure and wind turbine specifications.

3.2 Floating wind turbine models

3.2.1 Single CSC model

The wind turbine floater used in this project was developed and explained by Luan et al. (2016). The 5-MW-CSC comprises a rotor nacelle assembly, tower, hull, and mooring system, as shown in Figure 3.7. An NREL 5-MW FWT is used for all models, and its specifications provided by Jonkman et al. (2009) are listed in Table 3.7. A central column, three side columns, and three pontoons make up the hull of the 5-MW-CSC. The pontoons link the side columns to the central column at the bottom to create a unified structure. The pontoons contribute most of the additional mass in the heave, roll, and pitch. Heave plates and bracings are not present. The pontoons' box-shaped cross-section might provide significant viscous damping at heave, roll, and pitch resonant frequencies. The dimensions of a 5-MW- single CSC FWT are shown in Figure 3.8 and Figure 3.9 and presented in Table 3.6.

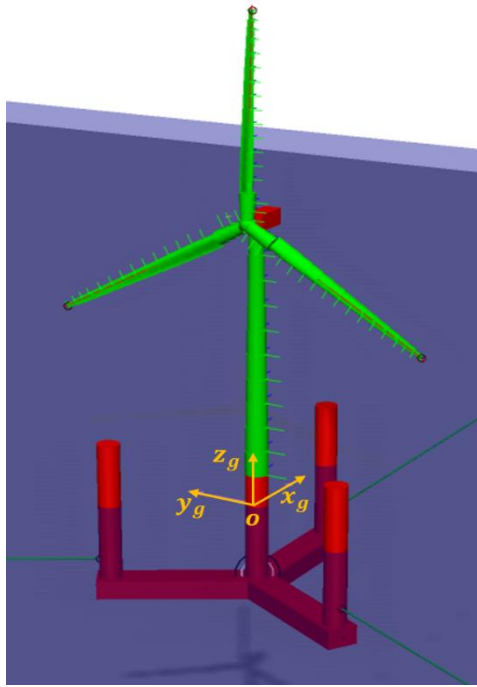


Figure 3.7 A 5-MW-CSC single FWT model. Luan et al. (2016)

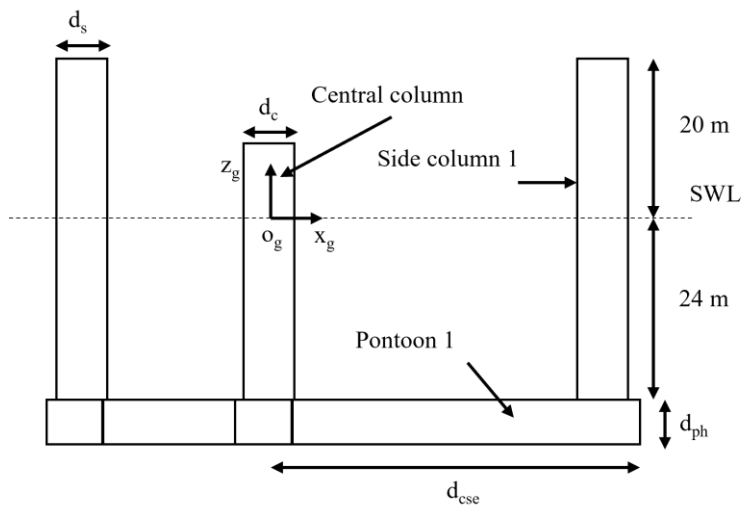


Figure 3.8 Side view of the hull of 5-MW-CSC. Luan et al. (2016)

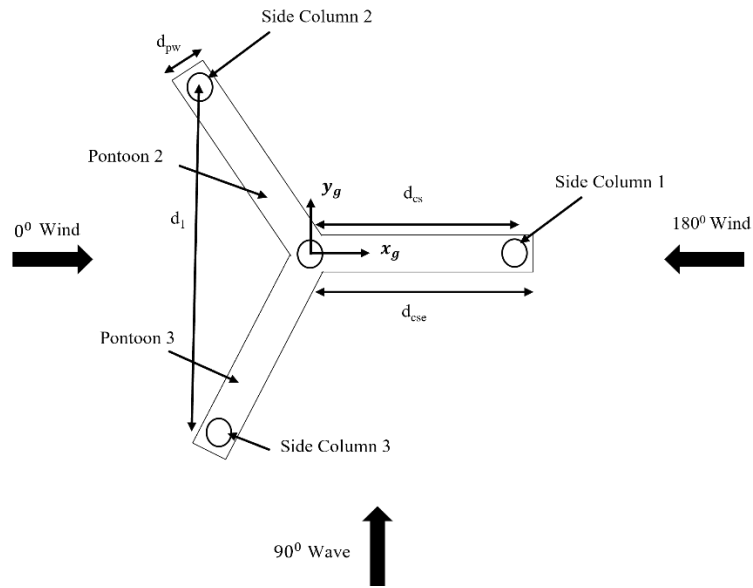


Figure 3.9 Top view of the hull of 5-MW-CSC. Luan et al. (2016)

Table 3.6 Dimensions of the hull of the 5-MW-CSC by Luan et al. (2016).

| Item | Unit | Value |
|--|---------|--------|
| d_c | [m] | 6.5 |
| d_s | [m] | 6.5 |
| d_{ph} | [m] | 6 |
| d_{pw} | [m] | 9 |
| d_{cs} | [m] | 41 |
| d_{cse} | [m] | 45.5 |
| Distance between top of the central column and SWL | [m] | 10 |
| Operating draft | [m] | 30 |
| Displacement | [tonne] | 10,555 |
| Steel weight (hull) | [tonne] | 1,804 |
| Equivalent thickness | [m] | 0.03 |

Table 3.7 Specifications of the NREL 5-MW wind turbine. Jonkman et al. (2009)

| Item | Unit | Value |
|------------------|-------|-------|
| Rated power | [kW] | 5000 |
| Rotor diameter | [m] | 126 |
| Hub height | [m] | 90 |
| Rated wind speed | [m/s] | 11.4 |

| | | |
|------------------------|---------|-------------------|
| Cut-in wind speed | [m/s] | 3 |
| Cut-out wind speed | [m/s] | 25 |
| Drivetrain | [-] | Geared |
| Control | [-] | Pitch regulated |
| Accumulated mass | [kg] | 2.4×10^5 |
| Rated rotational speed | [rad/s] | 122.91 |

The body-fixed coordinate system (x_b, y_b, z_b) coincides with the global coordinate system (x_g, y_g, z_g) when the 5-MW-CSC is at its mean position.

The ballast arrangement for the operating draft is shown in Figure 3.10. The ballast mass is distributed symmetrically around the center column's central line. The completely filled pontoons with ballast water is used to achieve the operational draft from Luan et al. (2016). Meanwhile, there is no ballast water in the central column. The ballast water pressure head in each side column is 7.7 m measured from the pontoon's top.

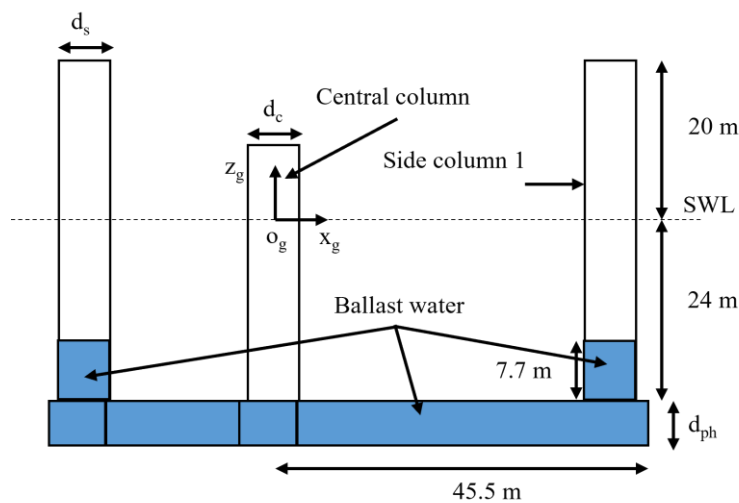


Figure 3.10 Ballast arrangement. Luan et al. (2016)

The mooring system is composed of three catenary chain mooring lines spread symmetrically at 120 deg about the z_g -axis of the platform, as illustrated in Figure 3.11. Chain mooring lines are represented as an evenly distributed mass with a solid cross-section as described in Luan et al. (2016).

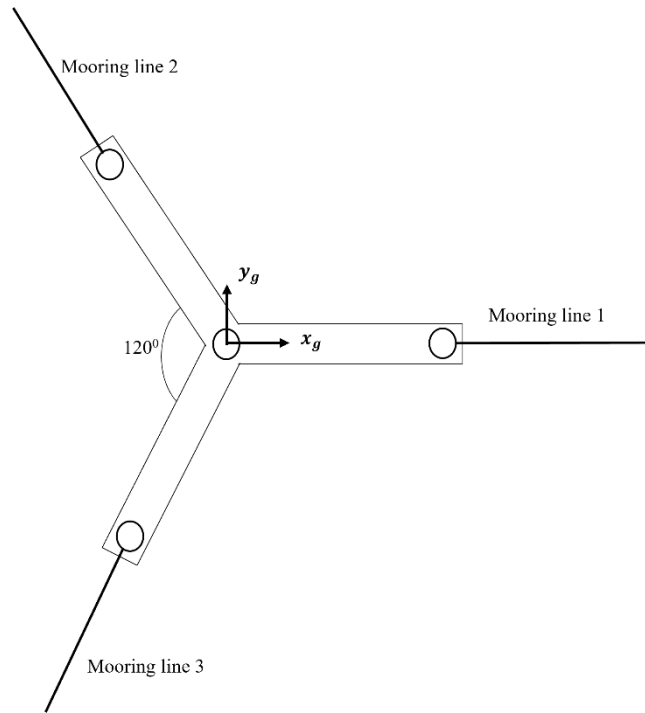


Figure 3.11 Mooring configuration for single CSC FWT.

3.2.1.1 Single mooring line modeling

To provide sufficient restoring force to floating platforms in various environmental conditions, station-keeping devices like mooring lines are used. Three catenary chain mooring lines are spread symmetrically at 120 deg around the platform z-axis in the case of a single CSC FWT, as shown in Figure 3.11. The same configuration is employed in the present study for a single mooring lines design in which each FWT is modeled with two side catenary chain mooring lines spread at 120 deg and one shared line as described by Munir et al. (2021). The configuration and properties of single mooring lines for single CSC floater and dual CSC FWTs are based on the specifications from Luan et al. (2016) and are listed in Table 3.8. Two single mooring lines are connected to each FWT through fairleads. The fairleads and anchor points are represented as supernodes to specify both ends of a mooring line. Each mooring line is made up of finite elements (FEs) with certain cross-sectional characteristics. In the present model, FE modeling of each single mooring line utilized 30 bar elements with a total length of 1073 m. The initial arrangement of the single mooring line is illustrated in Figure 3.12.

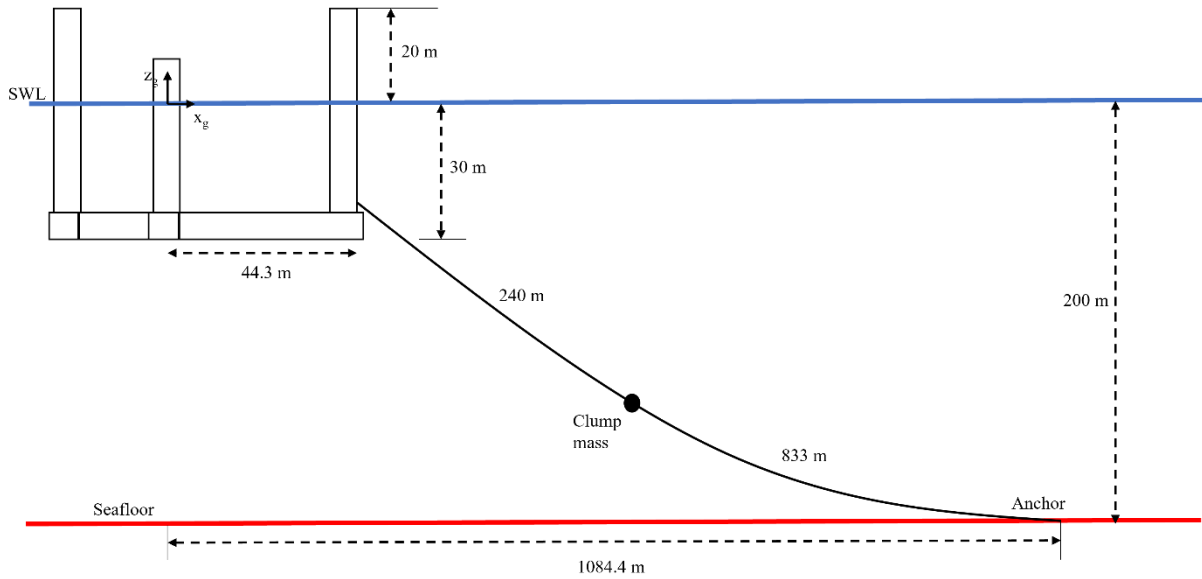


Figure 3.12 Single mooring system diagram for the single CSC and dual CSC FWTs.

Table 3.8 Design parameters of a single mooring system by Luan et al. (2016).

| Item | Unit | Value |
|--|----------------------|--------------------|
| Mooring type | [-] | Chain |
| Mooring line mass density | [kg/m] | 115 |
| Pretension at the fairlead | [kN] | 1,686 |
| Un-stretched mooring line length | [m] | 1,073 |
| Mooring line diameter | [m] | 0.137 |
| Depth of fairlead below sea water line | [m] | 18 |
| Density of the material | [kg/m ³] | 7,850 |
| Clump weight in water | [kg] | 15,000 |
| Extensional stiffness of mooring line | [kN/m] | 3.08×10^6 |
| Distance of the clump weight from the fairlead to the attachment point | [m] | 240 |
| Quadratic drag coefficient | [-] | 1.2 |

For dual CSC models in the present study, the static equilibrium position of the FWTs is kept constant at the mean position by changing the position of the anchors for three different configurations of dual CSC models as discussed in Section 3.2.2. The global arrangement of the anchors in all three different configurations of dual CSC is listed in Table 3.9.

Table 3.9 Arrangement of fairleads and dual CSC mooring line anchors in global coordinate system.

| Fairlead | x_g | y_g | z_g |
|----------|--------|-------|-------|
| 1 | 44.3 | 0 | -18 |
| 2 | -22.1 | 38.3 | -18 |
| 3 | -22.1 | -38.3 | -18 |
| 4 | 1124.3 | 0 | -18 |
| 5 | 1190.7 | 38.3 | -18 |
| 6 | 1190.7 | -38.3 | -18 |

| Anchors | Model 1 | | | Model 2 | | | Model 3 | | |
|---------|---------|--------|-------|---------|--------|-------|---------|--------|-------|
| | x_g | y_g | z_g | x_g | y_g | z_g | x_g | y_g | z_g |
| 2 | -542.2 | 939.1 | -200 | -532.4 | 939.1 | -200 | -556.2 | 939.1 | -200 |
| 3 | -542.2 | -939.1 | -200 | -532.4 | -939.1 | -200 | -556.2 | -939.1 | -200 |
| 4 | 1670.8 | 939.1 | -200 | 1661.3 | 939.1 | -200 | 1685.1 | 939.1 | -200 |
| 5 | 1670.8 | -939.1 | -200 | 1661.3 | -939.1 | -200 | 1685.1 | -939.1 | -200 |

The single mooring lines 2 and 3 are symmetric to mooring lines 4 and 5 because of the same properties and symmetric arrangement along the z_g -axis. Therefore, only the line shapes of mooring line 2 and mooring line 4 are depicted in Figure 3.13 for all the configurations of dual CSC FWTs.

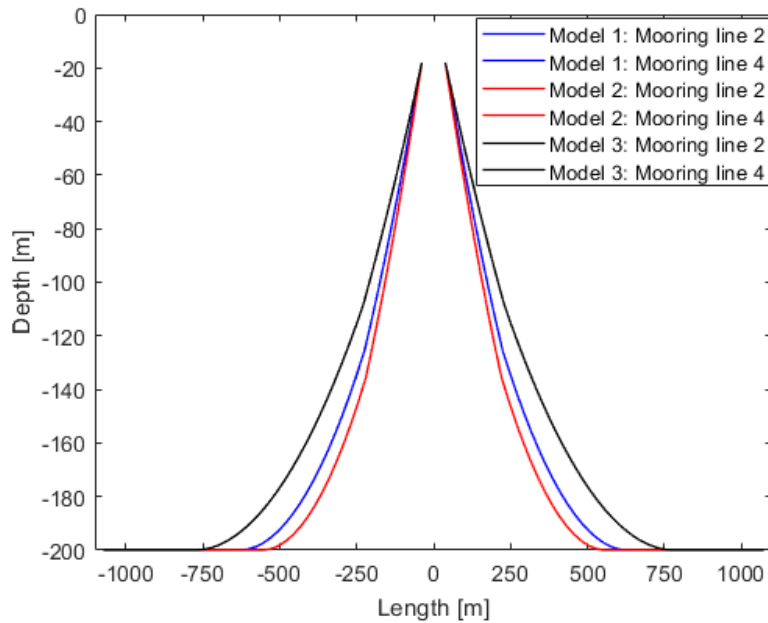


Figure 3.13 Single mooring line shape for three different configurations of dual CSC FWTs.

3.2.2 Dual CSC model with varying static equilibrium position

The motivation for modeling dual CSC FWTs is taken from the initial study in Munir et al. (2021) and is attached in Appendix A. This section mainly describes the modeling methodology from Munir et al. (2021). Two single CSC FWTs were connected with a shared mooring line. First of all, one single mooring line was removed from each FWT and connected with a shared line. Two different configurations of FWTs were studied by placing them horizontally at an equidistant offset of 6 and 8 rotors diameter distance. This leads to two different lengths of a shared line with distinct static equilibrium positions of FWTs. Compared to a single CSC model, platforms were rotated by 30 deg and -30 deg for FWT 1 and FWT 2 to accommodate the length of a shared line. Because of this, FWTs were rotated by 90 deg and always faced the upwind direction parallel to the rotor plane. This configuration leads to higher restoring stiffness of single mooring lines in the sway direction than in the surge direction. Like in the present study, basic catenary equations were used to design the single and shared mooring lines.

3.2.3 Dual CSC model with constant static equilibrium position

In the present study, some more modifications have been done to the model in Munir et al. (2021). Instead of two configurations of FWTs with different static equilibrium positions, three varying configurations of FWTs are studied with a constant static equilibrium position. With three configurations, the length of a shared line is also different. The anchor points of single mooring lines for each FWTs are also changed so that the varying shared line lengths do not affect the static position of FWTs. In the present configurations, two FWTs are rotated and placed at an equidistant horizontal offset of 9 rotors diameter distance along the x_g -axis in the global coordinate system. FWTs adjust their position around the constant mean static position at 9 rotors diameter distance for all the lengths of a shared line in three different configurations. This is done to analyze the behavior of FWTs placed horizontally with constant distance among them and varying shared line lengths. The properties of single mooring line described in Section 3.2.1.1 and shared mooring line in Section 3.2.2.1 are also modified to be consistent with a single CSC model. The FWTs face the upwind direction, as shown in Figure 3.14. The shared mooring line is positioned along the sway (y_g) direction in the present model as in Munir et al. (2021). Two single mooring lines are connected through fairleads to each FWT. The properties of the dual CSC FWTs with three different configurations are listed in Table 3.10.

Table 3.10 Dual CSC FWTs properties.

| Item | | Unit | Value |
|--|---|------|----------------|
| Static mean position of three configurations | <i>FWT 1</i> | [m] | (0, 0, 0) |
| | <i>FWT 2</i> | | (1128.6, 0, 0) |
| | <i>Model 1</i> | | 1168.6 |
| Initial distance between the wind turbines | <i>Model 2</i> | [m] | 1193.6 |
| | <i>Model 3</i> | | 1143.6 |
| | Constant static offset for three configurations | | [m] |

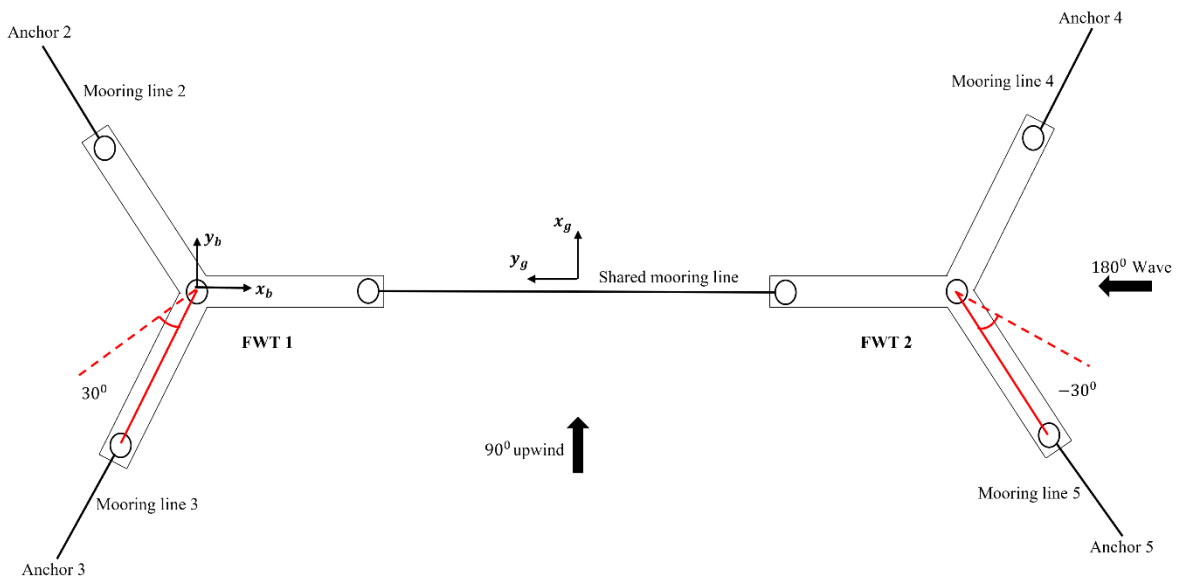


Figure 3.14 Illustration of dual CSC FWTs configuration from Munir et al. (2021).

3.2.3.1 Shared mooring line modeling

A shared mooring line is modeled to keep the two FWTs at their mean position with no wind and waves. The same modeling methodology for shared mooring line is adopted as discussed in Munir et al. (2021). Two FWTs are connected with a shared line through fairleads. When the fairleads are on the same level, basic catenary equations are applicable for shared mooring line design. A mooring line can be modeled by connecting two symmetric lines at the sagging point. To model the shared line effectively, various assumptions are made such that the current forces, bending effects, and dynamic effects on mooring lines can be ignored, as proposed by Liang et al. (2020).

The catenary plane is defined first for modeling the shared line, as illustrated in Figure 3.15. A mooring line's catenary plane is the vertical plane determined by the form of the catenary line. The fairleads serve as the origin of the catenary plane, as shown in Figure 3.15. The elastic catenary equations, Equation 44 and Equation 45 are implemented by making one end of the shared line the origin of a catenary plane as described by Faltinsen, (1993).

$$x = \frac{H}{W} \log \left(\frac{\sqrt{H^2 + V^2} + V}{H} \right) + \frac{H}{EA} s \quad (44)$$

$$h = \frac{1}{2} \frac{W s^2}{EA} + \frac{H}{W} \left[\frac{1}{\cos \phi} - 1 \right] \quad (45)$$

where x and h are the horizontal and vertical distance of the sagging point measured from the fairlead, H and V are the horizontal and vertical components of the mooring tension T at the fairlead, s is the total suspended length of the shared line, W is the weight per unit length of the mooring line in water, EA is the extensional stiffness of the line with E as the elastic modulus and A is the cross-sectional area.

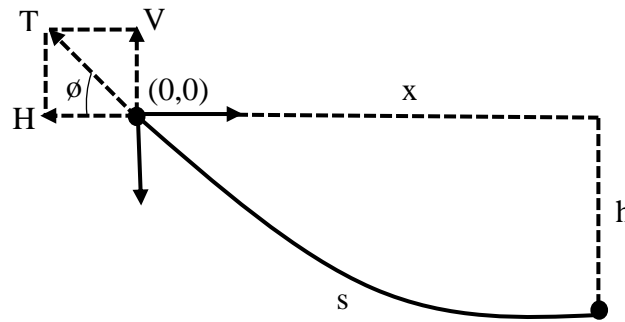


Figure 3.15 Illustration of catenary plane of the shared line. Liang et al. (2021)

The final suspended length may be solved by iteration after the distance between the fairlead and the sagging point is known with an initial approximation of s and h . The tension at the fairleads, as a result, may then be computed. By adjusting the vertical distance of the sagging point, the tension of the shared mooring line is modified to achieve horizontal force balance. The shared mooring line is modeled with two clump weights at an equidistant offset from the fairleads at each end. This is done to provide initial pre-tension to avoid the rolling of FWTs. Also, in the present model, three configurations of FWTs with varying shared line lengths are studied. This approach analyzes the effect of changing shared line length on structures' restoring stiffness. Figure 3.16 shows the arrangement of the shared mooring line with clump

weights in the present study. Properties of shared mooring line with different lengths are listed in Table 3.11.

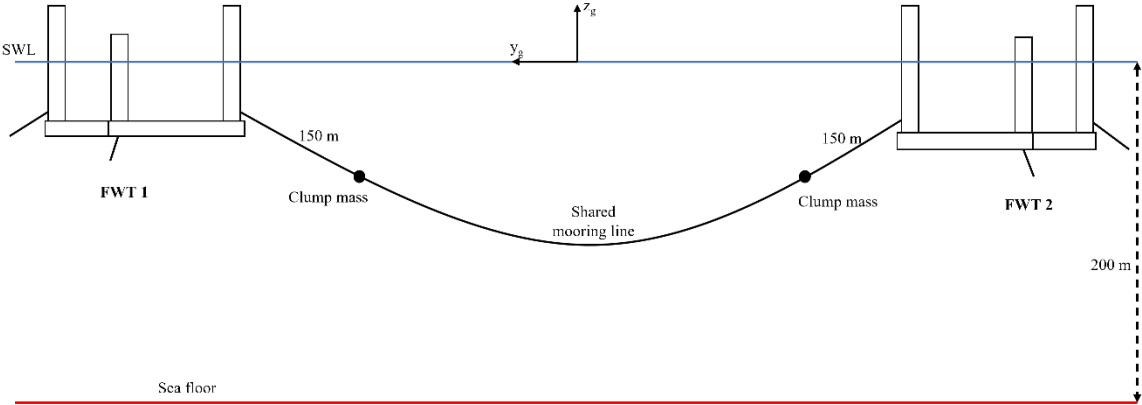


Figure 3.16 Arrangement of shared mooring line with clump weights in the present study.

Table 3.11 Properties of shared mooring line with varying configurations.

| Item | | Unit | Value |
|--|----------------|--------|--------------------|
| Mooring line type | | [-] | Chain |
| Mass density | | [kg/m] | 115 |
| Diameter | | [m] | 0.137 |
| | <i>Model 1</i> | | 1080 |
| Un-stretched length | <i>Model 2</i> | [m] | 1105 |
| | <i>Model 3</i> | | 1055 |
| Clump weight | | [kg] | 30,000 |
| Distance of clump weight from adjacent fairleads | | [m] | 150 |
| Extensional stiffness | | [N] | 3.08×10^9 |
| Quadratic drag coefficient | | [-] | 1.2 |

Note: Most of the shared mooring line properties are kept the same as the single mooring line to have a better comparison with the single CSC model.

The line shape comparison for different lengths of a shared mooring line in a catenary plane is illustrated in Figure 3.17.

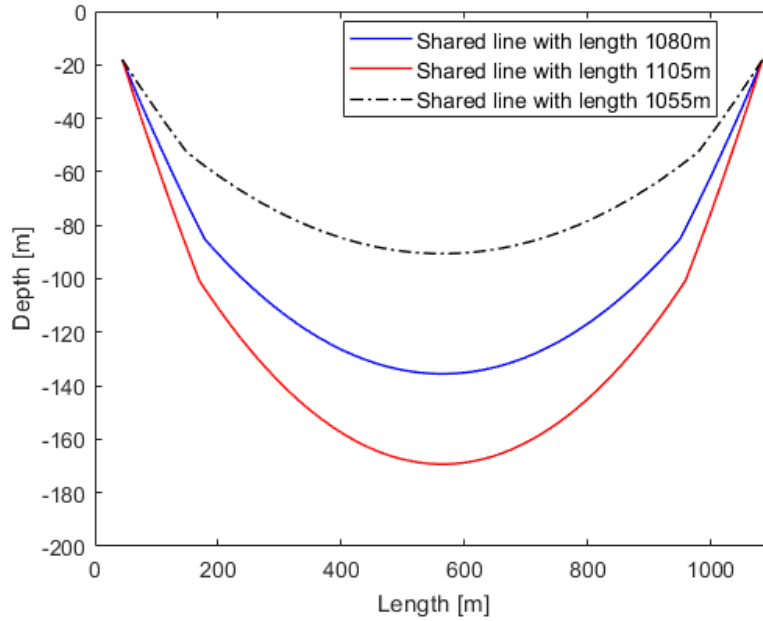


Figure 3.17 Shared mooring lines shape for three different configurations of dual CSC FWTs.

3.3 Coordinate system

In the present thesis, several platform specifications refer to the global coordinate system. X_g , y_g represent the set of orthogonal axes, with the sea water line (SWL) defined with the xy -plane and the z_g axis directed upward along the centerline of the CSC floater. Surge direction is always parallel to the direction of incident wind, and sway direction is lateral to the left when looking downwind. The direction of x_g , y_g , and z_g axis in relation to the structure in the case of a single CSC model is shown in Figure 3.7. The rigid body platform DOFs include surge, sway, and heave as translational motions while roll, pitch, and yaw are rotational. In the case of a single CSC FWT, the positive direction of surge (x_g) is the 0 deg direction of incident wind and wave. In contrast, the positive direction of sway (y_g) is the 90 deg direction of the incident wave, as shown in Figure 3.9.

On the other hand, the surge and sway motions of the dual CSC FWTs are 90 deg out of phase with the single CSC model. In contrast to the single CSC model, the platforms of the dual CSC model are rotated by 30 deg and -30 deg for FWT1 and FWT2 to accommodate the shared mooring line, as shown in Figure 3.14. As a result of this, the FWTs are rotated by 90 deg. With this configuration of dual CSC FWTs, the positive surge (x_g) is along with the 90 deg incident wind and wave direction, whereas the sway (y_g) is along the 180 deg incident wave direction, as illustrated in Figure 3.14.

4 RESULTS AND DISCUSSIONS

This chapter deals with the simulation results and related discussion for all models of the dual CSC i.e., Model 1, Model 2, and Model 3. It also includes the summary of results from Munir et al. (2021) regarding the influence of the varying distance between the FWTs on dynamic responses. Furthermore, investigation of natural periods from decay tests, the effect of different mooring configurations on restoring stiffness of the structure, mooring tension and restoring study, and finally, a comparative analysis of dynamic responses in six DOFs as a result of listed environmental conditions is presented. It is assumed that the FWTs are always facing parallel to the incident wind coming from all directions. Detailed comparison and analysis are provided in the following sections.

4.1 Global analysis of FWTs with varying static equilibrium position

This section summarizes the effect of varying shared mooring line lengths and horizontal distance between the FWTs on dynamic responses from Munir et al. (2021). The study by Munir et al. (2021) was carried out to analyze the responses of FWTs with waves coming from 0 deg to 180 deg against the responses of a single CSC. FWTs were placed at 750 m and 1000 m in the first and second configuration of dual CSC model. The wind is constantly directed in positive x_g -direction into the rotor plane of the FWTs. In order to assess the global responses of FWTs, one operational loading condition above the rated wind speed for the wind-dominant case and one extreme loading condition for the wave-dominant case with parked FWTs was considered as listed in Appendix A. For each platform's DOF, the most significant wave direction was selected, and the corresponding average statistical properties were discussed and compared.

It was found that both FWTs experienced higher maximum and lower minimum surge and sway motion. This suggests that in the surge and sway direction, mooring restoring stiffness is decreased. This can be attributed to the reduction of one anchor fixed mooring line from each FWT compared to a single CSC with three anchor fixed single mooring lines. It was evident from the observations that the shared mooring line significantly affects the surge and sway motions of the platforms. The increase in the mean and maximum horizontal offset of the FWTs is the result of a reduction in mooring restoring stiffness in the horizontal plane. Especially for the sway DOF, the increment is more obvious as only two mooring lines contribute to the

restoring force of both FWTs. For the second configuration with the aim of investigating the effect of varying distance between two FWTs, a similar effect in surge and sway DOF is observed. It was demonstrated that altering the length of the shared mooring line and distance between the FWTs has small effect on the responses of FWTs. This can be attributed to the negligible contribution of shared mooring line's tension to restoring force and moment.

4.2 Free decay test

Natural period, T_n , is the time required for a structure to complete one complete oscillation cycle. It is an intrinsic feature of a structure determined by the mass m and stiffness k of the structure and is measured in seconds (s).

$$T_n = 2\pi \sqrt{\frac{m}{k}} \tag{46}$$

Structures that are heavy (with large mass m) and flexible (with smaller stiffness k) have larger natural period than light and stiff structure.

All three models are subjected to decay testing in six distinct rigid body motions. In SIMA, this is modeled by raising the ramp force applied to the structure until the desired value is reached. After the ramp, a continuous force is provided to maintain the model's offset position and dampens out the oscillations caused by the impact of the applied force before removing the force and initiating the decay. Figure 4.1 illustrates a ramp and constant force as in Kvamen, (2020).

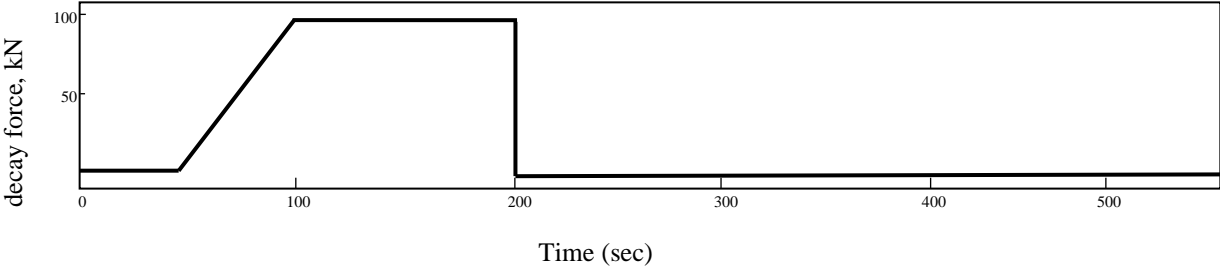


Figure 4.1 Decay force illustration with ramp duration 50 s, and constant force duration 100 s. Kvamen, (2020)

The simulation settings for the decay tests in the six rigid body movements included an application of a specified force for horizontal DOFs. A moment, rather than a force, is applied in the three revolutions of roll, pitch, and yaw. The duration differences are made to reduce

computational data because the natural frequencies in heave, roll, and pitch are smaller, and decay faster as described by Kvamen, (2020).

Table 4.1 lists the environmental conditions that are used for the decay test. They are constant during the free decay tests for all DOFs.

Table 4.1 Environmental simulation parameters for the decay tests.

| Item | Value |
|------------------------------|-------------------------------|
| Simulation time step in SIMA | 0.05 s |
| Time increment in SIMA | 0.1 s |
| Turbine condition | Parked |
| Wind input | 0.01 m/s |
| Wave conditions | $H_s = 0.001$ m, $T_p = 20$ s |

The time series of wind turbine positions are analyzed to derive the natural periods. A constant force with a certain ramp duration is applied to FWTs to reduce the initial impact perturbations. The force is applied for a period of time enough to ensure that the initial impact perturbation is dampened out and does not interfere with the natural period oscillation frequency. After that, FWTs are released and start oscillating around their initial position. These oscillations will decay at a constant rate depending on the structure's natural frequency. Now, we should be able to get the natural period of the structure by measuring any oscillation from crest to crest or from trough to trough.

Force is applied to the FWTs in different modes to capture the natural periods in different horizontal and rotational directions, as shown in Figure 4.2 and Figure 4.3. Twelve eigenmodes exist for the FOWF in the present study. Two eigenmodes are associated with each direction, e.g., “Surge 1” and “Surge 2”. The mode 1 in all six directions indicates that both CSCs move in the same direction as shown in Figure 4.2 (a) and Figure 4.3 (a). The mode 2 in all six directions indicates that both CSCs move in different directions as shown in Figure 4.2 (b) and Figure 4.3 (b).

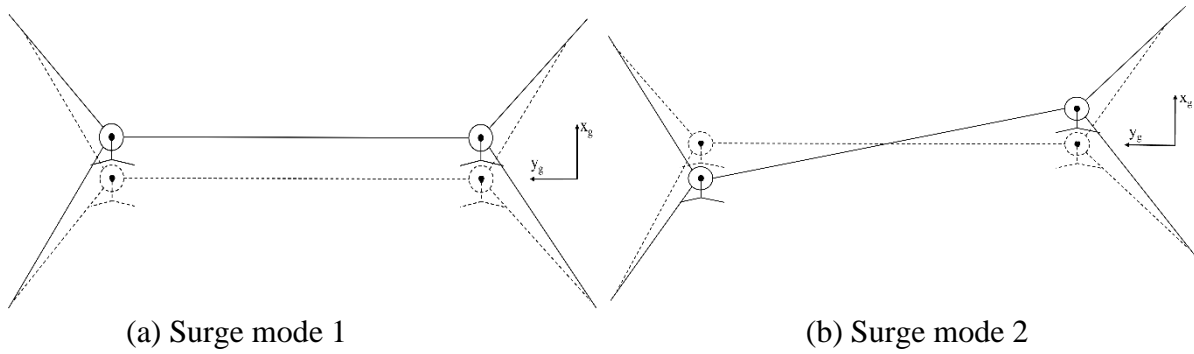


Figure 4.2 Illustration of eigenmodes in the surge direction (dashed line: initial position, solid line: mode shape)

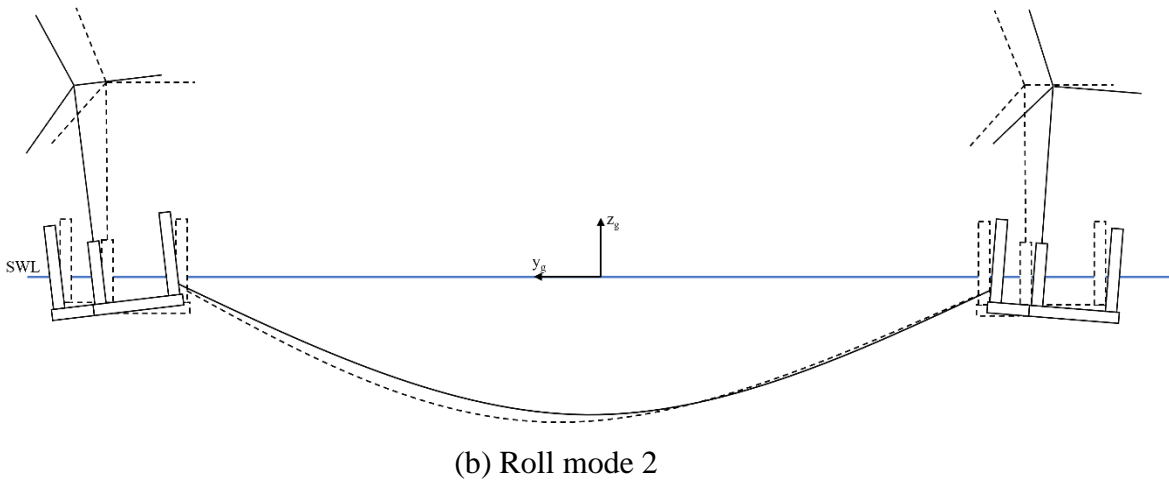
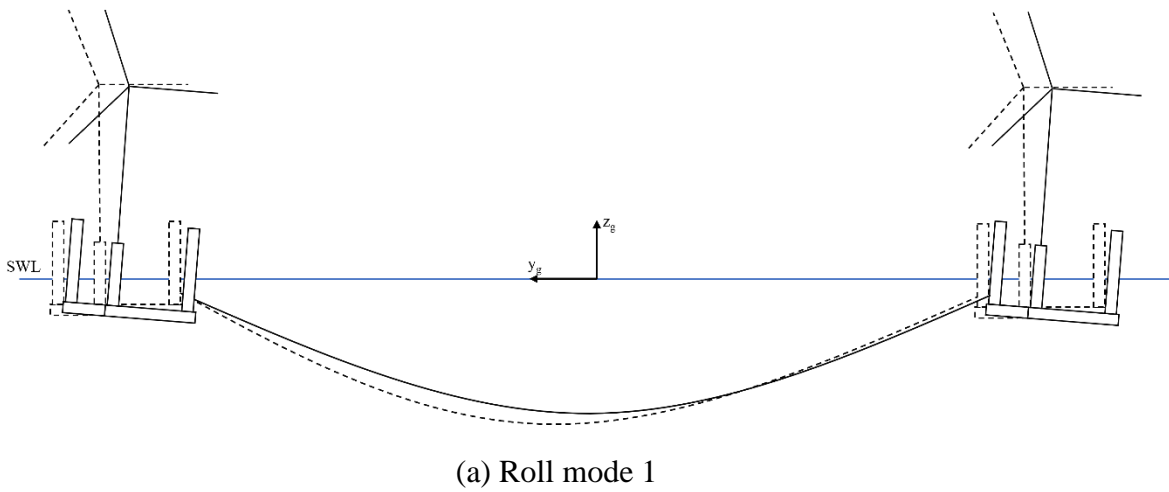


Figure 4.3 Illustration of eigenmodes in the roll direction (dashed line: initial position, solid line: mode shape)

Natural periods of a single CSC model from Luan et al. (2016) are listed in Table 4.2 for comparison.

Table 4.2 Natural periods [s] in six degrees of freedom of 5-MW single CSC model from Luan et al. (2016).

| Surge | Sway | Heave | Roll | Pitch | Yaw |
|-------|------|-------|-------|-------|-------|
| 79.5 | 79.5 | 25.8 | 31.28 | 31.32 | 58.12 |

The restoring stiffness change of the structure due to different mooring configuration greatly influence the natural periods of the semi-submersible structures in the horizontal plane (surge, sway, and yaw). Illustrations of some representative decay tests in the surge, sway, roll, and yaw degrees of freedom of Model 1 are plotted in Figure 4.4.

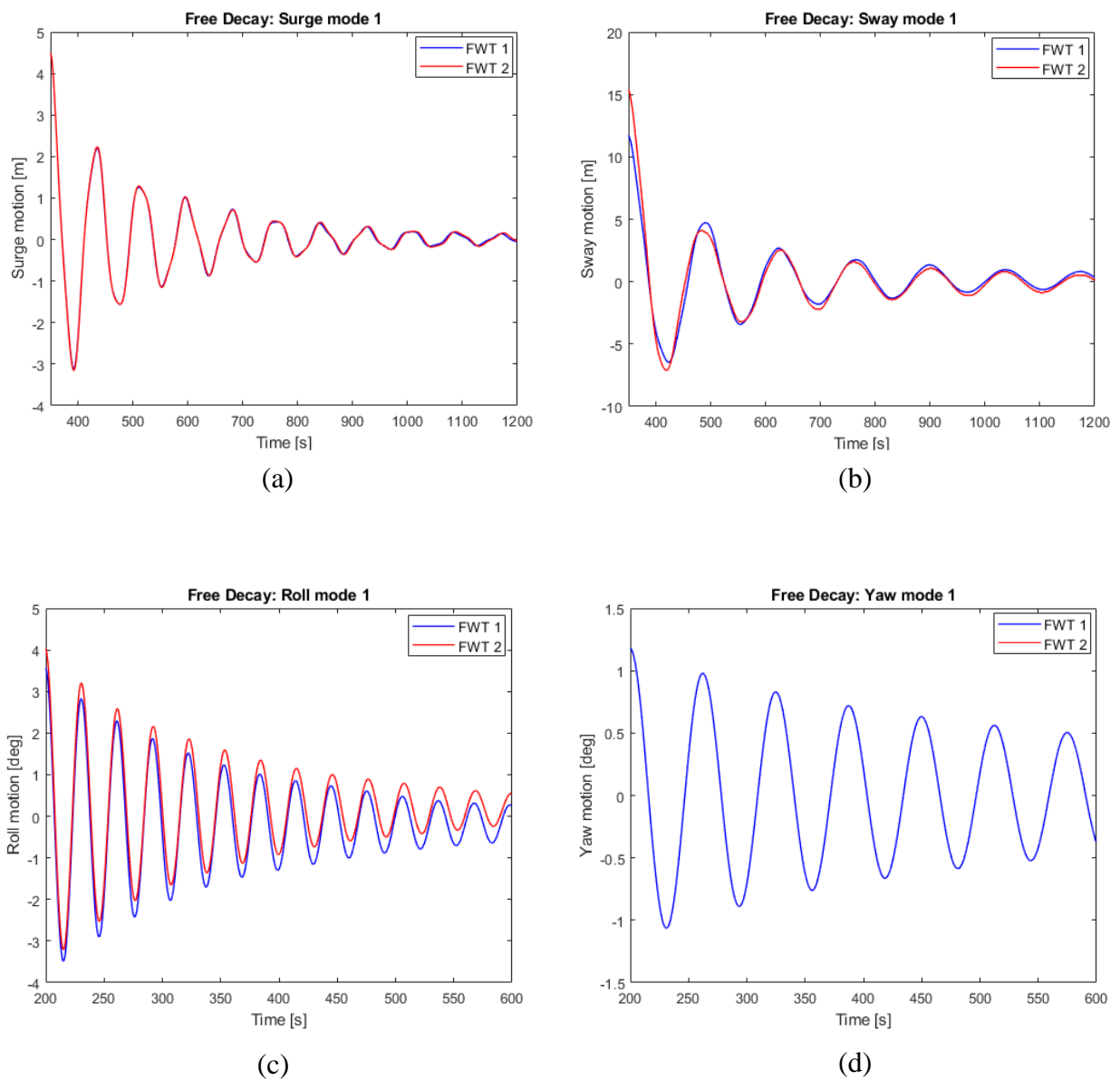


Figure 4.4 Free decay test for Model 1: (a) Surge; (b) Sway; (c) Roll; (d) Yaw

Natural periods for surge and sway DOFs are quite long. Figure 4.5, Figure 4.6, and Figure 4.7 summarize the findings of a free decay test conducted in calm water to compare the natural periods for the three models. As expected, the mooring mechanism has little effect on the natural periods in heave, roll, and pitch direction. The reference natural periods (surge, sway, and yaw) for Model 2 are larger than all the other models, including the single CSC. Whereas Model 1 has higher reference natural periods than Model 3 but less than Model 2, as seen from the following figures.

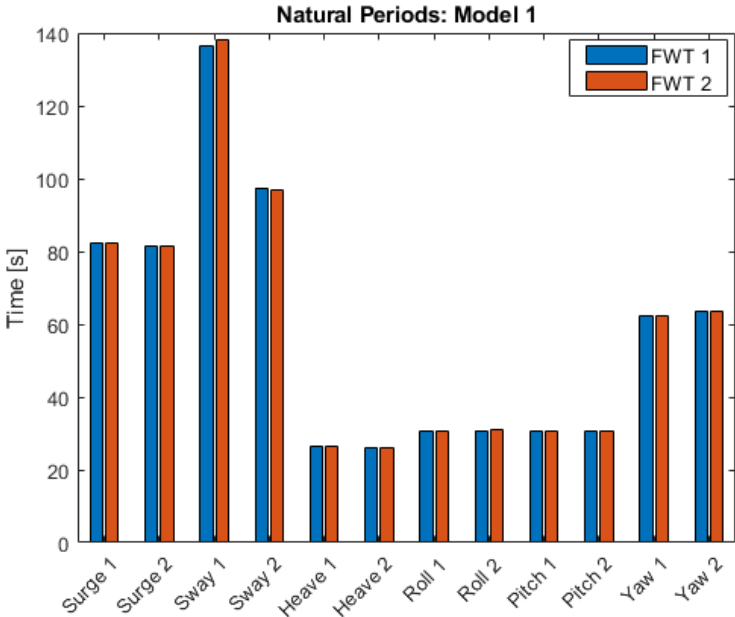


Figure 4.5 Free decay natural periods for the dual 5-MW CSC Model 1.

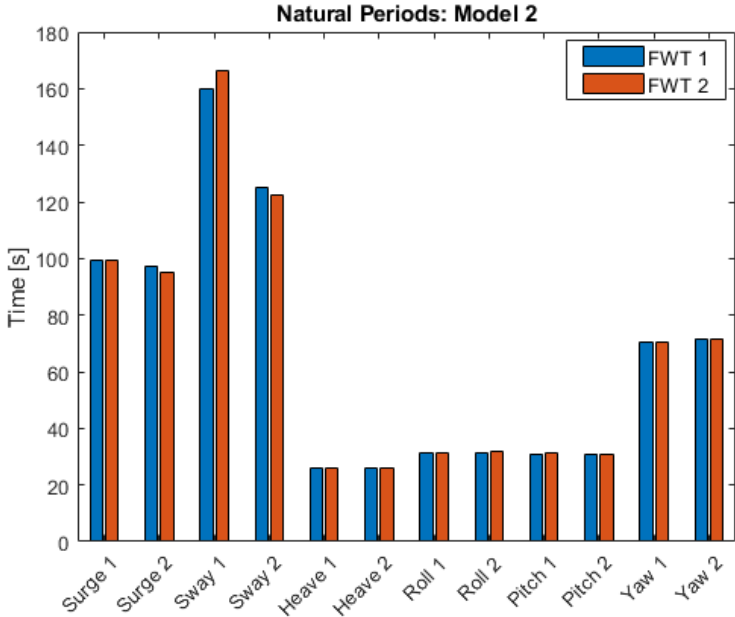


Figure 4.6 Free decay natural periods for the dual 5-MW CSC Model 2.

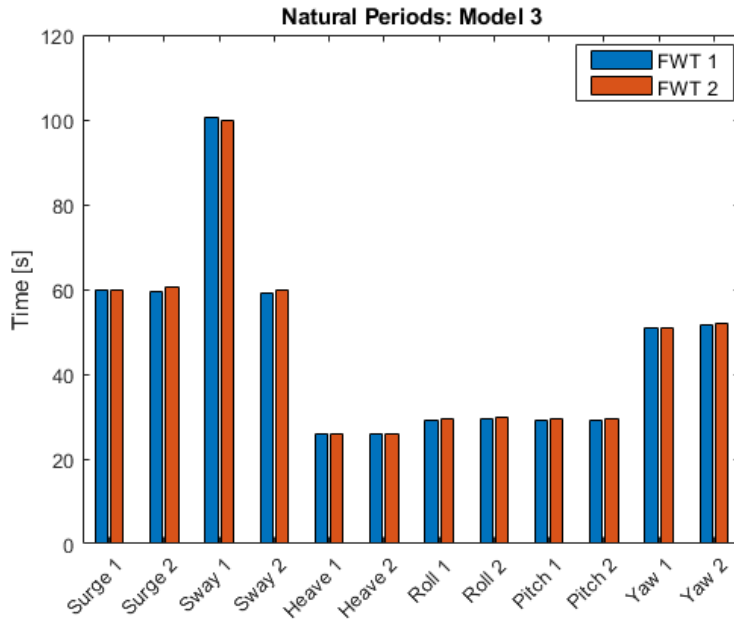


Figure 4.7 Free decay natural periods for the dual 5-MW CSC Model 3.

The difference in the natural periods for FWT 1 and FWT 2 of the dual CSC models is not significant. The FWTs with a shared mooring system have higher reference natural periods than a single CSC model. The higher reference natural periods can be attributed to the reduction of the structure's restoring stiffness by removing one anchored mooring line from each of the FWTs (see Equation 46). Also, different configurations of mooring lines concerning the change of anchor points lead to different restoring stiffness of the structure, which influences the natural periods as discussed in further sections.

For Model 2, higher natural periods occur due to a longer shared line, because of the increase in structure's mass and thereafter the periods. Also, the clump weights introduce more mass and geometrical stiffness, which further increases the periods. On the other hand, relative decrement in periods is observed for Model 3 with a shorter shared mooring line than the other two dual CSC models. Also, the geometry of the structure has less waterplane area, which introduces more considerable natural periods away from the wave periods, which is one of the reasons that semi-submersibles are good, especially in heave response.

4.3 Constant wind simulations

A constant incident wind input close to the rated wind speed of a 5-MW NREL wind turbine is used to simulate Model 1, Model 2, and Model 3 in an operational condition from directions 0

to 180 deg. Restoring stiffness of the system is calculated from the resultant thrust experienced by the FWTs and surge offset as a result of a constant wind input from 0 deg to 180 deg. The change in restoring stiffness of the structures can easily be captured through the present methodology. The same simulation technique is applied to a single CSC model for comparison purposes, and the results are plotted in Figure 4.8 and Figure 4.9. The input parameters of the simulation are given in Table 4.3.

Table 4.3 Simulation parameters for incident wind simulation.

| Item | Value |
|------------------------------|--------------------------------|
| Simulation length | 1500 s |
| Simulation time step in SIMA | 0.05 s |
| Time increment in SIMA | 0.1 s |
| Turbine condition | Operational |
| Constant wind input | 12 m/s |
| Wave conditions | $H_s = 0.001$ m, $T_p = 20$ s |
| Incident wind direction | 0-180 deg with 30 deg interval |

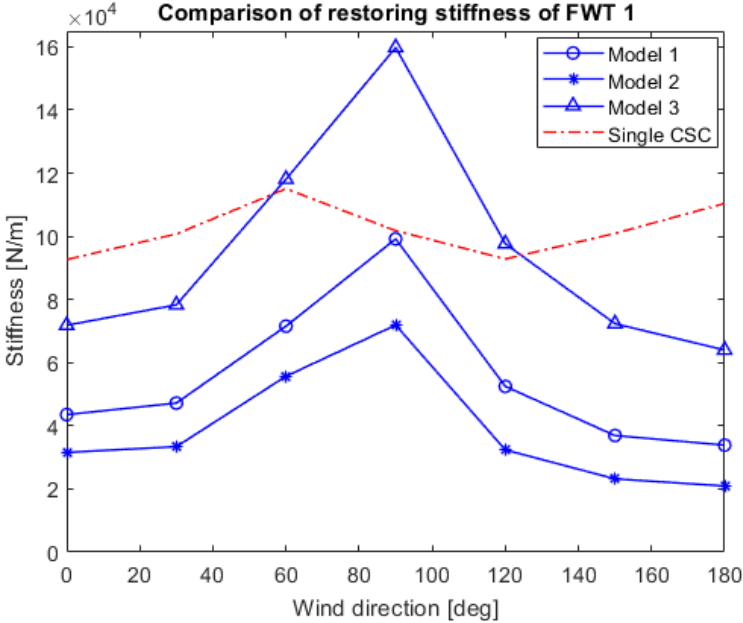


Figure 4.8 Stiffness comparison of FWT 1 from constant wind simulation.

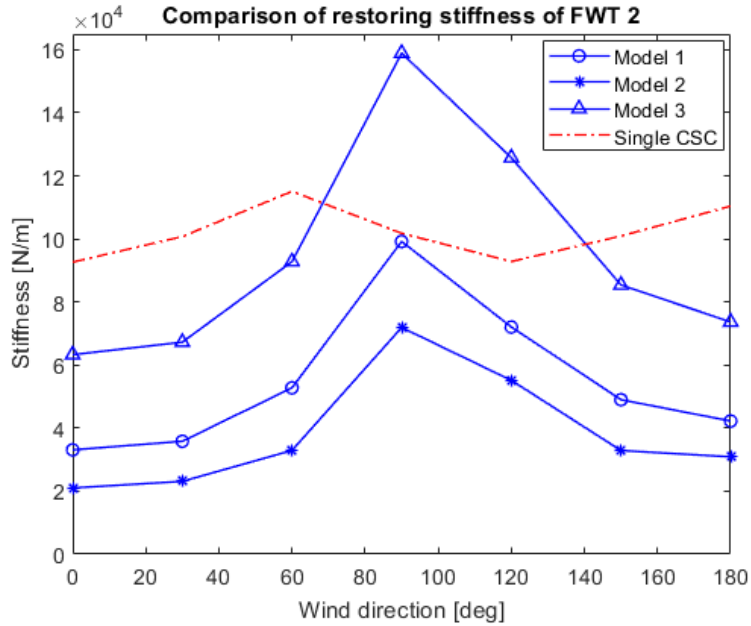


Figure 4.9 Stiffness comparison of FWT 2 from constant wind simulation.

As seen in Figure 4.8 and Figure 4.9, the mooring restoring stiffness of the system with a shared mooring line decreases as compared to a single CSC. The decrease in stiffness is due to reducing one anchor fixed mooring line from each of the FWTs and different mooring configurations for Model 1, Model 2, and Model 3. The higher decrement is observed for Model 2 with a longer shared line. As a result, Model 2 depicts higher offsets and natural periods due to increased mass with a longer shared line and different configurations of mooring lines. Detailed discussion about the system’s natural periods is done in previous Section 4.2, and the effects of system’s restoring stiffness change on dynamic responses and offsets are highlighted in further sections.

Model 1 with medium shared line length exhibits considerably better behavior than Model 2 and Model 3. The sagging distance of the shared line for Model 2 is very large and close to the seafloor. There might be a chance of a shared line touching the seafloor in extreme environmental conditions, leading to snap loads. This requires further investigation of the model’s response with higher U_w , H_s and T_p than the present study. After analyzing the responses in this work and taking into account the cost benefit analysis, Model 3 with a shorter shared line reveals smaller responses and provides cost savings options. But as this study is solely based on operational conditions, the shared line might experience tension loads due to its shorter length during extreme environmental conditions. As an example, Model 1 is chosen

to illustrate the behavior of FWTs as a result of reduced structure restoring stiffness and changed mooring configuration. The surge offset and pitch rotation of Model 1 in comparison with a single CSC are presented in Figure 4.10 and Figure 4.11 during constant wind simulation. The FWT 2 of Model 1 has a maximum offset of 17.4 m at the 0 deg incident wind. At the same place, FWT 1 has 13.2 m of offset compared to a single CSC model that is 6.2 m. The exact opposite responses of the FWTs can be observed at 180 deg due to the likewise configuration of the FWTs.

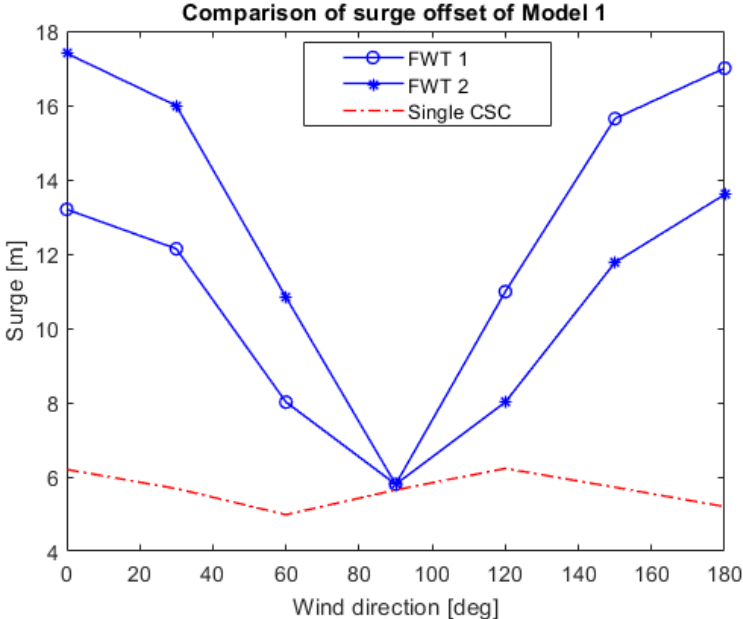


Figure 4.10 Illustration of horizontal offset of Model 1 from constant wind simulation.

Both FWTs have increased pitch motion compared to a single CSC model as shown in Figure 4.11. The maximum pitch of 5.7 deg is observed for FWT 1 at 180 deg. Whereas the FWT 2 has a maximum pitch of 5.62 deg at 0 deg incident wind direction. However, an interesting behavior is observed at 90 deg incident wind as both the FWTs have the same surge offset and pitch rotation. This is because the same system’s restoring stiffness occurs at 90 deg orientation of FWTs due to the same mooring lines configuration, as can be seen from Figure 4.8 and Figure 4.9.

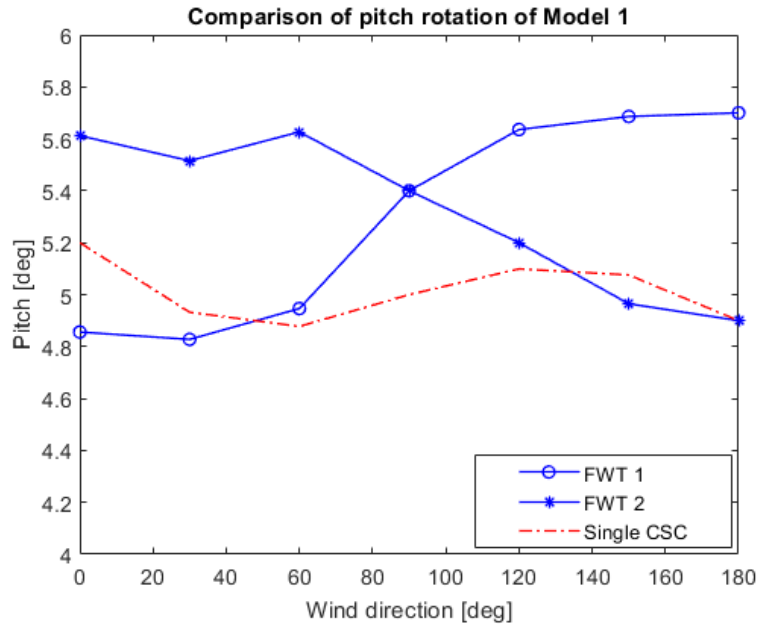


Figure 4.11 Illustration of pitch rotation of Model 1 from constant wind simulation.

4.4 Constant wind with varying wind speeds

A constant wind of varying magnitude is simulated on Model 1 in an operational condition. To capture the effects of varying wind speeds on mooring restoring stiffness, different wind speeds from 0 to 20 m/s with small intervals are applied to the structure. The same simulation setup as discussed in Section 4.3 is used to carry out the simulations, with the only difference being the varying wind speeds instead of constant wind speed. The input parameters of the simulation are listed in Table 4.3.

To see how the output properties changes for wind speeds under, at, and above the rated wind speed of 11.4 m/s, eight constant wind speeds are simulated within the operational limits of the wind turbines. Table 4.4 with the simulated wind speeds is presented below.

Table 4.4 Incident wind speeds simulated.

| Incident wind speeds [m/s] | | | | | | | |
|----------------------------|---|---|---|---|----|----|----|
| 0 | 3 | 5 | 7 | 9 | 12 | 15 | 20 |

The behavior of the FWTs when they are exposed to different wind speeds and the resulting thrust curve, is presented in the following figures.

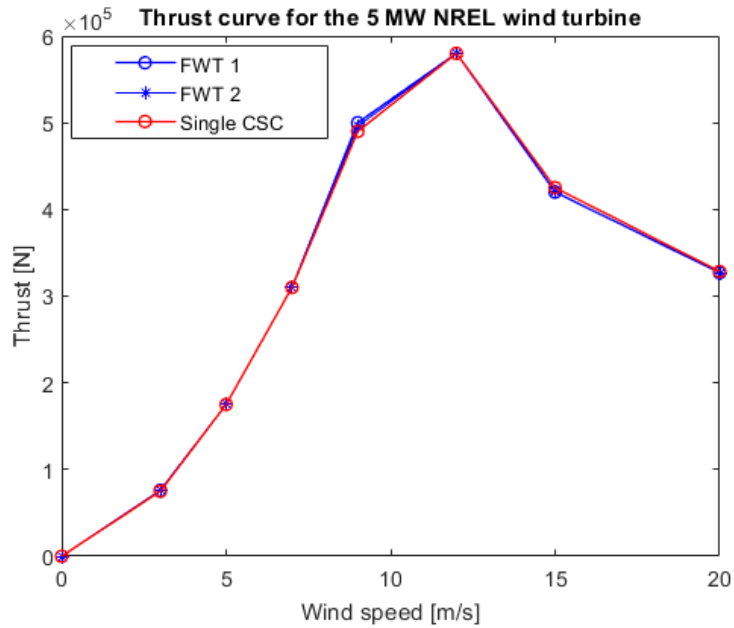


Figure 4.12 Thrust curve for the 5MW NREL FWTs from constant wind simulation.

The maximum thrust force of 580 kN is measured at a wind speed of 12 m/s, close to the rated wind speed of the wind turbine equal to 11.4 m/s. To illustrate how the thrust force affects the supporting substructure, Figure 4.13, Figure 4.14, and Figure 4.15 show the resulting platform translations in meters for wind directions of 0 deg, 90 deg, and 180 deg, respectively.

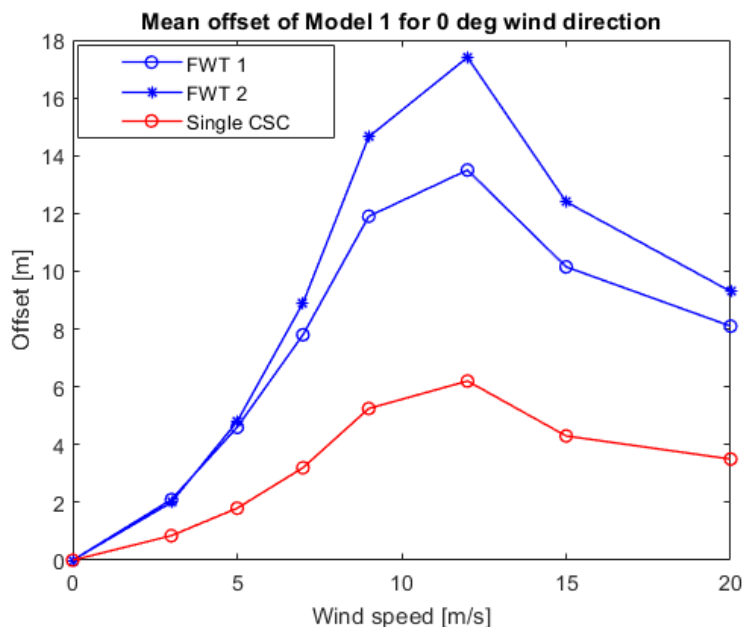


Figure 4.13 Platforms surge from incident wind simulation for 0 deg wind direction.

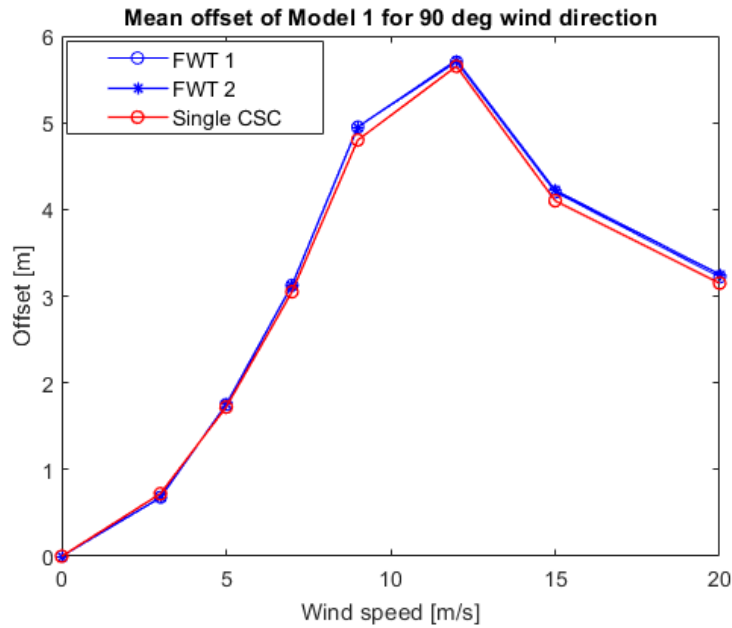


Figure 4.14 Platforms surge from incident wind simulation for 90 deg wind direction.

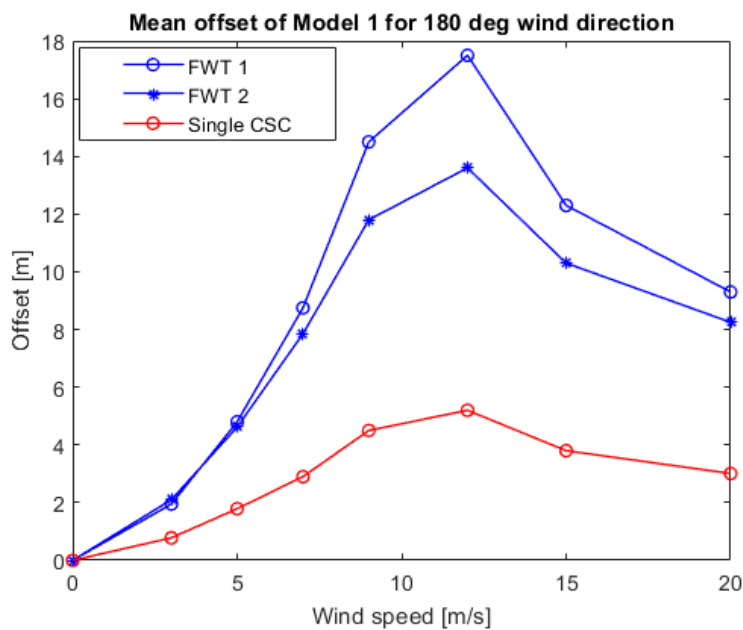


Figure 4.15 Platforms surge from incident wind simulation for 180 deg wind direction.

From the above figures, we can see that the surge motion of the platforms in both the Model 1 and single CSC model follows the thrust curve and gets a maximum offset of 17.5 m in the case of Model 1 compared to the single CSC model, which is 6.2 m at 12 m/s. This is because of the reduction of the restoring stiffness of the structure in different wind directions due to different mooring lines configuration, as shown in Figure 4.8 and Figure 4.9. However, the behavior of

both the models is the same in the case of 90 deg wind direction. This happens, because of the likewise configuration of single mooring lines in each of the models. The resultant offsets in the surge direction are only due to the thrust force generated by the wind because the environmental forces were simulated to approach the model in a surge direction, and the simulation input is a relatively smaller wave height of 0.001m.

By analyzing the incident wind simulations in various wind directions, some intriguing wind turbine behavior was identified. Due to the approach angle of the simulated wind parallel to the rotor plane, the thrust force influenced the surge and pitch motions. The structure's restoring stiffness decreases when wind speed and direction change. Moreover, the dual CSC model's mooring restoring stiffness decreases when one mooring line from each FWT is removed, which causes additional offset. The arrangement of the single mooring lines is also crucial in regulating the motion of the FWTs. With 0 deg wind, the offset of FWT 2 is more than the FWT 1. This can be attributed to the flexible connection of FWT 2 with a shared line rather than the FWT 1 which is moored with two anchor fixed single lines, and vice versa.

4.4.1 Environmental conditions

Extreme operating conditions are taken into account for all models in this study. To simulate the dynamic response of all floating structures, a set of environmental conditions, the same as that of Luan et al. (2016), is selected for all three models. Li et al. (2015) describes a joint probability density function for mean wind speed U_w , significant wave height (H_s), and the peak period of the wave spectrum (T_p), as well as a three-dimensional contour surface for U_w , H_s , and T_p corresponding to the 50-year return period for European offshore site 14 (Norway 5). With a selection of three wind turbine operational wind speeds, the corresponding H_s and T_p are selected as their conditional means based on the joint distribution. To characterize the irregular wave condition, the JONSWAP spectrum with significant wave height H_s and peak period T_p is utilized given in Equation 47. The corresponding wind is kept constant in all directions around the floating structures to account for the effect of changed mooring restoring stiffness.

$$S_J(\omega) = F_n \cdot S_{PM}(f) \cdot \gamma \exp\left[-\frac{(f-f_p)^2}{2\sigma^2 f_p^2}\right] \quad (47)$$

where $S_{PM}(f) = 0.3125H_s^2 T_p^{-4} f^{-5} \exp\{-1.25T_p^{-4} f^{-4}\}$

$$F_n = [5(0.065\gamma^{0.803} + 0.135)]^{-1}$$

$$\sigma = \begin{cases} 0.07 & f \leq f_p \\ 0.09 & f > f_p \end{cases}$$

F is the fetch, f is the wave frequency, f_p is the peak frequency, and γ is the peak enhancement factor typically 3.3 for North-Sea.

To address the 5-MW-CSC's motions in severe combined wind and wave conditions, three mean wind speeds (EC1 to EC3) are selected and reported in Table 4.5. They include a wind speed below the rated speed, a wind speed at the rated speed, and a wind speed over the rated speed. The mean wind speeds in the table are relative to the nacelle's position, i.e., the wind speed U_w at a reference height of 90 m is considered between cut-in and cut-out.

Three sets of independent 4600-second simulations with six random seeds are run for each loading condition in all floating CSC models to describe the constant wind and irregular wave conditions. The mean values are obtained from the time-series data to depict the stochastic variations. To avoid the transient effects, first 1000 s have been avoided and 4600 s simulation then can approximate a one-hour length.

Table 4.5 Environmental loading for extreme operating condition from Li et al. (2015).

| Load case | U_w [m/s] | H_s [m] | T_p [s] | Note |
|-----------|-------------|-----------|-----------|-------------|
| EC1 | 9.8 | 7.5 | 14.7 | Operational |
| EC2 | 11.4 | 7.9 | 14.4 | Operational |
| EC3 | 16 | 9.14 | 15 | Operational |

Note:

The wind speed is the mean wind speed at the reference height of 90 m above SWL.

4.4.2 Mooring lines tension

All models in this study are moored using the catenary mooring lines. The mooring system's primary function is to keep the floater at its mean equilibrium position under various environmental conditions. The tension of the mooring lines is measured at the fairlead point and is the sum of the tension in the line and the clump mass. A sensitivity study is performed for the maximum offset limit of the floating platforms. The single and shared lines' properties are taken from Luan et al. (2016) and listed in Section 3.2.1.1 and Section 3.2.3.1.

The offset of CSCs and the tension in each line are examined in the x_g and y_g directions as shown in Figure 3.5 and Figure 3.6. The tension in the four catenary moorings increases linearly when the x and y offsets are increased, whereas the influence of the clump weight is negligible. The tension increases linearly at small x-offsets and becomes nonlinear at large offsets for the four catenary moorings, that's why a range of -20 m to 20 m is chosen for the offset limit of floating platforms in the plots. Comparative results of the dual CSC system and a single CSC are shown in Figure 4.16 and Figure 4.17.

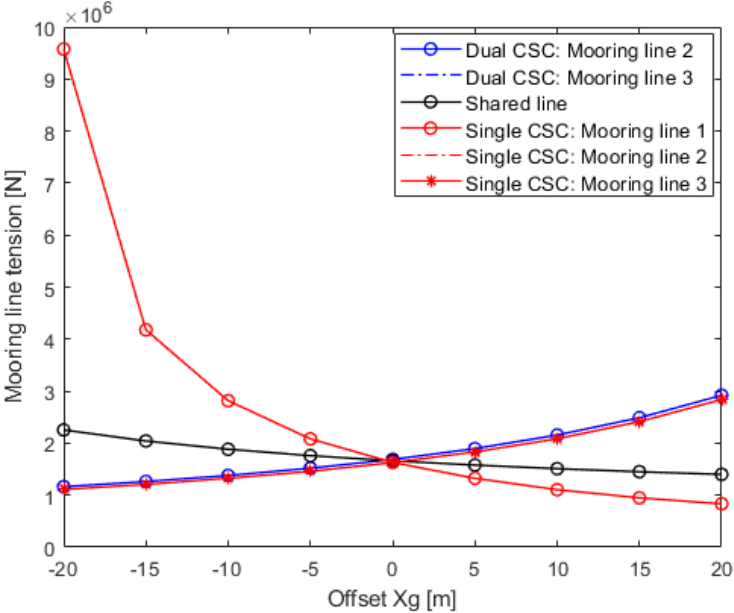


Figure 4.16 Relationship between line tension and offset x_g .

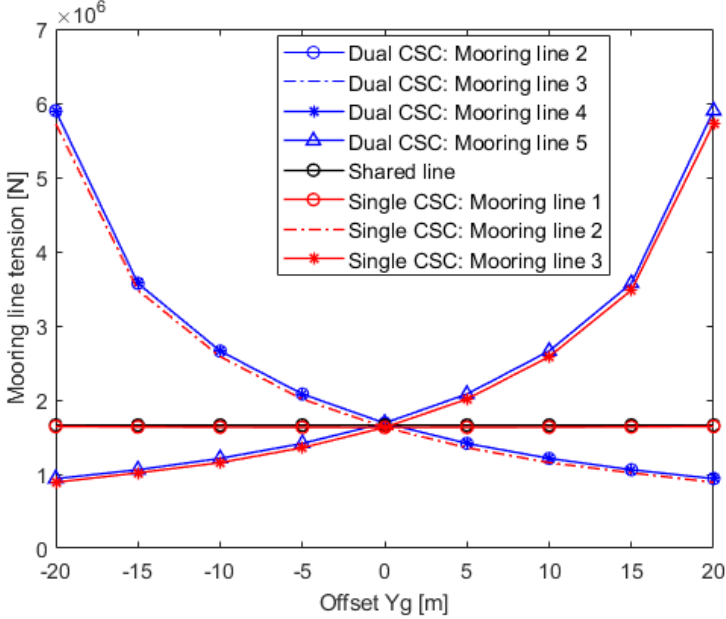


Figure 4.17 Relationship between line tension and offset y_g .

The tension in mooring line 2 and mooring line 3 in Figure 4.16 is symmetrical to the tension in mooring line 4 and mooring line 5 because of the symmetry of the structural arrangement of dual CSC models about the x_g -axis. Due to this, Figure 4.16 shows just the findings of mooring line 2 and mooring line 3. It is noticed that the maximum tension is achieved by the single mooring lines in Figure 4.17. While in Figure 4.16, maximum tension is found in the mooring line 1 of the single CSC model and shared line for the dual CSC model. Even though the maximum breaking load (MBL) of the mooring lines is not given by Luan et al. (2016), the tension in the shared line for the value of $y_g = -20$ m should be close to the MBL. Tension in the shared line increases linearly and gets tightened, especially when CSC moves in the negative direction of x_g -axis. For large negative offset x_g , the tension in the shared line exceeds the MBLs. At the further offset, the tension in the shared line even exceeds the tension in the single mooring line 1 of the single CSC model and comes under tension.

The total mooring restoring forces acting on the FWTs can be calculated using the current modeling approach since the tension in each line can be calculated. Tension on each fairlead calculates the total mooring restoring forces on FWTs. The relationship between the total mooring restoring force acting on the FWTs and the horizontal offset along the y_g -axis is investigated. The dual CSC system is compared to the single CSC model. The relationship between the horizontal offset of FWTs and mooring restoring force is shown in Figure 4.18. It will give an overview of the average horizontal motions when subjected to normal environmental loads.

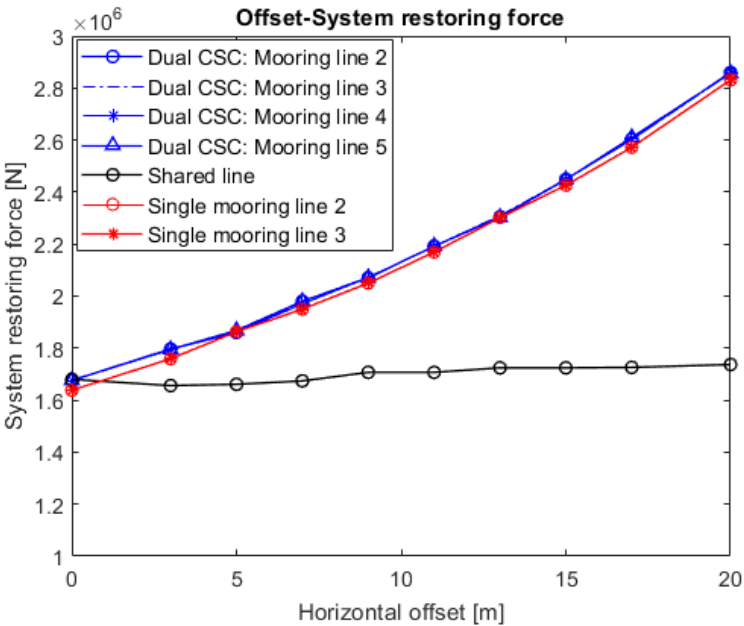


Figure 4.18 System restoring force.

From Figure 4.18, it can be seen that the mooring restoring effect of the shared line is not significant in the horizontal direction, especially in the surge direction. The difference in mooring restoring force is not substantial for distinct properties of the shared line. This is reasonable since the tension in the shared line is less than in the single mooring lines, as illustrated in Figure 4.16 and Figure 4.17. Additionally, the surge direction is almost perpendicular to the shared line's catenary plane, implying that the tension in the shared line contributes far less than the tension in the other two single mooring lines in the surge direction. Hence, it is evident that the FWTs with a shared mooring system change the system's restoring effects compared to the single CSC model.

4.4.3 Platform motions

Typically, platform motion is classified into six degrees of freedom: surge, sway, heave, roll, pitch, and yaw. The heave is described in global coordinates with the z_g axis parallel to the CSC's axial direction as shown in Figure 3.14, while the surge is defined on the x_g axis parallel to the wind directions.

Three different configurations of the dual CSC model i.e., Model 1, Model 2, and Model 3 are considered with different mooring configurations, as listed in Table 3.9. The resulting responses are compared against the single wind turbine system proposed by Luan et al. (2016) and discussed further. The responses of a single CSC model from Luan et al. (2016) against the environmental conditions listed in Table 4.5 are tabulated in Table 4.6. The simulation setup for the rigid body motions is described in Section 4.4.1, which is the same for all the cases. The direction of incident wind is directed at 90 deg, which is directed directly into the hub of rotor plane, while four different wave directions are considered (from 0 to 90 deg with 30 deg intervals) in the time domain simulations. Extreme loads can be well estimated by aligned wind and wave situations as described by Barj et al. (2014). However, tower-base side-to-side bending moments depend strongly on the perpendicular wind and wave cases. This bending moment is induced by the roll motion of floating platforms. Especially for 90 deg misalignment of wind and waves, tower-base side-to-side bending moment is maximum because of the maximum roll motion of the platforms. Only including aligned wind and waves results in a 50% miscalculation of the tower-base side-to-side bending moment and a 5% overvaluation of the tower-base fore-aft bending moment calculated by Barj et al. (2014). These values are essential

for fatigue calculation in the future and must be accounted for. The tower-base side-to-side bending moment for FWT 1 is presented below.

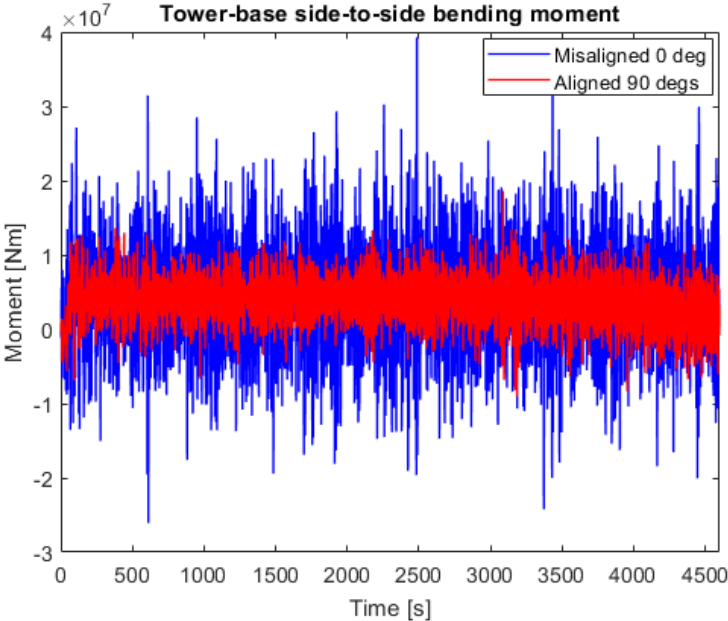


Figure 4.19 Tower-base side-to-side bending moment of FWT 1’s tower.

The above figure shows that the tower experiences high bending moment when wind and waves are misaligned, with the wind coming from 0 deg and waves from 90 deg. On the other hand, there is around a 50% decrease in values and standard deviation when wind and waves are aligned at 90 deg. Based on these results, the misaligned wind and waves study must be carried out as done in the present study to represent a CSC platform's extreme and fatigue characteristics accurately.

Table 4.6 Statistical properties of a single CSC model presented by Luan et al. (2016).

| ECs | Statistical Properties | Surge [m] | Sway [m] | Heave [m] | Roll [deg] | Pitch [deg] | Yaw [deg] |
|-----|------------------------|-----------|----------|-----------|------------|-------------|-----------|
| EC1 | Max | 10.4 | 3.8 | 2.3 | 1.9 | 9.1 | 1.8 |
| | Mean | 5.9 | 0 | 0 | 0.3 | 5.8 | 0 |
| EC2 | Max | 11 | 3.9 | 2.5 | 2.1 | 10.1 | 1.9 |
| | Mean | 6.5 | 0 | 0 | 0.4 | 6 | 0 |
| EC3 | Max | 8.7 | 4.1 | 3.1 | 2.5 | 9.1 | 2 |
| | Mean | 4.1 | 0 | 0 | 0.6 | 4 | 0 |

To account for the statistical uncertainties, six random wave seeds are used for different wave realizations and their average statistical properties are calculated. The surge and sway motions are significantly influenced as compared to the other DOFs by the shared mooring configuration as described by the free decay tests in Section 4.2. Also, the natural periods in roll and pitch DOFs do not change much as compared to the single CSC model. It proves that the mooring system has a minor impact on these DOFs. In this section, the motions of the supporting platform in the surge, sway, and pitch DOFs are studied. The maximum and mean values of the platform surge, sway and pitch motions for Model 1, Model 2, and Model 3 are shown in Figure 4.20, Figure 4.21, and Figure 4.22, respectively.

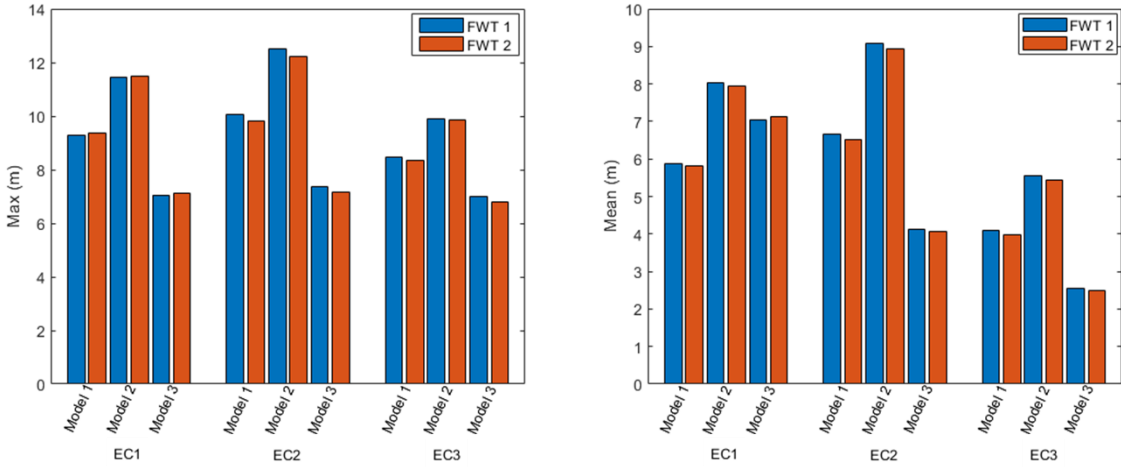


Figure 4.20 Platform surge

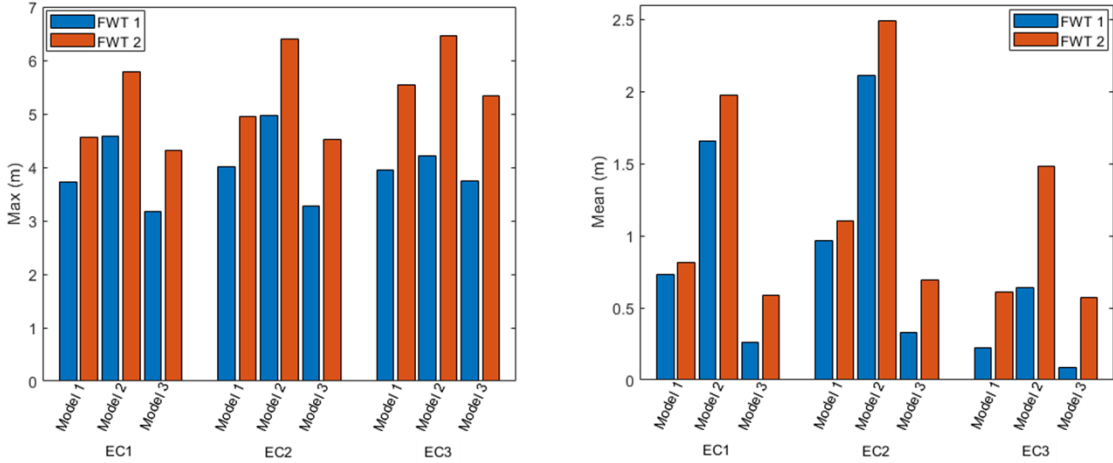


Figure 4.21 Platform sway

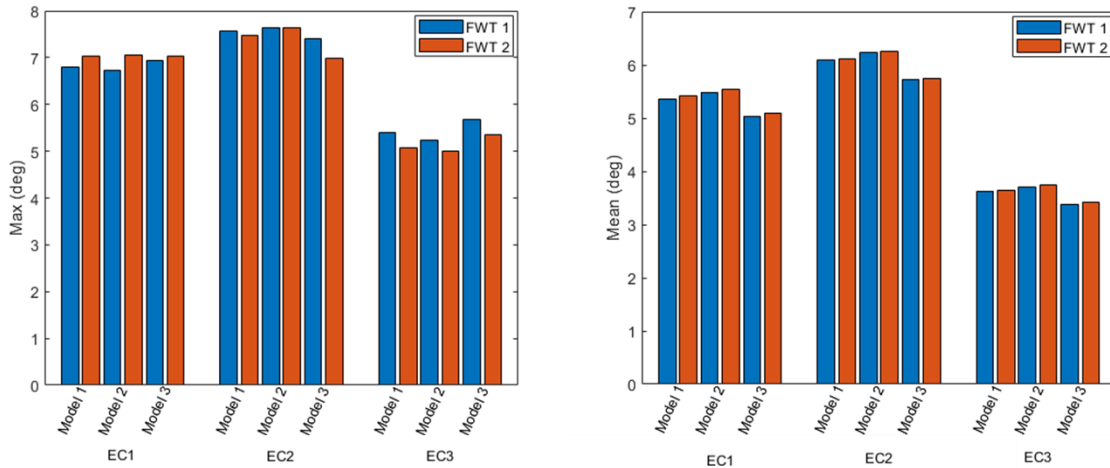


Figure 4.22 Platform pitch

A significant increase in motion is observed for Model 2 with a longer shared line. The reduced restoring stiffness of the system leads to higher offsets, as discussed in Section 4.3. The maximum surge offset of Model 2 is 12.5 m in EC2, which is 14% more than the single CSC and 25% more than Model 1. A similar trend is observed for the mean surge offset of Model 2. The relative difference in surge motion between the two FWTs' is less than 2% in all models. This happens because, during 90 deg angle of wave propagation, both FWTs experience the same restoring forces in surge direction due to the same mooring orientation. The alignment of wind and wave directions at 90 deg results in further higher offsets in the surge direction.

Moreover, the FWTs experience the same wind thrust force during the respective environmental loads. In SIMA, the simulation code is modeled with the possibility of one wind file for all the FWTs. This means that both FWTs will be exposed to the same wind realizations and will not be independent. Especially for our case, where the FWTs are at least 1128.6 m apart, this is not realistic, as normally they would experience different wind speeds and gusts resulting also in uneven loading of the mooring arrangement. With the current simulation tool configuration, this uneven load effect cannot be captured.

On the other hand, the shared mooring configuration also leads to higher sway offsets as can be seen from Figure 4.21. Model 2 experiences significantly higher maximum and mean sway offset than the single CSC model and Model 1 in EC2. By changing the mooring configuration and increasing the shared line's length by 2.4%, the maximum sway displacement of Model 2 increases up to 18% and 58% compared to the Model 1 and the single CSC model, respectively.

The mean sway offset also increases and reaches the maximum of 2.4 m, compared to 0 m in a single CSC case and 1.1 m for Model 1. The maximum sway motion occurs at 0 deg incident wind direction for FWTs. There is a significant relative difference among the FWTs' sway motion with FWT 2 experiencing 25% higher offset than FWT 1. This can be attributed to the fact that, while the two FWTs are pushed towards y_g -direction, the restoring force is generated by the two anchored catenaries attached to the upwind FWT. While both FWTs are traveling downwind, the restoring force ending up in the downwind FWT is reduced since it got consumed in reducing the sag of the shared line. We could say that there is a lagging in experiencing the restoring force between the two FWTs. The lagging is actually the storage of potential energy to reduce the sagging of the shared mooring line. This lagging enables the downwind FWT to gain some momentum. The combination of the reduced restoring force and viscous drag of the sagging on its way to regain its original position results in a higher offset of FWT 2.

The sagging distance of the shared line is more considerable for Model 2 due to its longer length than the Model 1 and Model 3. For the maximum sway offset of FWTs, the shared line is still 11 m above the seafloor in case of Model 2. So, there is no interference of reduced tension and snap loads with the responses of FWTs. In the present work, the mooring system and configuration of FWTs are modeled in such a way that the mooring system has higher stiffness in sway direction than surge. Due to this configuration, FWTs show more offset in the surge direction and less in the sway direction.

The heave, pitch, roll, and yaw DOFs are not much affected by the mooring configuration in the present study. The resultant motions are within the range of a single CSC model. Heave motion is independent of wind and waves' direction. The FWTs in dual CSC configurations have represented minimal heave motions for all the ECs. The FWTs with varying shared line lengths and mooring configurations are modeled so that these DOFs are not much affected. Also, the wind force impact is constant because of the defined wind properties. This influence the surge and sway DOFs more and have less effect on rotational DOFs, i.e., pitch and roll.

The power spectral density chart of Model 2 for surge, sway, and pitch DOF is plotted in Figure 4.23, Figure 4.24, and Figure 4.25. It is evident from the figures that the surge, sway, and pitch motions are waves-dominated. However, no resonance is observed due to the large natural

periods of FWTs which are far from the wave periods. The mean wind speed is constant which is why we cannot observe any low frequency response from power spectral charts. The surge offset of FWT 1 is slightly higher than FWT 2. This is caused by different excitation forces experienced by the FWTs. Because of the surge-pitch coupling, the difference among the pitch resonant response of FWTs also leads to the relative difference in surge motion of FWT 1 and FWT 2. Furthermore, a slight reduction of pitch response for Model 1 and Model 3 is observed as compared to Model 2.

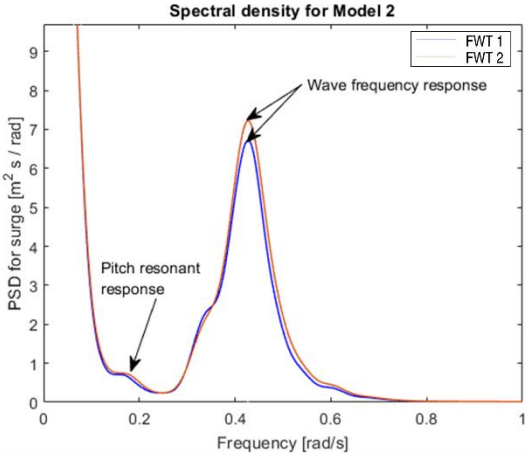


Figure 4.23 Power spectra for platform surge in EC2.

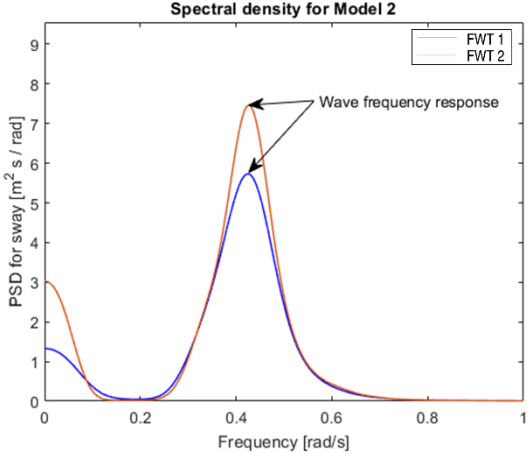


Figure 4.24 Power spectra for platform sway in EC2.

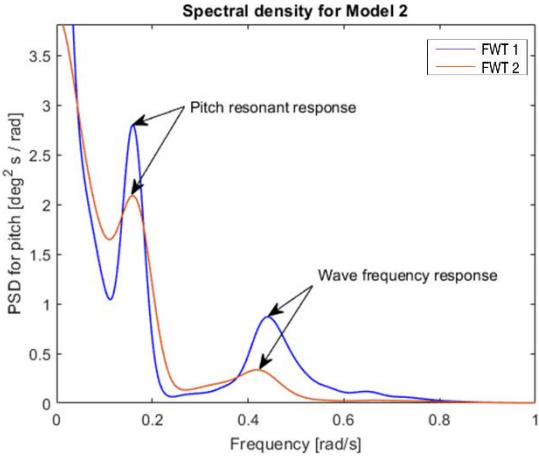


Figure 4.25 Power spectra for platform pitch in EC2.

5 CONCLUSION

The dual CSC-5MW FWTs with three different configurations of shared mooring lines are modeled in this thesis. The length of a shared mooring line is varied without changing the static equilibrium position of the two FWTs. The initial distance between the FWTs is adjusted to accommodate the varying lengths of a shared line that makes up the three different models, as Model 1 with medium long shared line, Model 2 with a longer, and Model 3 with relatively shorter shared line. The results proposed that the shared mooring line is a feasible concept with added dynamic complexity. Several main conclusions from this study are given below.

- The FWTs are modeled by connecting two single CSC models horizontally. One mooring line is removed from each FWTs and connected them with a shared line with different lengths that make up three different configurations of FWTs. The horizontal distance between the FWTs is kept constant at 9 rotors diameter distance of approximately 1128.6 m. To accommodate the varying lengths of a shared line in each configuration, the platforms are rotated, and anchor points are adjusted to keep the FWTs at their mean static position. The FWTs are rotated by 90 deg and always face the upwind direction. Taking the benefit from the possibility of rotating the FWTs in SIMA, the dynamic behavior is captured as a result of constant wind simulations from 0 deg to 180 deg wind directions.
- The free decay tests are performed initially on all the configurations of a dual CSC and compared against the single CSC model. A dual CSC FWTs' surge, sway, and yaw DOFs are significantly influenced by the shared line. The natural periods of the surge, sway, and yaw DOFs are highly sensitive to both shared and single lines' configurations. Due to the reduced mooring restoring stiffness, the dual CSC system has increased reference (surge, sway, and yaw) natural periods than the single CSC model. Model 2 have relatively higher natural periods than the other two dual CSC models because of the increased mass of the system due to a longer shared line. Similarly, the Model 3 with a shorter shared line has small natural periods than the other two dual CSC models. It is essential to pay close attention to the surge and sway degrees of freedom in the design of a shared mooring system to avoid resonance.

- The effect of wind loads on FWTs is studied. The maximum thrust experienced by the FWTs is at 12 m/s which is close to the rated wind speed of 5-MW NREL wind turbine. Constant wind and wind with varying magnitude from different directions of FWTs are applied on the dual CSC and a single CSC FWT, and the resultant structures' restoring stiffnesses are compared. The results show a considerable decrease in the structure's restoring stiffness for the dual CSC system. This decrease can be attributed to the reduction of one anchor fixed mooring line from each of the FWTs. Also, the different mooring configurations affect the mooring restoring stiffness and lead to higher maximum offsets than the single CSC model. FWTs exhibit similar behavior for 90 deg incident wind because of the same mooring configuration and restoring stiffness of the structure as compared to a single CSC.
- Basic catenary equations are used to design the shared mooring line. Most of the properties of a shared line are kept the same as a single mooring line to make a good comparison. A mooring lines' tension study is performed to examine the influence of a shared line on the restoring effects of the moorings. The configuration of a single CSC has been used for comparison. It is evident that the mooring restoring effect of the dual CSC system is influenced significantly in surge and sway DOFs. In addition, the mooring restoring force investigation demonstrated that a shared line's restoring force in the horizontal direction is almost negligible. This proves that the shared line is not participating in restoring the motions in horizontal DOFs.
- Global time-domain analysis has been carried out to calculate the global responses in six DOFs in three selected combined wind and wave conditions. All the three models with different shared line lengths were exposed to environmental loads, and the responses were compared against the single CSC model. It was observed that the shared mooring system results in higher surge and sway displacements due to the reduction of mooring restoring stiffness of the structures associated with the change in platform orientation and mooring configuration. Model 2 with long shared line results in higher motions than the other two models and vice versa. The reduction of one anchored mooring line from each of the FWTs in dual CSC models and shared mooring lines' negligible participation in restoring the surge and sway displacements can also be attributed to the higher maximum and mean offsets of dual CSC systems in surge and sway DOFs. During the global analysis of Model

2, it was found that the sagging distance of the shared line has increased and kept the sag at 11 m above the seafloor during the maximum sway offset. There is a possibility for a shared line to touch the seafloor in extreme environmental conditions with higher H_s and T_p . As in our case, the waves dominate the surge and sway motions; this could lead to the snap loads on fairleads. Similarly, the shared line also gets tightened during the extreme environmental conditions for Model 3 because of its shorter length and can experience increased tension loads. Keeping all this in mind, Model 1 with a medium shared line length is recommended for further investigations in the future.

The present modeling and analyzing methodology can be utilized in the preliminary design of FOWFs with shared mooring lines.

6 RECOMMENDATIONS FOR FUTURE WORK

The current research intends to develop a model for early exploration of the dynamic behavior of two FWTs connected by a shared mooring line. Modifications and enhancements to the findings obtained in this work can be implemented in the future. However, a more robust dual CSC model with a shared line can be expected to develop and be investigated in the future. Several ideas to make the current model better and more comprehensive are proposed in the following.

- To begin, updated metocean data from the area of interest may be analyzed, as environmental conditions may have changed in recent years. New environmental conditions could be developed and analyzed for dynamic responses.
- This research work did not investigate the effects of current. As a result, the systems would have bigger offsets and mooring line tensions, which should be examined before running additional simulations.
- As discussed in Section 4.4.3, SIMA has a limitation of only one wind file for multiple FWTs. This means that the FWTs will experience the same wind realizations during the simulations, which is not realistic, especially when the FWTs are placed at large offsets. In reality, they would experience different wind speeds and gusts, resulting in uneven loadings. To account for this, “OpenModelica” is an open-source Modelica simulation environment that can be used with different wind properties for multiple FWTs.
- When it comes to deploying ocean energy, a combination of concepts seems to be the most effective method to save money and boost output. An integrated offshore renewable energy concept by Luan et al. (2014), which incorporates three flap-type wave energy converters, could increase the power production by deploying on the dual CSC model with a shared line. This could also increase the dynamic complexity and induce increased motions to the platform, which is another interesting topic and could be considered for further studies.

- It is possible to do a fatigue analysis of the system if sufficient turbulent wind simulations are conducted. In some cases, identifying the most damaging combinations of wind speed U_w , significant wave height H_s , and wave period T_p might help prevent system failure.
- Cost should also be studied to determine how much total cost is saved by sharing a mooring line between the FWTs, including the cost of anchors and the single lines. The overall cost might be further reduced by investigating the use of shared mooring lines amongst three or more FWTs. The length and expense of the power cable may be decreased if it could be built similarly to the shared mooring line in this project, rather than laying on the seabed.

7 REFERENCES

- [1]. Council, G.W.E., Global Wind Report 2021. 2021. *Global Wind Energy Council: Brussels, Belgium*.
- [2]. Munir, H., Lee, C.F. and Ong, M.C., 2021, November. Global analysis of floating offshore wind turbines with shared mooring system. In *IOP Conference Series: Materials Science and Engineering* (Vol. 1201, No. 1, p. 012024). IOP Publishing.
- [3]. Musial, W., Butterfield, S. and Boone, A., 2004, January. Feasibility of floating platform systems for wind turbines. In *42nd AIAA aerospace sciences meeting and exhibit* (p. 1007).
- [4]. Fontana, C.M., Arwade, S.R., DeGroot, D.J., Myers, A.T., Landon, M. and Aubeny, C., 2016, June. Efficient multiline anchor systems for floating offshore wind turbines. In *International Conference on Offshore Mechanics and Arctic Engineering* (Vol. 49972, p. V006T09A042). American Society of Mechanical Engineers.
- [5]. Katsouris, G. and Marina, A., 2016. *Cost modelling of floating wind farms*. Petten, The Netherlands: ECN.
- [6]. Robert Speht, *WPED Contributor*, September 2021. [Ready-to-float: A permanent cost reduction for offshore wind \(windpowerengineering.com\)](https://www.windpowerengineering.com)
- [7]. Rummelhoff, I., 2017, October. World's first floating wind farm has started production. www.equinor.com. Retrieved February 10, 2022, from <https://www.equinor.com/news/archive/worlds-first-floating-wind-farm-started-production>
- [8]. Floatgen breaks new records in 2020., 2021, February. <https://www.floatgen.eu/>. Retrieved February 15, 2022, from <https://www.floatgen.eu/en/actualites/floatgen-breaks-new-records-2020>
- [9]. The WindFloat® advantage., 2020, December. <https://www.principlepower.com/>. Retrieved February 16, 2022, from <https://www.principlepower.com/windfloat/the-windfloat-advantage>
- [10]. Richard, C., 2018, August. Japanese floater ready for installation. <https://www.windpowermonthly.com/>. Retrieved April 1, 2022, from <https://www.windpowermonthly.com/article/1490217/japanese-floater-ready-installation>
- [11]. Musial, W., Butterfield, S. and Ram, B., 2006, May. Energy from offshore wind. In *Offshore technology conference*. OnePetro.
- [12]. Liang, G., Merz, K. and Jiang, Z., 2020, August. Modeling of a Shared Mooring System for a Dual-Spar Configuration. In *International Conference on Offshore Mechanics and Arctic Engineering* (Vol. 84416, p. V009T09A057). American Society of Mechanical Engineers.

- [13]. Ikhennicheu, M., Lynch, M., Doole, S., Borisade, F., MATHA, D., DOMINGUEZ, J., VICENTE, R., HABEKOST, T., RAMIREZ, L., POTESTIO, S. and MOLINS, C., 2021. Review of the state of the art of mooring and anchoring designs, technical challenges and identification of relevant DLCs.
- [14]. Benveniste, G., Lerch, M., de Prada, M., Kretschmer, M., Berqué, J., López, A. and Pérez, G., 2016. LCOE tool description, technical and environmental impact evaluation procedure. *LIFES50+ Deliv*, 2 (2).
- [15]. Beiter, P., Musial, W., Smith, A., Kilcher, L., Damiani, R., Maness, M., Sirnivas, S., Stehly, T., Gevorgian, V., Mooney, M. and Scott, G., 2016. *A spatial-economic cost-reduction pathway analysis for US offshore wind energy development from 2015–2030* (No. NREL/TP-6A20-66579). National Renewable Energy Lab. (NREL), Golden, CO (United States).
- [16]. Bjerkseter, C. and Ågotnes, A., 2013. *Levelised costs of energy for offshore floating wind turbine concepts* (Master's thesis, Norwegian University of Life Sciences, Ås).
- [17]. Hurley, W.L. and Nordstrom, C., 2014. *PelaStar Cost of Energy: A Cost Study floating foundation system in UK waters*. Technical report, Glosten Technology.
- [18]. Goldschmidt, M. and Muskulus, M., 2015. Coupled mooring systems for floating wind farms. *Energy Procedia*, 80, pp.255-262.
- [19]. Gao, Z. and Moan, T., 2009, September. Mooring system analysis of multiple wave energy converters in a farm configuration. In *Proceedings of the 8th European Wave and Tidal Energy Conference, Uppsala, Sweden* (pp. 7-10).
- [20]. Liang, G., Jiang, Z. and Merz, K., 2021. Mooring Analysis of a Dual-Spar Floating Wind Farm With a Shared Line. *Journal of Offshore Mechanics and Arctic Engineering*, 143(6).
- [21]. Luan, C., Gao, Z. and Moan, T., 2016, June. Design and analysis of a braceless steel 5-mw semi-submersible wind turbine. In *International Conference on Offshore Mechanics and Arctic Engineering* (Vol. 49972, p. V006T09A052). American Society of Mechanical Engineers.
- [22]. Roddier, D. and Weinstein, J., 2010. Floating wind turbines. *mechanical engineering*, 132(04), pp.28-32.
- [23]. Byrne, B.W. and Houlsby, G.T., 2003. Foundations for offshore wind turbines. *Philosophical Transactions of the Royal Society of London. Series A: Mathematical, Physical and Engineering Sciences*, 361(1813), pp.2909-2930.
- [24]. Siavashi, R., 2018. *Sensitivity analysis of the dynamic response of floating wind turbines* (Master's thesis, The University of Bergen).
- [25]. Beatrice Offshore Windfarm Ltd homepage. (2022). Beatrice Offshore Windfarm Ltd. Retrieved 2022, from <https://www.beatricewind.com/>.

- [26]. Scheu, M., Matha, D., Schwarzkopf, M.A. and Kolios, A., 2018. Human exposure to motion during maintenance on floating offshore wind turbines. *Ocean Engineering*, 165, pp.293-306.
- [27]. Jonkman, B.J. and Kilcher, L., 2012. *TurbSim user's guide: version 1.06. 00*. National Renewable Energy Laboratory: Golden, CO, USA.
- [28]. International Electrotechnical Commission, 2005. Wind turbines-part 1: design requirements. *IEC 61400-1 Ed. 3*.
- [29]. Wen, T.R., 2018. *Feasibility study and dynamic analysis of floating vertical axis wind turbines in multi-applications* (Master's thesis, University of Stavanger, Norway).
- [30]. SINTEF Ocean. *SIMO 4.10.1 Theory Manual*; SINTEF Ocean: Trondheim, Norway, 2017.
- [31]. Hansen, M., 2015. *Aerodynamics of wind turbines*. Routledge.
- [32]. Atcheson, M., Garrad, A., Cradden, L., Henderson, A., Matha, D., Nichols, J. and Sandberg, J., 2016. *Floating offshore wind energy*. Springer.
- [33]. Pettersen, B., 2007. *Marin teknikk 3-hydrodynamikk*. Dept. of Marin Techn. NTNU, Trondheim, Norway.
- [34]. Faltinsen, O., 1993. *Sea loads on ships and offshore structures* (Vol. 1). Cambridge university press.
- [35]. Gudmestad, O., 2015. *Marine technology and operations: Theory & practice*. WIT Press.
- [36]. Kvamen, J.O., 2020. *Mooring systems for floating wind turbine farms in deep water* (Master's thesis, NTNU).
- [37]. Cheng, Z., 2016. *Integrated dynamic analysis of floating vertical axis wind turbines* (Ph.D. Thesis, NTNU).
- [38]. Cheng, Z., Madsen, H.A., Gao, Z. and Moan, T., 2017. A fully coupled method for numerical modeling and dynamic analysis of floating vertical axis wind turbines. *Renewable Energy*, 107, pp.604-619.
- [39]. Wang, K., Moan, T. and Hansen, M.O.L., 2013, June. A method for modeling of floating vertical axis wind turbine. In *International Conference on Offshore Mechanics and Arctic Engineering* (Vol. 55423, p. V008T09A016). American Society of Mechanical Engineers.
- [40]. Veritas, D.N., 2010. Environmental conditions and Environmental loads (DNV-RP-C205). *Det Norske Veritas*.
- [41]. SINTEF, O., 2017. *RIFLEX 4.10. 1 User Guide*. SINTEF Ocean: Trondheim, Norway.
- [42]. Jonkman, J., Butterfield, S., Musial, W. and Scott, G., 2009. *Definition of a 5-MW reference wind turbine for offshore system development* (No. NREL/TP-500-38060). National Renewable Energy Lab.(NREL), Golden, CO (United States).

- [43]. Li, L., Gao, Z. and Moan, T., 2015. Joint distribution of environmental condition at five European offshore sites for design of combined wind and wave energy devices. *Journal of Offshore Mechanics and Arctic Engineering*, 137(3).
- [44]. Barj, L., Jonkman, J.M., Robertson, A., Stewart, G.M., Lackner, M.A., Haid, L., Matha, D. and Stewart, S.W., 2014. Wind/wave misalignment in the loads analysis of a floating offshore wind turbine. In *32nd ASME wind energy symposium* (p. 0363).
- [45]. Luan, C., Michailides, C., Gao, Z. and Moan, T., 2014, June. Modeling and analysis of a 5 MW semi-submersible wind turbine combined with three flap-type wave energy converters. In *International Conference on Offshore Mechanics and Arctic Engineering* (Vol. 45547, p. V09BT09A028). American Society of Mechanical Engineers.

Appendix A

Research paper

Global analysis of floating offshore wind turbines with shared mooring system.

Hammad Munir, Chern Fong Lee and Muk Chen Ong

Published in *IOP Conference Series: Materials Science and Engineering* (Vol. 1201, No. 1, p. 012024). IOP Publishing

Global analysis of floating offshore wind turbines with shared mooring system

H Munir¹, C F Lee^{1,*}, M C Ong¹

¹University of Stavanger, Norway

*chern.f.lee@uis.no

Abstract. Floating wind turbines (FWTs) with shared mooring systems can be one of the most cost-effective solutions in reducing mooring costs. First, the static configuration of a shared line is estimated using the elastic catenary equation. The present study investigates the global responses of two FWT with a shared mooring system. Two shared mooring configurations with different horizontal distances between the FWTs are considered. In the first configuration, the FWTs are placed 750m apart; and in the second configuration, they are placed 1000m apart. Two different environmental conditions (ECs) are used to simulate the global responses of the system in time domain. The shared mooring line results in higher extreme motions in surge and sway (degree of freedoms) DOFs due to the reduction of mooring restoring stiffness. The lower mooring restoring stiffness can be attributed to the reduction of one seabed anchoring point for each FWT as compared to a single FWT with three anchors installed. In the rotational DOFs, the shared mooring line configurations result in slight mean offset in each direction and significant increase in the motion standard deviations. This is caused by the reduced mooring stiffness associated with the change in platform orientation.

1. Introduction

Floating Wind Turbines (FWTs) is getting more attention in the wind energy sector during the last decade due to the availability of large wind resources at deeper waters. Better sea transport facilities like large towing vessels and heavy lift cranes have made this concept even more feasible. FWTs are becoming one of the most promising means of energy production, especially in deep-water regions. The reason behind this is the reduced friction offshore, the stronger wind production with small turbulence on average and to avoid noise and visualization pollution due to the large distance from populated areas [1]. Thus, a lot of research has been conducted around the design of FWTs to make it more efficient, cost effective and sustainable.

However, due to a requirement of a more compliant supporting structure to control the dynamic motions of the wind turbine within acceptable limits, the cost of the floating structure remains one of the biggest challenges in way of the full deployment of commercialized floating wind farms. The 5-MW-CSC is a braceless semi-submersible platform proposed in [1] to support the NREL 5-MW horizontal axes wind turbine [2]. Research on this concept is relatively less as compared to the other similar concepts like DeepCwind OC4 by [3], OC3-Hywind by [4] and WindFloat by [5].

One of the most promising ways to minimize the levelized cost of energy (LCoE) is to reduce the structural weight by minimizing the number of components. When considering the floating offshore wind farms (FOWFs), sharing of mooring lines between neighboring FOWTs is an attractive concept to reduce the LCoE and the complexity of installation activities. The total number of mooring lines is decreased through the sharing of mooring line between two adjacent floating wind turbines (FWTs). The number of anchors required lowers as well, resulting in further cost reduction.

In the present study, the global responses of two 5-MW-CSC FWTs with one shared mooring line in extreme wind and wave conditions are investigated. To provide comparability with the results presented by Luan et al. [1], the specifications of the mooring lines that run from the fairleads to anchors remain unchanged. For the shared mooring line, the static configuration is estimated using elastic catenary equation. The motion responses are calculated using time domain simulations and compared against the case of a single FWT presented by Luan et al. [1].

2. CSC wind turbine & methodology

2.1 CSC floating wind turbine

The supporting platform of a 5-MW- CSC was designed to accommodate a 5-MW NREL offshore base line wind turbine. The 5-MW-CSC is composed of a rotor nacelle assembly (RNA), tower, hull and mooring system as shown in Figure 1. The hull of 5-MW-CSC consists of one central, three side columns and three pontoons. The tower is mounted on the central column in the middle from which the three side columns are placed at an equidistant offset. The ballast mass is symmetrically distributed about the central line of the central column. Ballast water is used to achieve the operating draft and the pontoons are completely filled with ballast water. The hull structure is modelled as a rigid body with master-slave connections to the tower base and the fairleads for mooring line connections. The mooring system is composed of three catenary chain mooring lines spread symmetrically at 120° about the z_g -axis of the platform. The chain mooring lines are simplified as a uniformly distributed mass with a solid cross-section as proposed in [1]. The body fixed coordinate system of 5-MW-CSC is coincident to the global coordinate system. The 0° and 90° directions are defined as the positive directions in x_g and y_g , respectively as shown in Figure 2. In the present study, hydrodynamic studies for the 5-MW-CSC hull have been performed using the linear potential flow program WADAM [6] and validated against the result presented by Luan et al. [1]. The hydrodynamic coupling (added mass and damping) between the two FWTs is neglected due to the long distance between the two rigid bodies. The response amplitude operators (RAOs) in different wave directions for the surge, heave and pitch DOFs are presented in Appendix A.

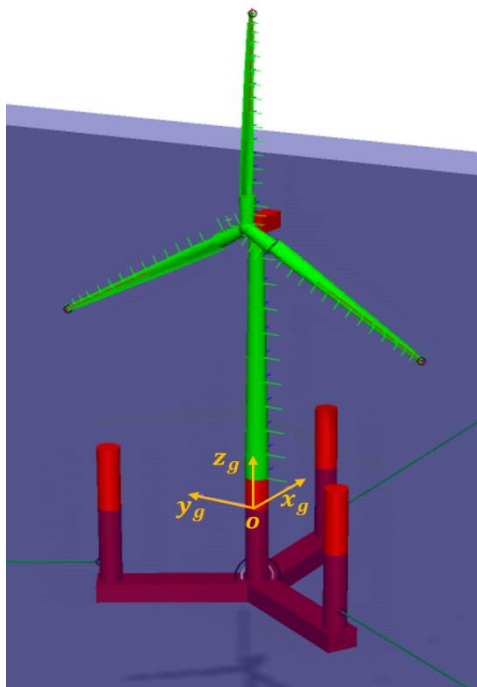


Figure 3. CSC-5-MW single wind turbine model.

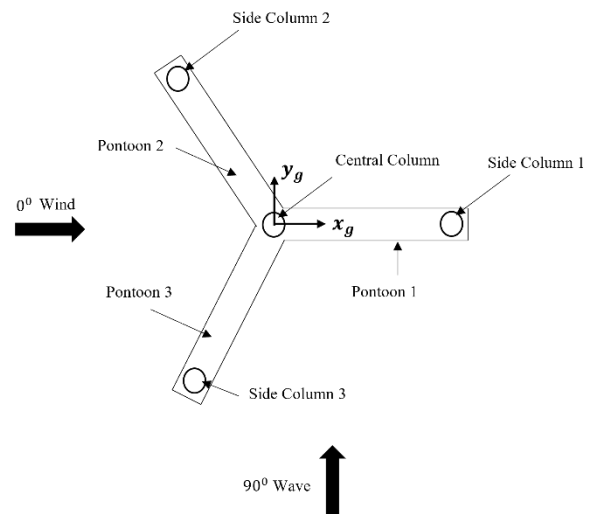


Figure 4. Top view of the hull of 5-MW-CSC.

2.2 Single mooring lines modelling

Mooring lines are station keeping devices which are designed in such a way to provide a sufficient restoring force for the floating platforms in various environmental conditions. The 5MW-CSC FWT is moored with three catenary chain mooring lines spread symmetrically at 120° about the platform z-axis as described in [1]. Same configurations are used in the present study for single mooring lines design in which each wind turbine is modelled with two side catenary chain single mooring lines spread at 120° and one shared mooring line. The stiffnesses of mooring lines consist of material and geometrical stiffness. The force-displacement properties of a catenary system are dependent on material properties,

line geometry and mooring system configuration. The single mooring line properties are summarized in Table 1. Moreover, the static configuration and effective tension of the used catenary single mooring lines are presented in Figure 3 and Figure 4, respectively.

Table 1. Single mooring line properties.

| Property | |
|---|--------------------|
| Mooring line type [-] | Chain |
| Mooring line mass density [kg/m] | 115 |
| Un-stretched mooring line length [m] | 1,073 |
| Mooring line diameter [m] | 0.137 |
| Extensional stiffness of mooring line [kN/m] | 3.08×10^6 |
| Depth of fair lead below sea water line (SWL) [m] | 18 |
| Depth of anchors [m] | 200 |
| Density of material [kg/m ³] | 7,850 |

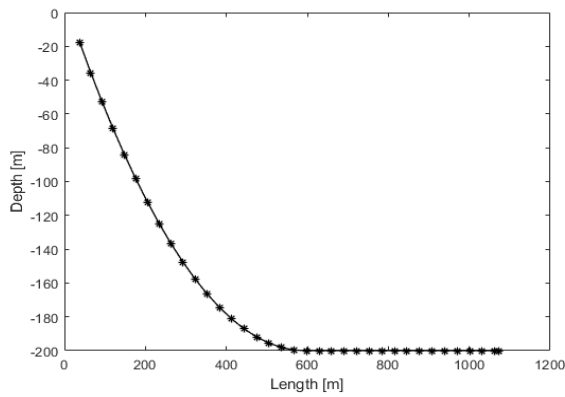


Figure 3. Single mooring line shape in dual CS system.

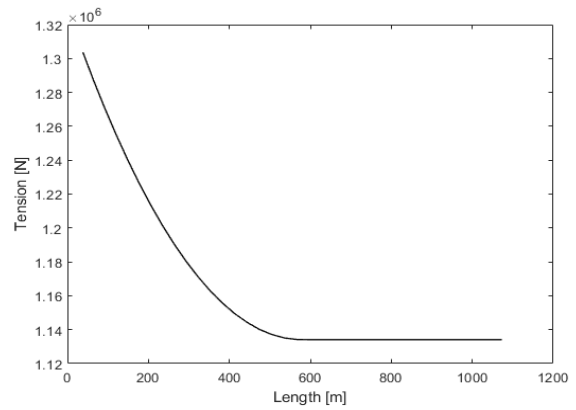


Figure 4. Axial effective tension of single mooring line.

2.3 Shared mooring line modelling

Basic catenary equations are applicable for shared mooring line design when the two fairleads are on the same level. The mooring line can be designed as two symmetric lines shape connected at the sagging point. Various assumptions are made against the modelling of a shared mooring line such that the dynamic effects, bending effects and current forces effects on mooring lines can be neglected as proposed by Liang et al. [7]. The origin of the catenary plane is set at the fairlead as shown in Figure 5. By setting one end of the shared line as the origin of a catenary plane, the elastic catenary equations, Eqn. 1 and Eqn. 2 are applied [7].

$$x = \frac{H}{w} \log \left(\frac{\sqrt{H^2 + V^2} + V}{H} \right) + \frac{H}{EA} S \quad (1)$$

$$h = \frac{1}{2} \frac{ws^2}{EA} + \frac{H}{w} \left[\frac{1}{\cos \phi} - 1 \right] \quad (2)$$

where x and h are the horizontal and vertical distance of the sagging point measured from the fairlead, H and V are the horizontal and vertical components of the mooring tension T at the fairlead 1, s is the total suspended length of the shared line, w is the weight per unit length of the mooring line in water, EA is the extensional stiffness of the line with E as the elastic modulus and A is the cross-sectional area. With the distances between the fairlead and the sagging point known and with an initial guess of s and h , the final suspended length can be solved by iteration. The resulting tension at fairleads can then be calculated. The tension of the shared mooring line is adjusted to achieve horizontal force balance by modifying the vertical distance of the sagging point.

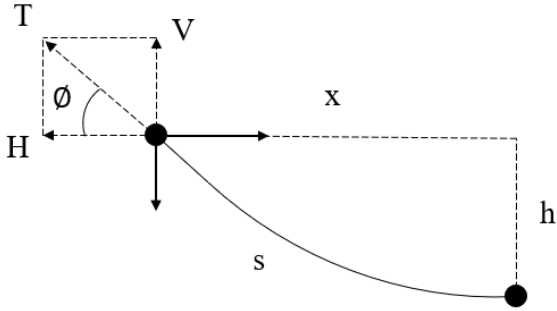


Figure 5. Illustration of shared line in catenary plane.

The properties of shared mooring line and its static configurations are shown in Table 2 and in Figure 6, Figure 7 & Figure 8.

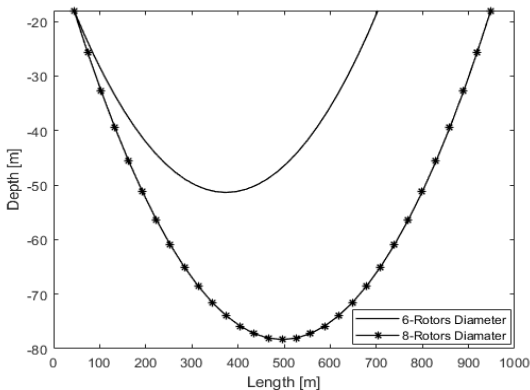


Figure 6. Line shape in the catenary plane for the shared line.

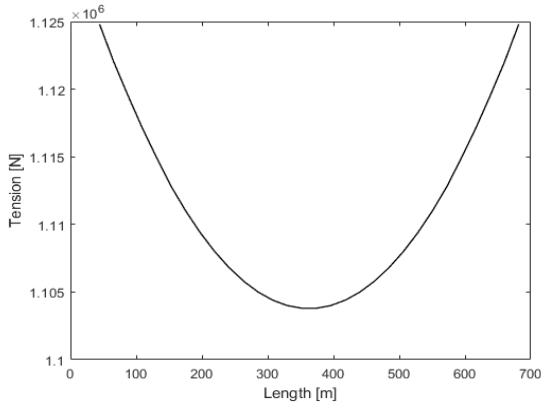


Figure 7. Shared line tension with 6 rotors diameter configuration.

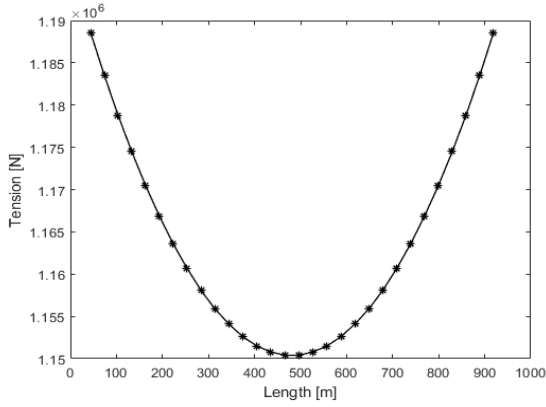


Figure 8. Shared line tension with 8 rotors diameter configuration.

2.4 Wind turbines configuration

In the present study, two different shared line configuration are investigated. In the first configuration, the FWTs are placed 750m (six rotor diameters) apart; in the second configuration, they are placed 1000m (8 rotor diameters) apart. In order to accommodate the shared mooring line, the floating platforms are rotated by 30° and -30° for FWT 1 and FWT2, respectively as compared to the original 5MW-CSC FWT. A plan view of the two-FWT configuration is as shown in Figure 9. Following the recommendation by Liang et al. [7], the properties of the shared mooring line are summarized in Table 2. Two wind turbines are placed with shafts along the x_g -axis in the global coordinate system with the wind turbines facing the upwind direction as shown in Figure 9. The focus in the present study is the comparison of responses of FWTs with waves coming from 0° to 180° against the responses of a single FWT. Wind is constantly directed at 0° (positive x_g -direction) into the rotor plane of wind turbines. The shared line is positioned along the sway direction (y_g) in the present model. The shared line is modelled using 30 bar elements with a total length of 661.4 m and 911.4 m for the first and second configuration, respectively.

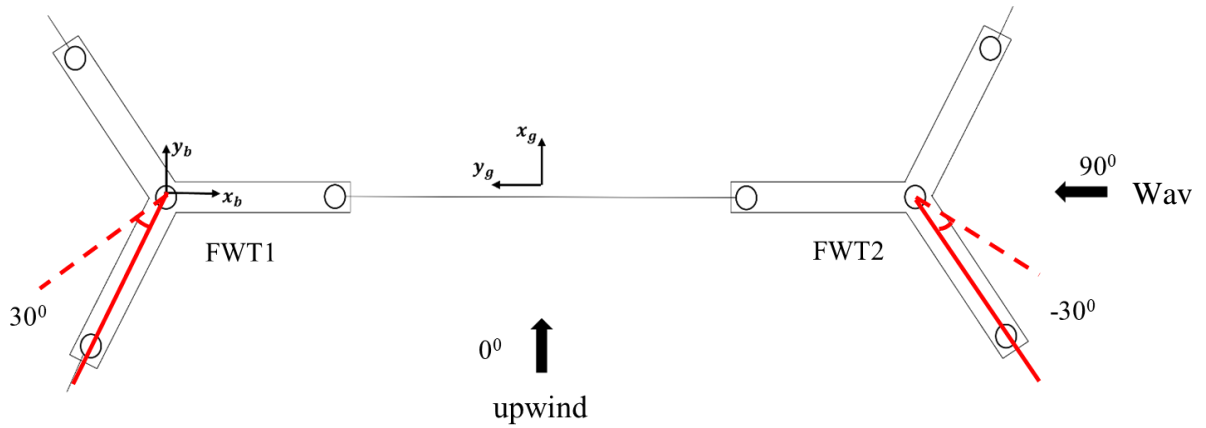


Figure 9. Floating Wind Turbines Configuration.

Table 2. Shared Mooring Line Properties for CSC-Wind Turbines at Two Horizontal Distances.

| Property | |
|---------------------------|--------------------|
| Mooring line type [-] | Chain |
| Mass density [kg/m] | 72 |
| Diameter [m] | 0.06 |
| Weight in water [N/m] | 649.46 |
| Extensional stiffness [N] | 3.38×10^8 |
| Maximum breaking load [N] | 4.52×10^6 |

3. Environmental conditions (ECs)

Joint probability density function (PDF) of mean wind speed (U_W), significant wave height (H_S) and peak period of wave spectrum (T_P) and the environmental contour of U_W , H_S and T_P corresponding to a 50-year return period are described in [8]. Two parameter JONSWAP spectrum is employed with a peak factor of 3.3 to describe the waves while the wind is described by the Kaimal wind spectrum with normal turbulence. Turbulent wind fields are generated using Turbsim [9] and as a simplification, it is assumed that both wind turbines are experiencing identical wind field in each EC. In order to assess the global responses of FWTs, one operational loading condition above the rated wind speed for wind-dominant case and one extreme loading condition for wave-dominant case with parked wind turbine are considered [10, 11] as listed in Table 3. For each EC, H_S is selected as the maximum value on the contour surface corresponding to the chosen U_W . Seven different wave incident directions varying from 0° to 180° with 30° interval is used to consider the effects of waves coming from different directions.

Table 3. Environmental Conditions for global response study.

| | Turbulence Intensity [%] | Wind Speed [m/s] | Hs [m] | Tp [s] | Note |
|-----|--------------------------------|------------------------|--------|--------|-------------|
| EC1 | 12 | 20 | 10.3 | 14.7 | Operational |
| EC2 | 11 | 40.4 | 15.3 | 14.3 | Parked |

4. Results and discussions

4.1 Case study A

To obtain the global responses of the FWTs under wind and wave loads, numerical simulations are carried out in time domain using SIMA, a simulation software for marine operations [12, 13]. To account for statistical uncertainty, six 1-hr simulations with distinct random seeds are carried out. The average statistical properties based on six 1-hr simulations are plotted in Figure 10. In the present paper, the platform motions of both FWTs connected with a shared mooring line are to be compared against the platform motions of a single FWT. As such, for each platform's DOF, one most significant wave direction is selected, and the corresponding average statistical properties are summarized in Table 4. In comparison, the statistical properties for a single FWT under the same environmental loads and incident wave directions documented in [1] are presented in Table 5.

For EC1, with a 0° incident wave direction, the mean surge offsets of FWT1 and FWT2 are similar to the case of a single FWT. However, both FWT1 and FWT2 achieve higher maximum and lower minimum surge motion, suggesting a lower mooring restoring stiffness in the surge direction. The lower mooring restoring stiffness can be attributed to the reduction of one seabed anchoring point for each

FWT as compared to a single FWT with three anchors installed. Similar behavior in the surge direction can be observed under EC2, with an even greater difference in the negative surge direction.

For sway DOF, the response in 90^0 incident waves is compared. The mean positions of both FWT1 and FWT2 increase as compared to a single FWT and the increment is more significant in EC2 due to the higher waves. Both FWT1 and FWT2 achieve higher maximum and lower minimum sway motion due to the reduced mooring restoring stiffness in the sway direction. The shared mooring configuration increases the standard deviation of sway motion by approximately 50% and 22% for EC1 and EC2, respectively as compared to the single FWT. As expected, the heave motions of both FWT1 and FWT2 are dominated by buoyancy force and are in general displaying the same characteristic as compared to the case of a single FWT.

Based on the above observations, it is shown that the shared mooring line has a considerable effect on surge and sway motions of the platforms. The effect of a reduction in mooring restoring stiffness in the horizontal translational DOF is reflected through an increase in mean and maximum horizontal offset of the FWTs. The increase is more significant in the sway DOF as only two mooring lines are contributing to the restoring force of both FWTs.

For pitch DOF, the response in 0^0 incident waves is compared. The pitch motion of FWT1 is in general similar to the motion of a single FWT. However, FWT2 is having a smaller mean pitch angle in the downwind direction (-0.7^0). It is later observed that even when there is no wind, the neutral position of FWT2 is with a pitch offset of approximately 2^0 in the upwind direction. This has eventually resulted in FWT2 having a smaller mean pitch angle downwind. It is also shown that the use a shared mooring line resulted in an increase in the standard deviation of pitch motion. The increment is more prominent in EC1 with a 100% increment for FWT1.

For roll DOF, the response in 0^0 incident waves is compared. Roll motion is dominated by the influence of the shared mooring line. The configuration of the shared mooring line causes a mean roll offset that is different from the case with a single FWT. For FWT2, the shared mooring line configuration resulted in an increase in roll motion standard deviation by approximately 100% in EC1.

For yaw DOF, the responses of FWT1 and FWT2 in 120^0 incident waves is compared against the response of a single FWT in 90^0 incident waves due to different platform orientations. Significant reduction in the yaw standard deviation is observed for FWT2 in EC1.

Table 4. Maximum statistical properties of FWTs at 6 rotors diameter distance with different wave headings.

| ECs | Turbines | Statistical Properties | Surge | Sway | Heave | Roll | Pitch | Yaw |
|-----|----------|------------------------|------------------------|-------------------------|------------------------|---------------------------|--------------------------|----------------------------|
| | | | *0 ⁰ [m] | *90 ⁰ [m] | *0 ⁰ [m] | *90 ⁰ [deg] | *0 ⁰ [deg] | *120 ⁰ [deg] |
| EC1 | FWT1 | Max | 8.8 | 6.5 | 3 | 0.9 | 6.8 | 2.2 |
| | | Min | -0.9 | -4.7 | -3.4 | -3.3 | -0.2 | -3.7 |
| | | Mean | 3.6 | 0.8 | -0.3 | -1.2 | 3.3 | -0.5 |
| | | Std | 1.5 | 1.5 | 1 | 0.6 | 1 | 0.8 |
| | FWT2 | Max | 9 | 6.4 | 3 | 7.2 | 1.6 | 2.4 |
| | | Min | -0.9 | -4.9 | -3.4 | 1.3 | -3.1 | -2.2 |
| | | Mean | 3.8 | -0.1 | -0.3 | 4.3 | -0.7 | 0 |
| | | Std | 1.5 | 1.6 | 0.9 | 1 | 0.8 | 0.1 |
| EC2 | FWT1 | Max | 9.2 | 11.1 | 4.4 | 0.1 | 4 | 2 |
| | | Min | -5.1 | -5 | -4.7 | -5 | -2.5 | -2.4 |
| | | Mean | 1.6 | -3.3 | -0.2 | -2.3 | 0.6 | -0.1 |
| | | Std | 2.1 | 2.2 | 1.3 | 0.7 | 0.8 | 0.6 |
| | FWT2 | Max | 9.1 | 12.3 | 4.4 | 2.7 | 0.9 | 2.7 |
| | | Min | -5.1 | -3.5 | -4.7 | -0.3 | -3.6 | -1.3 |
| | | Mean | 1.5 | 2.9 | -0.2 | 1.3 | -1.1 | 0.5 |
| | | Std | 2.1 | 2.3 | 1.3 | 0.4 | 0.5 | 0.6 |

* incident wave direction

Table 5. Maximum statistical properties of single wind turbine proposed in [1].

| ECs | Statistical Properties | Surge | Sway | Heave | Roll | Pitch | Yaw |
|-----|------------------------|------------------------|-------------------------|------------------------|---------------------------|--------------------------|---------------------------|
| | | *0 ⁰ [m] | *90 ⁰ [m] | *0 ⁰ [m] | *90 ⁰ [deg] | *0 ⁰ [deg] | *90 ⁰ [deg] |
| EC1 | Max | 8.5 | 4.5 | 3.5 | 3 | 6.8 | 1.9 |
| | Min | -0.5 | -4 | -3 | -2 | 0 | -2.6 |
| | Mean | 3.5 | 0.1 | 0.1 | 0.5 | 3 | -0.2 |
| | Std | 1.5 | 1 | 0.8 | 0.5 | 0.5 | 0.6 |
| EC2 | Max | 10 | 9 | 5.5 | 3 | 4.2 | 1.8 |
| | Min | -4.5 | -5 | -5 | -4.2 | -2.2 | -2.1 |
| | Mean | 1.8 | 0.8 | 0.2 | -0.3 | 0.5 | 0.1 |
| | Std | 2.1 | 1.8 | 1.5 | 0.6 | 0.5 | 0.5 |

* incident wave direction

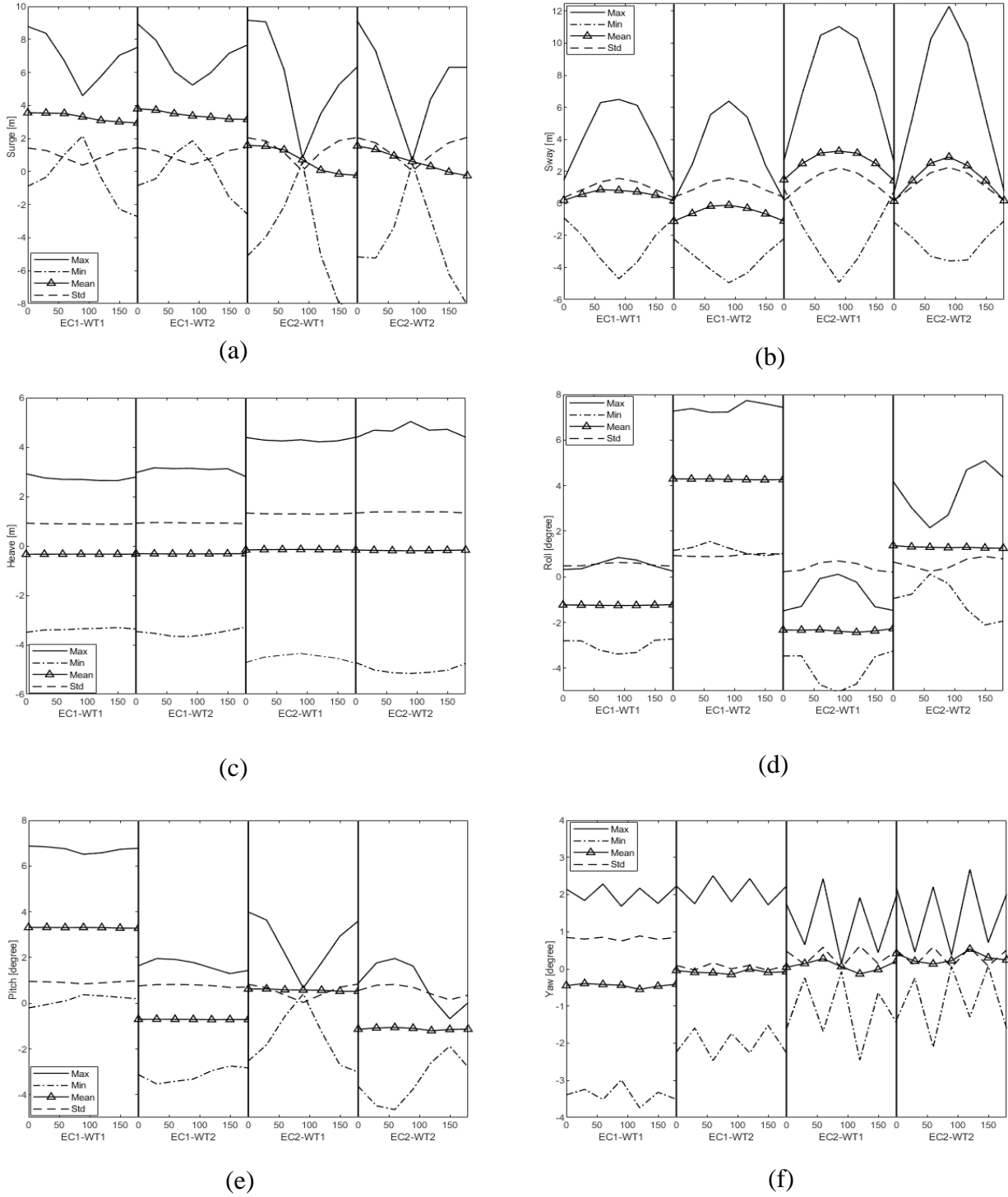


Figure 10: Statistical properties of dual 5-MW CSC at 6 rotors diameter distance in extreme combined wind and waves. For each condition, from the left end to the right end, wave direction varies from 0° to 180° with 30° intervals.

4.2 Case study B

In the second configuration, two wind turbines are placed at eight rotors diameter distance along the y_g -axis. A longer mooring line is used but with the rest of the properties remain the same as the first configuration. Similar procedure as described in Section 4.1 has been carried out to obtain the global responses of both FWTs. The average statistical results are plotted in Figure 11 and summarized in Table 6.

The second configuration aims at investigating the effect of varying distance between two FWTs. As discussed in Section 4.1, similar effect in the surge and sway DOF is observed. The mooring restoring stiffness in these two DOFs is reduced resulting in higher motion standard deviation as well as higher extreme motions. However, despite a slight change in sway mean offset, which is due to the design of the shared mooring line, motions in all DOF remain generally unchanged as compared to the first configuration. It demonstrates that changing the length of shared mooring line has little effect on the responses of FWTs. This is because the tension in a shared line contributes very little in restoring force and moment.

Table 6. Maximum statistical properties of FWTs at 8 rotors diameter distance with different wave headings.

| ECs | Turbines | Statistical Properties | Surge | Sway | Heave | Roll | Pitch | Yaw |
|-----|----------|------------------------|------------|-------------|------------|---------------|--------------|----------------|
| | | | *0° [m] | *90° [m] | *0° [m] | *90° [deg] | *0° [deg] | *120° [deg] |
| EC1 | FWT1 | Max | 8.7 | 5.7 | 3.1 | 1.3 | 6.8 | 2.3 |
| | | Min | -1 | -4.8 | -3.3 | -3 | -0.2 | -3.7 |
| | | Mean | 3.5 | 0.1 | -0.2 | -1 | 3.3 | -0.5 |
| | | Std | 1.4 | 1.5 | 0.9 | 0.6 | 1 | 0.8 |
| | FWT2 | Max | 8.9 | 4.7 | 3.1 | 7.2 | 2 | 2.4 |
| | | Min | -0.9 | -5.7 | -3.3 | 1 | -2.9 | -1.5 |
| | | Mean | 3.7 | -0.6 | -0.2 | 4.1 | -0.4 | 0.4 |
| | | Std | 1.5 | 1.5 | 1 | 1 | 0.8 | 0.5 |
| EC2 | FWT1 | Max | 9.2 | 10.5 | 4.5 | 0.2 | 4 | 1.9 |
| | | Min | -8 | -4.1 | -4.6 | -4.5 | -2.6 | -2.3 |
| | | Mean | 1.6 | 2.6 | 0 | -2 | 0.6 | -0.1 |
| | | Std | 2.1 | 2.1 | 1.3 | 0.6 | 0.8 | 0.6 |
| | FWT2 | Max | 9.1 | 9.6 | 4.5 | 2.5 | 1.2 | 2.8 |
| | | Min | -5.2 | -4.6 | -4.5 | -0.4 | -3.4 | -1.3 |
| | | Mean | 1.5 | 2.1 | 0 | 1.1 | -0.8 | 0.5 |
| | | Std | 2.1 | 2.1 | 1.4 | 0.4 | 0.6 | 0.6 |

* incident wave direction

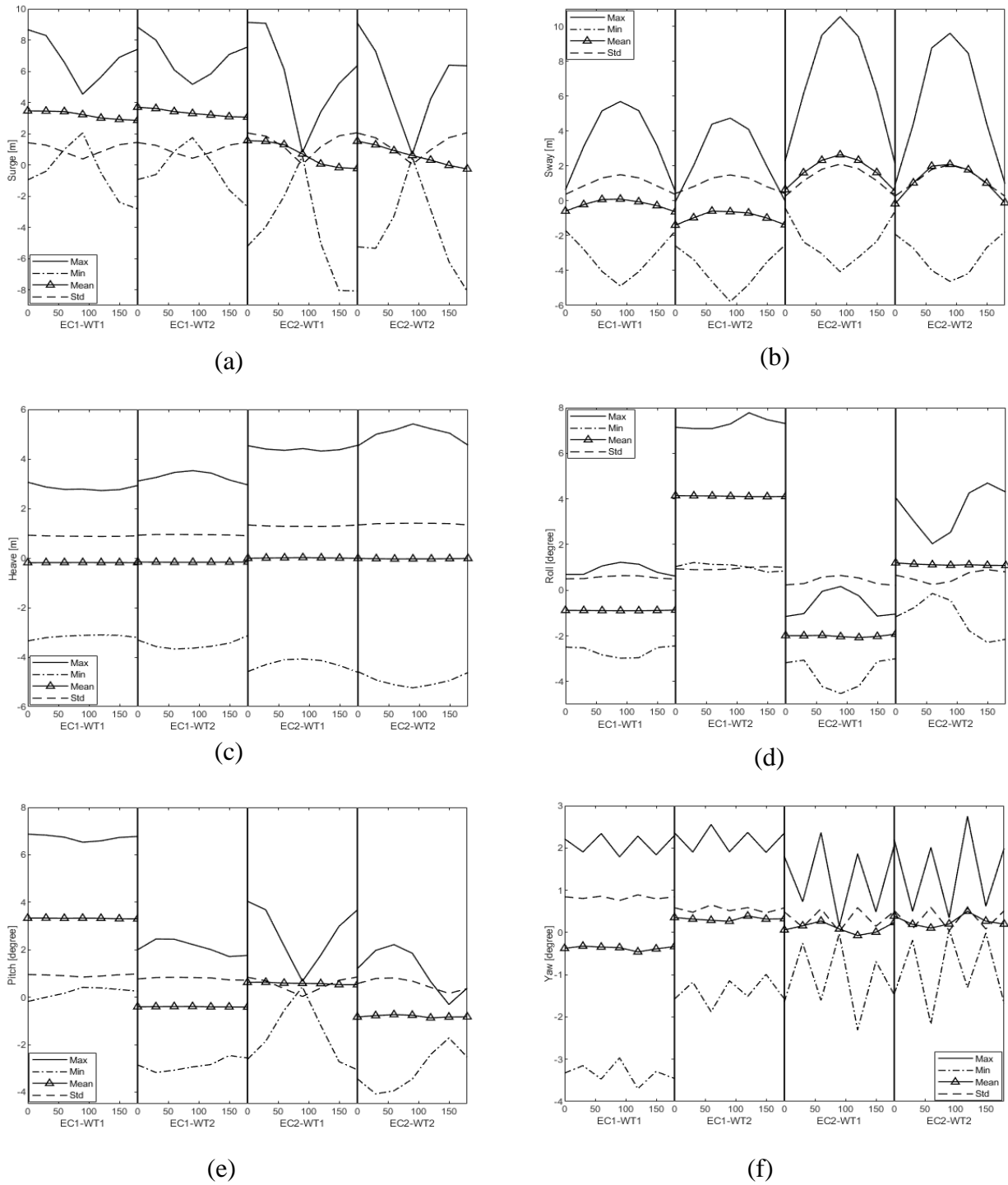


Figure 11: Statistical properties of dual 5-MW CSC at 8 rotors diameter distance in extreme combined wind and waves. For each condition, from the left end to the right end, wave direction varies from 0° to 180° with 30° intervals.

5. Conclusion and future works

The dual CSC-5MW FWTs with a shared mooring line at two horizontal distances are modelled in this paper. The rigid body motions in 6 DOFs of each wind turbines are compared against the single wind turbine model and discussed in Sections 4.1 and 4.2. Global time-domain analysis has been carried out to calculate the global responses in two selected combined wind and wave conditions. While a shared mooring system allows for cost savings for floating wind farms, it also adds complexity to the dynamic behavior of the system. Basic catenary equation is employed to design the shared mooring line. The shared mooring line results in higher maximum motion and lower minimum motion in the surge and sway DOFs due to the reduction of mooring restoring stiffness. In the rotational DOFs, the shared mooring line configurations result in slight mean offset in each direction and significant increase in the motion standard deviations. This is caused by the reduced mooring stiffness associated with the change in platform orientation. The effect of different distances between FWTS has been investigated. For different distances between FWTs, the difference in motions in all DOF is not significant as the shared line contributes little to the restoring force.

The study in the present paper aims at establishing a model for preliminary investigation of dynamic behavior of two FWTs connected by a shared line. Future studies should be carried out focusing on the behavior in more specific environment conditions and detailed design of mooring line.

6. References

- [1] Luan C, Gao Z and Moan T 2016 Design and analysis of a braceless steel 5-mw semi submersible wind turbine, *Int. Conf. on OMAE* (American Society of Mechanical Engineers) vol. 49972.
- [2] Jonkman J, Butterfield S, Musial W and Scott G 2009 Definition of a 5-MW reference wind turbine for offshore system development (No. NREL/TP-500-38060). National Renewable Energy Lab.(NREL), Golden, CO (United States).
- [3] Robertson A, Jonkman J, Masciola M, Song H, Goupee A, Coulling A and Luan C 2014 Definition of the semisubmersible floating system for phase II of OC4 (No. NREL/TP-5000-60601). National Renewable Energy Lab.(NREL), Golden, CO (United States).
- [4] Jonkman J 2010 Definition of the Floating System for Phase IV of OC3 (No. NREL/TP-500-47535). National Renewable Energy Lab.(NREL), Golden, CO (United States).
- [5] Roddier D, Cermelli C, Aubault A and Weinstein A 2010 WindFloat: A floating foundation for offshore wind turbines, *J. Renew. Sustain. Energy*, **2**(3), p.033104.
- [6] DNV GL 2019 SESAM User Manual, WADAM (Høvik, Norway).
- [7] Liang G, Merz K and Jiang Z 2020 Modeling of a Shared Mooring System for a Dual-Spar Configuration *Int. Conf. on OMAE* (American Society of Mechanical Engineers) vol 84416.
- [8] Li L, Gao Z., Moan T 2015 Joint Distribution of Environmental Condition at Five European Offshore Sites for Design of Combined Wind and Wave Energy Devices, *J. Offshore Mech. Arct. Eng.* **137**(3).
- [9] Jonkman B J and Buhl Jr. M L 2006 Turbsim user's guide. Tech. rep., National Renewable Energy Lab.(NREL), Golden, CO (United States).
- [10] IEC, 2005. International standard IEC 61400-1, Wind turbines—Part 1: Design requirements (Geneva, Switzerland).
- [11] IEC, 2009. International standard IEC 61400-3, Wind turbines—Part 3: Design requirements for offshore wind turbines (Geneva, Switzerland).
- [12] SINTEF Ocean 2019. SIMO 4.10.1 User Guide (Trondheim, Norway).
- [13] SINTEF Ocean 2019. RIFLEX 4.16.0 User Guide (Trondheim, Norway).

Appendix A

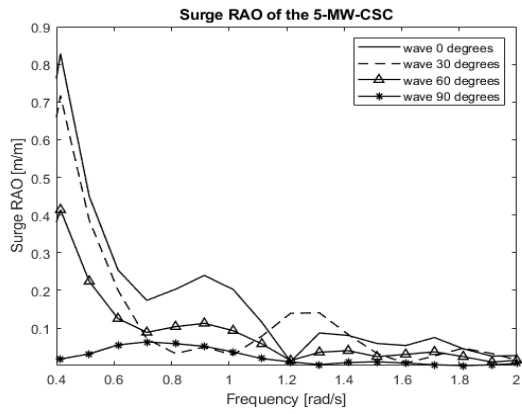


Figure 12. Surge RAO of the 5-MW-CSC

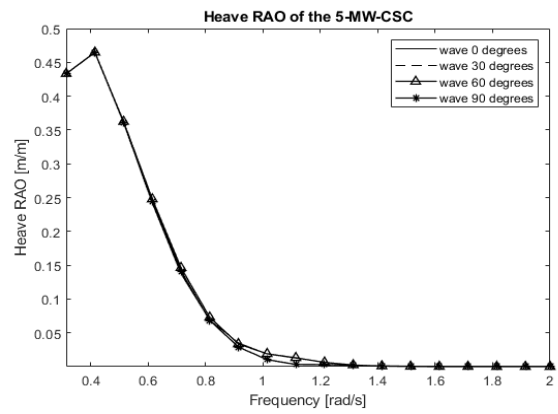


Figure 13. Heave RAO of the 5-MW-CSC

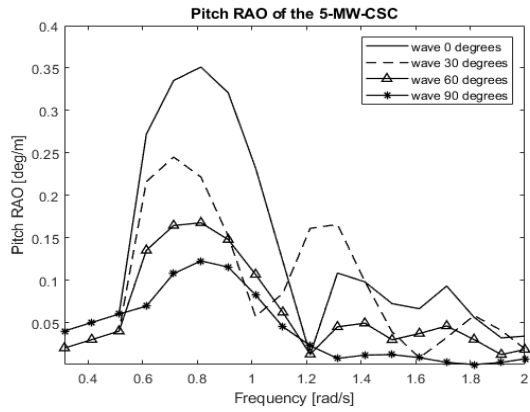
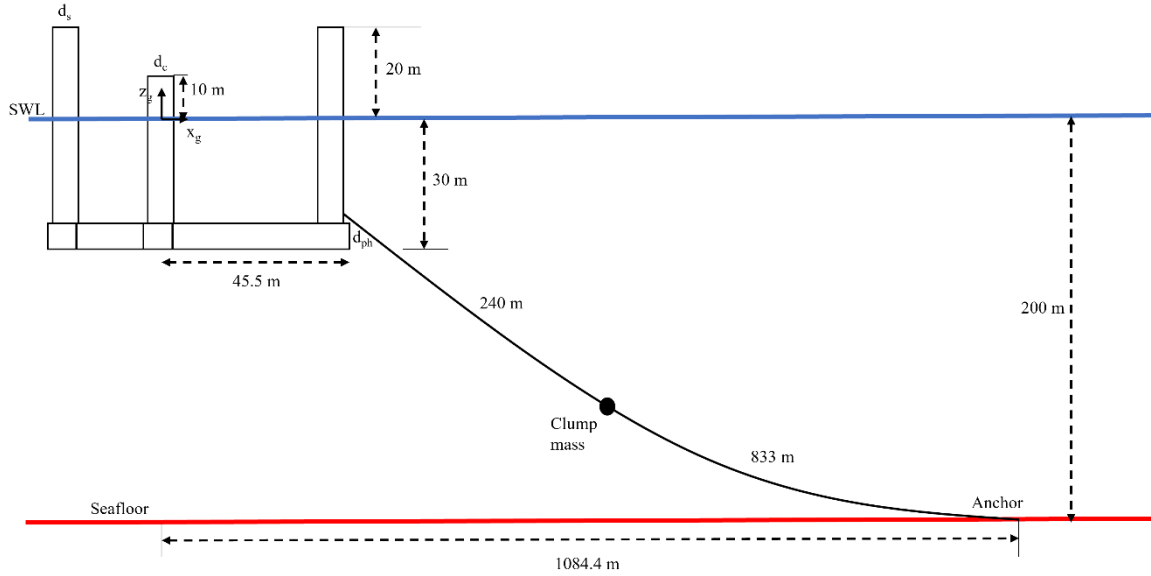


Figure 14. Pitch RAO of the 5-MW-CSC

Appendix B

Calculation sheet for a single CSC model

Appendix B: Calculation Sheet- Stability Check for a single CSC model



Input Data:

CSC data

| | | |
|----------------------------|--------|-----------------------|
| $d_s =$ | 6 | [m] |
| $d_c =$ | 6 | [m] |
| $d_{ph} =$ | 6.5 | [m] |
| $\rho_{steel} =$ | 8 | [ton/m ³] |
| $\rho_{sea\ water} =$ | 1.025 | [ton/m ³] |
| $Z_{csc,\ top} =$ | 10 | [m] |
| $M_{hull\ and\ ballast} =$ | 9880 | [ton] |
| $Z_{hull\ and\ ballast} =$ | 5.64 | [m] |
| $M_{tower} =$ | 249 | [ton] |
| $Z_{tower} =$ | 85 | [m] |
| $M_{nacelle} =$ | 294 | [ton] |
| $Z_{nacelle\ and\ hub} =$ | 119.35 | [m] |
| $M_{blades} =$ | 53 | [ton] |
| $Z_{blades\ and\ hull} =$ | 119.35 | [m] |
| $M_{structure} =$ | 10390 | [ton] |

Mooring line data

| | | |
|-----------------|-------|-------------------|
| $L_{mooring} =$ | 1073 | [m] |
| $W_{mooring} =$ | 0.115 | [ton/m] |
| $V_{clump} =$ | 2 | [m ³] |
| $W_{clump} =$ | 15000 | [kg] |

Environmental data

| | | |
|------------------|------|-----|
| $Z_{SWL} =$ | 0 | [m] |
| $Z_{seafloor} =$ | -200 | [m] |

Center of gravity:

$$COG = \frac{\sum M_i \times z_i}{\sum M_i}$$

$$COG \text{ from hull bottom} = \frac{9880 \times 5.64 + 249 \times 85 + 294 \times 119.35 + 53 \times 119.35}{10390} = 11.38 \text{ [m]}$$

$$COG \text{ from MWL} = 30 - 11.38 = -18.61 \text{ [m]}$$

Center of buoyancy:

| Type | Z _{underwater_low} [m] | Z _{underwater_up} [m] | Z _b [m] | h _i [m] | A _{wp} [m ²] | V _i [m ³] |
|-----------------|------------------------------------|-----------------------------------|-----------------------|-----------------------|--------------------------------------|-------------------------------------|
| Central column | -24 | 0 | -12 | 24 | 33.18 | 796.4 |
| Side column x 3 | -24 | 0 | -12 | 24 | 99.55 | 2389.2 |
| Pontoon x 3 | -30 | -24 | -27 | 6 | 1158.4 | 6950.1 |

$$z_{b,i} = z_{underwater_low} + \frac{z_{underwater_up} - z_{underwater_low}}{2}$$

$$\text{Displacement} = \sum V_i = 10135.7 \text{ [m]}$$

$$\text{Total Buoyancy, } COB = \frac{\sum V_i \times z_{b,i}}{\sum V_i} = -22.3 \text{ [m]}$$

Mooring line tension:

$$\text{Water depth from fairlead to bottom, } h = 182 \text{ [m]}$$

$$\text{Length of catenary, } S = 667 \text{ [m]}$$

$$\text{Horizontal force, } H = \frac{W}{2h} (S^2 - h^2) = 1431 \text{ [kN]}$$

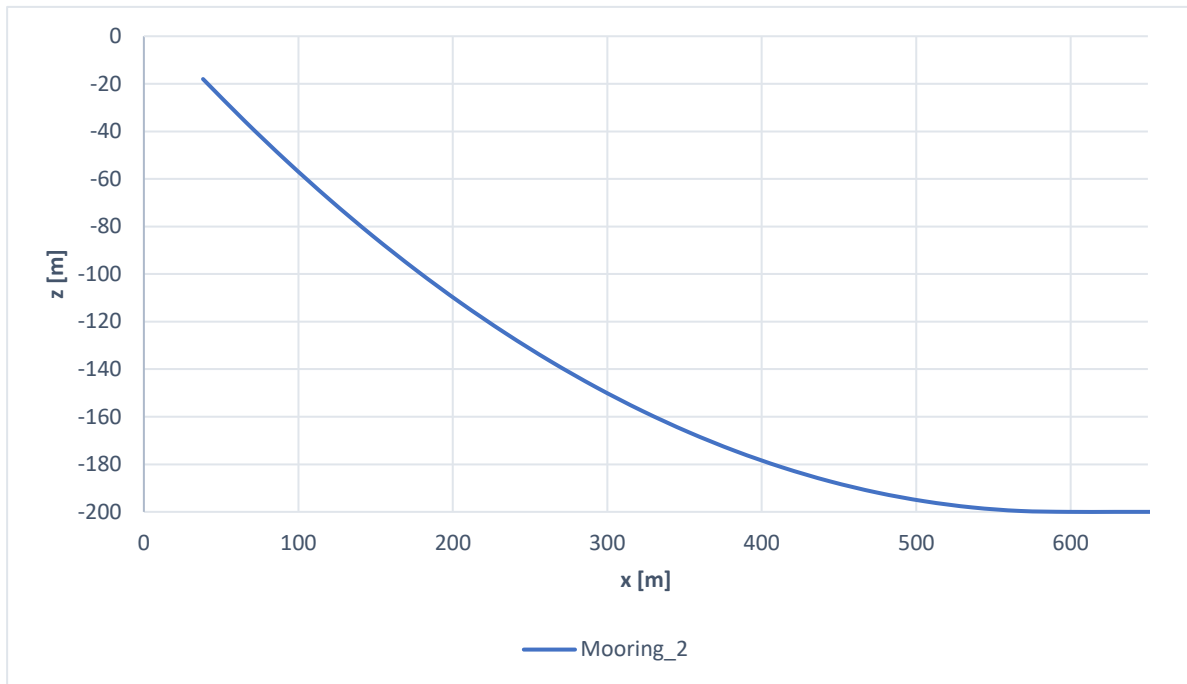
$$\text{Vertical force, } V = \sum W_i \times S_i = 843 \text{ [kN]}$$

$$\text{Total tension of one mooring line} = 1.66 \times 10^6 \text{ [N]}$$

The mooring geometry under static equilibrium can be found from the following formula:

$$y = \frac{H}{W} \left(\cosh \frac{W}{H} x - 1 \right)$$

CSC single mooring layout



Initial stability check:

Freeboard check, $f = 10 \text{ [m]} > 0$ “OK”

Area of inertia in pitch direction, $I = I_{xx} + Ad^2 = 8.4 \times 10^4 \text{ [m}^4\text{]}$

Displacement, $\nabla = 10135.7 \text{ [m}^3\text{]}$

$Z_{csc, bottom} = -30 \text{ [m]}$

$\overline{BM} = \frac{I}{\nabla} = 8.28 \text{ [m]}$

$\overline{KB} = COB - z_{csc, bottom} = 7.7 \text{ [m]}$

$\overline{KG} = COG - z_{csc, bottom} = 11.39 \text{ [m]}$

$\overline{KB} + \overline{BM} - \overline{KG} = 4.6 \text{ [m]} > 0$ “OK”

(Theory part for initial stability can be referred to chapter 2.)

From the calculations, it is clear that the CSC can satisfy the criteria of initial stability.